# DEFORMATION AND BEHAVIOUR OF DISLOCATIONS IN SILICON CRYSTALS

---

YOICHI NISHINO

| 報告番号 | 甲第1566号 |
| --- | --- |

# CONTENTS

# CHAPTER 1

# INTRODUCTION

## 1.1. INTRODUCTORY REMARKS

In semiconductor crystals such as silicon, the Peierls-Nabarro barrier for dislocation motion is extremely large because of the covalent bonding, so that very high stress is required to generate and move dislocations. The dislocation mobility in these crystals is, therefore, much lower than that in metal crystals and also depends sensitively on the deformation temperature. Namely, in the temperature range below Tm/2 (Tm: the melting temperature in Kelvin), the macroscopic plastic deformation of crystals does not take place, that is, dislocations are practically immobile under applied stress and the crystals are extremely brittle like ordinary ceramics. In contrast to this, they become increasingly ductile above Tm/2 and behave like metal crystals [1].

On the other hand, various semiconductor crystals, now utilized widely in device technology, are usually grown in a dislocation-free state or with very low densities of dislocations. However, dislocations are often introduced into such crystals

during subsequent thermal processing, which lead to a deterioration of device properties. In order to consider successful counterplans for controlling the generation of dislocations in device elements, it is first necessary to understand the generation and the multiplication processes of dislocations under the simple stress condition such as tensile deformation.

The technique of in-situ observation using high voltage electron microscope (HVEM) [2,3] is suited to the detailed investigation of dislocation process occurring on a microscopic scale. However, observations on a macroscopic scale are also necessary to clarify from where and how dislocations are generated and move in dislocation-free bulk crystals. By using a recently developed 90 kW-class ultra high intensity X-ray generator and a TV imaging system, it is now possible to carry out real-time observations of dynamic phenomena occurring in bulk crystals by means of X-ray topography [4,5].

Silicon crystals are expected to have the following advantages for the study on the deformation and the behaviour of dislocations.

(i) Highly perfect crystals of high purity can be easily obtained. Generally in metal crystals, the density of grown-in dislocations is fairly high and also the purity obtainable is not so high as compared with that of silicon crystals, so that it is hard to know how crystal perfection and purity affect the deformation characteristics of crystals from the study on metals. Such difficulties may not exist in the study on silicon crystals.

(ii) In covalent crystals such as silicon, it is believed that

Peierls-Nabarro barrier plays a predominant role in the resistance to the motion of dislocations [6]. Therefore, experimental studies of the dislocation motion can be made under relatively ideal conditions and a clear-cut analysis of the results obtained may be possible.

(iii) The dislocation velocity depends sensitively on the temperature and rather insensitively on the stress. Such dynamical characteristics of dislocations are reflected in the mechanical behaviour of crystals. Thus, the level of the flow stress in semiconductor crystals depends sensitively on the strain rate and the deformation temperature throughout all deformation stages [7-9].

(iv) The dislocations are practically immobile at room temperature, so that the dislocation configuration developed during high-temperature deformation is easily frozen in when the crystals are rapidly cooled under the applied load. Consequently, the arrangements of dislocations which have contributed to deformation can be revealed by transmission electron microscopy [10].

## 1.2. GENERAL SURVEY OF PREVIOUS WORKS

### 1.2.1. Dislocations in Silicon Crystals

The diamond cubic lattice, shown in Fig. 1-1, corresponds to two interpenetrating f.c.c. lattices, one of which is dis-

placed by a/4[111] (a: lattice constant of unit cell) with respect to the other. Atoms in the two lattices do not have identical surroundings, so that the structure can be described as an f.c.c. structure with a basis of two atoms per lattice point. The primitive-unit-cell vectors remain those associated with a single f.c.c. lattice. Thus, the slip plane in the diamond cubic lattice is {111} and the perfect dislocations have Burgers vectors a/2<110> [11]. Presumably because of a large Peierls-Nabarro barrier with deep troughs along <110> directions, glide dislocations lie primarily along <110> directions when the dislocation density is low [12]. Gride dislocations lying along <110> directions are either pure screw or 60° dislocation, so called because the Burgers vector is inclined at an angle of 60° to the direction of dislocation line.

The layer structure of diamond lattice contains (111) planes in the sequence AaBbCc, as shown in Fig. 1-2. Because of the double-layer atomic arrangement, there are two inherently different sets of dislocations, one member of each set having a Burgers vector identical to one dislocation in the other set. Dislocations in the broad layers such as Aa are termed the shuffle set and those in the narrow layers such as aB termed the gride set [13]. Various characteristics of dislocations in semiconductor crystals have been so far discussed on an assumption that they are of the perfect type in shuffle set [1]. Recent transmission electron microscopy using a weak-beam technique [14-19] and high-resolution electron microscopy [20-22], however, show that dislocations at rest in silicon crystals are extended, i.e., the

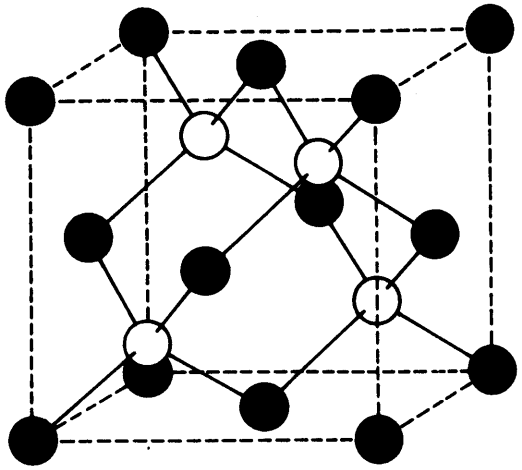

Fig. 1-1. Diamond cubic unit cell. The diamond cubic lattice corresponds to two interpenetrating f.c.c. lattices.

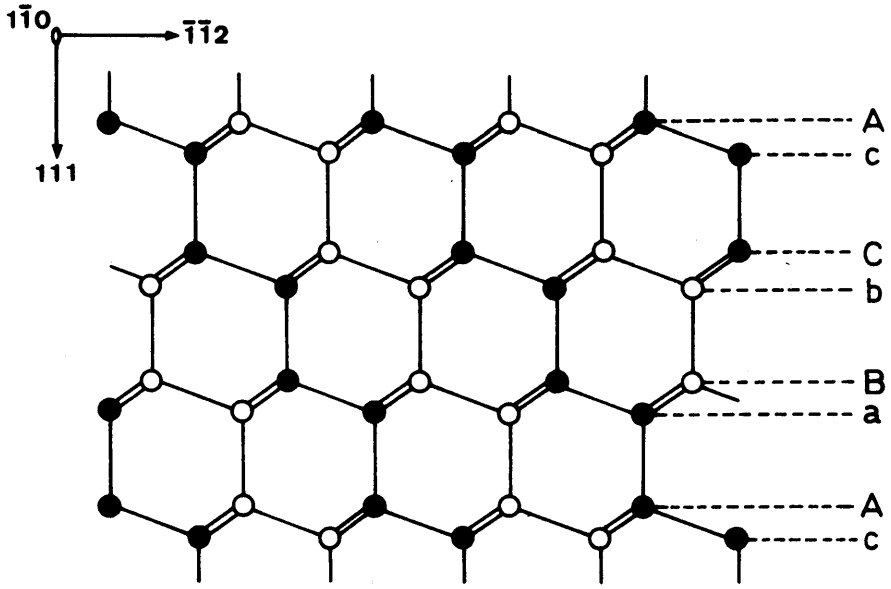


Fig. 1-2. A diamond cubic lattice projected normal to (1$\bar{1}$0). Full circles represent atoms in the plane of the paper and open circles represent atoms in the plane below. (111) is perpendicular to the plane of the paper and appears as a horizontal trace.

dislocations are of the gride set. According to these observations, the stacking fault energy of silicon crystals is estimated to be 50 - 60 $mJm^{-2}$, from the widths of images of extended dislocations. It has been confirmed by means of in-situ HVEM observation [23] that moving dislocations in silicon crystals are also extended.

### 1.2.2. Dislocation Mobility

The dislocation velocities in silicon crystals have been extensively investigated as a function of stress and temperature by means of etch pitting [24-27], conventional X-ray topography [28-35], real-time X-ray topography [36,37] and in-situ electron microscopy [38]. These results seem to be consistent with the thermally activated motion of dislocations, which proceeds through a double-kink mechanism [6]. It has been found that the dislocation velocity v is expressed approximately with the equation:

$$v = v_o \, (\tau / \tau_o)^m \exp (-E / kT) \qquad (1.1)$$

where $\tau$ is the applied shear stress, $\tau_o$ a constant, T the deformation temperature and k the Boltzmann constant. The magnitudes of exponent m and activation energy E for 60° dislocation are, for example, 1.1 and 2.2 (eV), respectively [39]. However, there is a little difference especially in the absolute values of dislocation velocity among the results obtained so far. This difference in dislocation velocity seems to be caused by the

experimental conditions. Namely, most of the investigations [24-34] adopted an intermittent observation in which a specimen is cooled to room temperature for observation after applying stresses at elevated temperatures and then the distance moved by dislocations are measured.

On the other hand, Chikawa et al. [36] observed X-ray topographs of moving dislocations continuously through a vidicon camera and measured directly the dislocation velocity by using a video tape recorder (VTR). By means of this real-time X-ray topographic observation, Sumino et al. [37] measured the dislocation velocities at various temperatures as a function of the resolved shear stress in float-zone crystals and Czochralski crystals both of intrinsic type. As a result, no appreciable difference is observed in the velocities of both types of crystal except for the fact that no motion of dislocations are realized in Czochralski crystals when they are under stress lower than about 3 $MN/m^2$ [37].

Here, real-time X-ray topography is expected to have the following advantages; (i) the dynamic behaviour of dislocations in a thick specimen can be observed for crystals with low dislocation densities, (ii) fast motion of dislocations can be observed because of low-magnification observation, (iii) macroscopic properties such as stress-strain curves can be investigated easily in parallel with the observation of dislocations, (iv) dislocation motion free from radiation damage can be observed*.

* In MgO crystals, however, it has been demonstrated that the yield stress is increased by 10 to 50 % due to the intensive X-ray irradiation [40].

The dislocation velocity in silicon crystals is known to be markedly influenced by doping with electrically active impurities. It is generally accepted that n-doping results in an increase of the velocities of screw and 60° dislocation [24,25,32-34]. However, the effect of p-doping is not well understood. It seems that for rather high concentrations of accepters, the velocity also increases when compared with intrinsic crystal [24,25,32,33]. However, it seems that in moderately p-doped crystal, no clear effect is observed for screw dislocation while the velocities of 60° dislocations are slightly lower than in intrinsic crystal [34].

### 1.2.3. Deformation Characteristics

It has now been 30 years since the elemental semiconductor crystals, silicon and germanium, were first plastically deformed [41]. Many investigations, thereafter, have been performed to get the knowledge of their high-temperature plastic properties and the behaviour of dislocations in these crystals. The progress in the research field of plasticity of semiconductor crystals, especially of germanium, were summarized by Alexander and Haasen [1] from the view point of a micromechanical (dislocation dynamical) theory of macroscopic plastic properties.

The mechanical properties of bulk crystals of silicon have been investigated mainly by the two modes of deformation, that is, tension [37,42-49] and compression [50-59]. It is well known that the crystals having a very low density of dislocations show

a marked yield drop phenomena and that the macroscopic deformation proceeds by means of the propagation of Lüders bands in the deformation stage from the upper yield point to the lower yield point [37,43,53,56]. Lüders bands usually originate from the specimen-holding positions and propagate inwards. It is also indicated that even when the resolved shear stress reaches the lower yield point, the dislocation distribution as well as the local strain is very inhomogeneous over the specimen length [60]. The values of the upper and the lower yield stresses are strongly dependent on the strain rate $\dot{\varepsilon}$ and the temperature T, and both stresses are well-described by the following relation [8, 43,46,51,60,61]:

$$\tau = A \, (\dot{\varepsilon} \, / \, \dot{\varepsilon}_o)^{1/n} \exp \, (U \, / \, kT) \qquad (1.2)$$

As for silicon crystals, the magnitudes of n and U are, for example, 2.4 and 1.25 (eV) for upper yield stress, and 3.3 and 0.8 (eV) for lower yield stress, respectively [46]. Namely, they become higher for higher strain rate and also for lower temperature.

Semiconductor crystals can be deformed to higher strains if the applied stresses and the temperatures are high enough*.

---

* Observations have been so far restricted to temperatures above 900 - 1000 K since below these temperatures crystals under stress fail by fracture without plastic deformation. Recently, suppression of brittle behaviour has been achieved by superimposing a confining pressure in compression tests. Silicon crystals were deformed at temperatures as low as 573 K and had the resolved flow stress values of up to 1000 $MN/m^2$ [58].

Figure 1-3 shows a typical stress-strain curve of specimen deformed at elevated temperature [1]. These specimens show a three-stage hardening curve (beyond stage 0) over the whole temperature range, which guarantees sufficient ductility. In detail, stage I (easy glide) is characterized by a small constant hardening rate $(d\tau/d\varepsilon)_I = \theta_I$, the sebsequent stage II by a much larger and still constant $(d\tau/d\varepsilon)_{II} = \theta_{II}$, whereas in stage III the hardening curve has concave shape. The stresses at the beginning of stage I, II and III are denoted here by $\tau_I$, $\tau_{II}$ and

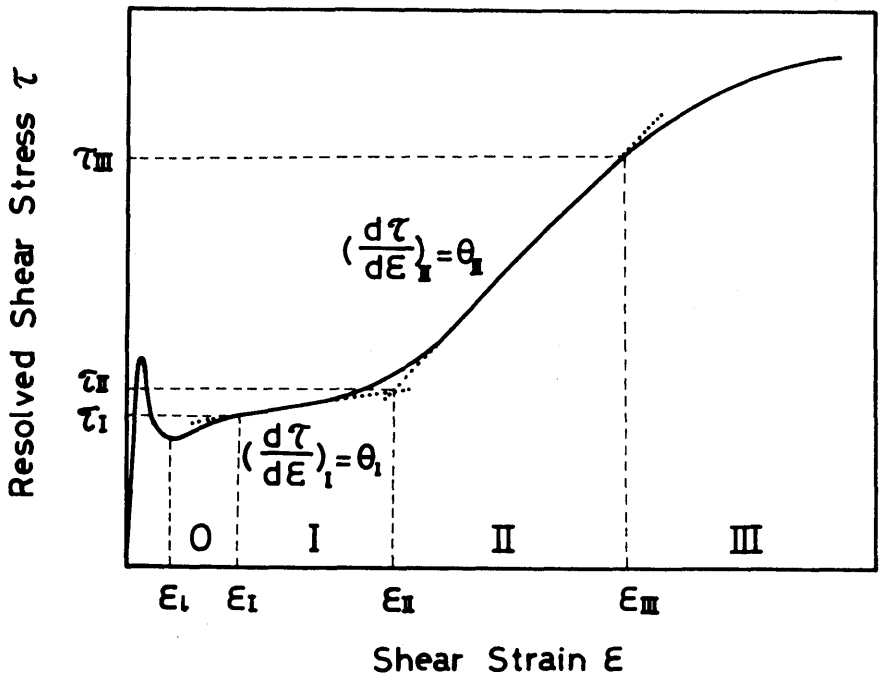


Fig. 1-3. Typical stress-strain curve of semiconductor crystals. These crystals show a three-stage hardening curve (beyond stage 0): stage I, II, III. The definition of various parameters is also given in the figure.

$\tau_{III}$, respectively, and these show the strain rate and temperature dependence given by Eq. (1.2). With increase in the temperature, the stress-strain curve shrinks in size maintaining a similar shape, and the increase in the strain rate results in a similar effect as that brought by the increase of the temperature [8,46].

For understanding of the mechanical behaviour of crystals, it is essential to know the dislocation processes occurring during deformation. In this case, electron microscopy is suited to the investigation of dislocation configuration on a microscopic scale since the dislocation density is extremely high after plastic deformation. It has been revealed in germanium crystals [10, 62] that the dislocation configurations in various deformation stages and the work-hardening processes are very similar to those of f.c.c. metals. There are also some investigations of dislocation configuraitons in deformed silicon crystals [50,55,63] although these observations are restricted to small strain regions. On the other hand, X-ray topography is a unique and powerful technique for the observations of dislocation processes in bulk crystals with low densities of dislocations. The generation and the multiplication processes of dislocations in silicon crystals have been investigated by using this technique [29,35, 45,64-68]. It is generally accepted that dislocations are often generated preferentially in the surface region in a highly perfect crystal. Such generation of dislocations usually takes place heterogeneously, and this fact leads to an idea that some irregularities on the surface play important roles in the gener-

ation process of dislocations [45,66].

Hereupon, dynamic deformation such as fatigue cycling has not yet been applied to semiconductor crystals, except for the fatigue deformation by using reversed cantilever bending [69]. This is probably due to the difficulties in experimental technique. Nevertheless, the investigation of cyclic deformation behaviour is important not only to controll the dislocation generation in device elements but also to provide some significant information on the fatigue-induced microstructure of metals and ceramics.

### 1.2.4. Effects of Oxygen on Dislocation Motion

Czochralski-grown silicon crystals are now used widely in device manufacture because of their smaller susceptibility to the thermal slip in wafers occurring during processing. These crystals, which are commonly grown from the melt in fused quartz crucibles, originally contain oxygen atoms at a concentration of about $10^{18}$ $cm^{-3}$. The precipitation of supersaturated oxygen atoms, therefore, takes place in Czochralski crystals in the course of heat treatment at elevated temperatures below 1500 K, and various types of lattice defects are known to be introduced in cennection with this precipitation [70-74]. Although the state and the shape of oxide precipitates change in company with the change of annealing temperature, as summarized in Table 1-1, these precipitates are identified as silicon oxide [70,75].

The effects of oxygen on the dislocation motion are tenta-

Table 1-1. State of oxide precipitate in silicon crystal

| Annealing Temperature (K) | 720—1050 | 1140—1200 | 1260—1340 |
|---|---|---|---|
| State | $SiO \rightarrow SiO_2$ Amorphous | $SiO_2$ Cristobalite | $SiO_2$ Amorphous |
| Shape | * | Square-shaped platelet | Octahedron |

tively considered as follows; (i) dislocation pinning effect by isolated oxygen atoms and/or their clusters [76,77], (ii) dislocation locking effect by oxygen atoms [37], (iii) precipitation hardening by oxide precipitates[78], (iv) precipitation softening by oxide precipitates [44,49,55,56,58]. Hu [76,77] reported that dislocations were generated more easily in float-zone crystals during the thermal processing of wafers than in Czochralski crystals and that isolated oxygen atoms and/or their clusters impeded the motion of individual dislocations (i). Recently, Sumino et al. [49] have shown that the difference in mechanical strength of both crystals originates in the locking effect of dislocations by oxygen atoms (ii), which takes place only in Czochralski crystals, and not in the difference in the dislocation mobility between the two types of crystals. On the other hand, oxide precipitates are introduced in Czochralski crystals after annealing at high temperatures. It may be considered that

they become obstacles to the motion of dislocations [78], so that the precipitation hardening is caused (iii). As a matter of fact, nevertheless, the magnitudes of the upper yield stress and of the yield drop always decrease upon precipitaion of oxygen atoms [44,49,55,58], in other words, the crystals soften drastically on heat treatment at temperatures around 1273 K (iv). In this case, dislocations punched out from precipitates play the most important role in the softening due to precipitation [49].

The above effects of dissolved and precipitated oxygen atoms on the motion of dislocations can be applied directly to device technology as the roles of oxygen during thermal processing, as shown in Table 1-2. Even if dislocations are nucleated by thermal stress in originally dislocation-free crystals during processing, they are thought to be locked rapidly by dissolved oxygen atoms [37], not being able to act as dislocation multiplication centers. Dissolved oxygen atoms, therefore, have the advantage of the reduction of thermal slip. Once the precipitation of oxygen atoms takes place, however, thermally induced microdefects, including oxide precipitates, dislocation loops and so on, are introduced in crystals. They are detrimental to device properties when they are formed in a region near the crystal surface and also lead to the thermal slip, acting as sources of mobile dislocations. On the other hand, they also act as gettering sites for undesirable impurities when they are formed in bulk region far from the surface [79]. Precipitated oxygen atoms, in this case, turn to advantage.

Table 1-2. Roles of dissolved and precipitated oxygen atoms in Czochralski crystal during thermal processing.

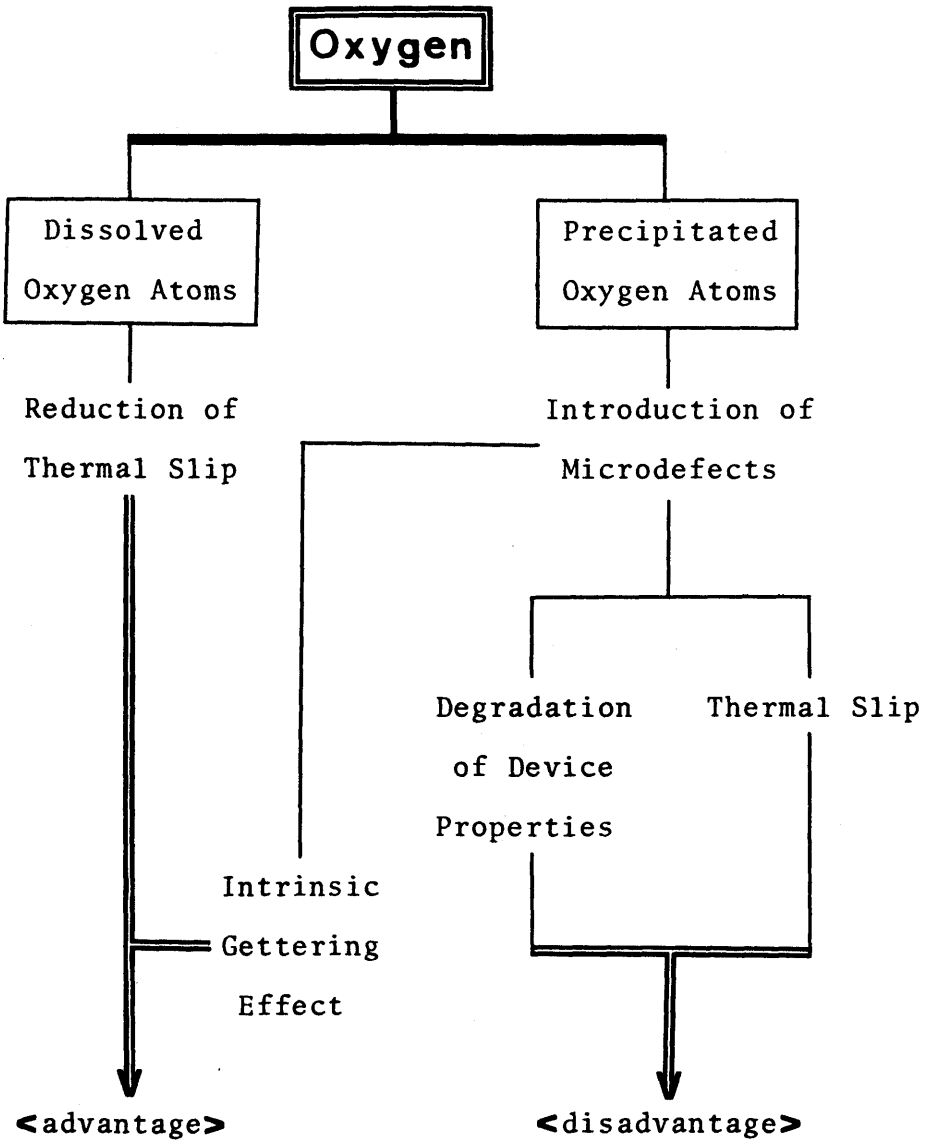

Oxide films thermally grown on silicon crystals are also employed in device technology. It is recognized that they involve internal stress after cooling because of the difference in thermal expansion between oxide film and silicon crystal. This stress brings lattice strain in crystal, which gives rise to the enhanced X-ray diffraction at the boundary between the oxidized region and the oxide-removed region [80,81]. Mechanical stress at the edges of oxide windows is known to be able to cause the generation of dislocations which reduces the yield of semiconductor devices [82].

## 1.3. THE AIMS OF THE PRESENT STUDIES

With the recent progress of silicon semiconductor device, it has become the object of attention how dislocations are nucleated, move and multiply during the growth processes of crystals and during the subsequent thermal processes of wafers since they bring about harmful effects on the performance of devices. For the purpose of controlling of the generation and multiplication of dislocations, it is necessary to get the knowledges of the mechanical properties and also the dynamical behaviour of dislocations in silicon crystals under simple deformation conditions. Silicon crystals are a typical material in which the Peierls-Nabarro barrier for dislocation motion is extremely large. The investigations of deformation behaviour of such a crystal at elevated temperatures, hence, can provide some useful information

on the dislocation processes of metals and ceramics.

By the way, Czochralski-grown silicon crystals are commonly utilized in the fabrication of semiconductor device. Meanwhile, it has been recognized that there is a big difference in the mechanical response to the thermal stress between float-zone crystals and Czochralski crystals (see Section 1.2.4.). It may be reasonable to think that such a difference in the mechanical strength is related to the difference in the cencentration of impurities, e.g., oxygen atoms included in these crystals. Also from the view point of practical uses, it is interesting to investigate how such impurities or defects affect various dislocation processes which control the mechanical behaviour of Czochralski crystals.

In the present studies, Czochralski crystals were at first deformed in tension at elevated temperatures by using an Instron-type testing machine. The crystals deformed to higher strains were examined by means of high voltage electron microscopy to reveal in detail the dislocation configurations (Chapter 2). In order to observe dynamically the dislocation processes during tensile deformation, a high-temperature deformation apparatus was newly constructed for real-time X-ray topography (Chapter 3). With the aid of this apparatus which was combined with an ultra high intensity X-ray generator and a TV imaging system, the generation process and the movement of dislocations in originally dislocation-free crystals were investigated at elevated temperatures under various deformation conditions; (i) motion of single dislocations during annealing (Chapter 4), (ii) dislocation gen-

eration at oxide precipitates (Chapter 5), (iii) notch effect during deformation (Chapter 6). Cyclic deformation in push-pull was, for the first time, applied to silicon crystals by using a newly developed high-temperature fatigue apparatus which was attached to an Instron-type testing machine (Chapter 7). Furthermore, in connection with the dislocation generation induced in wafers during thermal processing, thermal stress and the viscoelastic behaviour of oxide films on silicon crystals were revealed directly by in-situ thermal cyclic experiments (Chapter 8).

## REFERENCES


[1] H. Alexander and P. Haasen: Solid State Phys. 22 (1968) 27.

[2] H. Saka and T. Imura: J. Phys. Soc. Jpn. 32 (1972) 702.

[3] H. Saka, K. Noda and T. Imura: Cryst. Lattice Defects 4 (1973) 45.

[4] A.R. Lang: Modern Diffraction and Imaging Techniques in Materials Science, eds. S. Amelinckx, R. Gevers, G. Remaut, and J. Van Landuyt (North-Holland, Amsterdom, 1970) p. 407.

[5] B.K. Tanner: X-Ray Diffraction Topography (Pergamon, Oxford, 1976)

[6] V. Celli, M.N. Kabler, T. Ninomiya and R. Thompson: Phys. Rev. 131 (1963) 58.

[7] S. Schäfer, H. Alexander and P. Haasen: Phys. Status Solidi 5 (1964) 247.

[8] K. Kojima and K. Sumino: Cryst. Lattice Defects 2 (1971) 147.

[9] I. Yonenaga and K. Sumino: Phys. Status Solidi (a) 50 (1978) 685.

[10] H. Alexander: Phys. Status Solidi 26 (1968) 725; 27 (1968) 391.

[11] J.P. Hirth and J. Lothe: Theory of Dislocations (MacGrow-Hill, New York, 1968) p. 353.

[12] W.C. Dash: J. Appl. Phys. 27 (1956) 1193.

[13] J. Hornstra: J. Phys. Chem. Solids 5 (1959) 129.

[14] I.L.F. Ray and D.J.H. Cockayne: Philos. Mag. 22 (1970) 853.

[15] I.L.F. Ray and D.J.H. Cockayne: Proc. R. Soc. London A 325 (1971) 543.

[16] A.M. Goměz, D.J.H. Cockayne, P.B. Hirsch and V. Vitek: Philos. Mag. 31 (1975) 105.

[17] K. Wessel and H. Alexander: Philos. Mag. 35 (1977) 1523.

[18] A.M. Goměz and P.B. Hirsch: Philos. Mag. 36 (1977) 169.

[19] H. Föll and C.B. Carter: Philos. Mag. A40 (1979) 497.

[20] J.C.H. Spence and H. Kolar: Philos. Mag. A39 (1979) 59.

[21] M. Sato, K. Hiraga and K. Sumino: Jpn. J. Appl. Phys. 19 (1980) L155.

[22] M. Sato, K. Sumino and K. Hiraga: Phys. Status Solidi (a) 68 (1981) 567.

[23] M. Sato and K. Sumino: Phys. Status Solidi (a) 55 (1979) 297.

[24] V.N. Erofeev, V.I. Nikitenko and V.B. Osuenskii: Phys. Status Solidi 35 (1969) 79.

[25] V.N. Erofeev and V.I. Nikitenko: Sov. Phys. -Solid State 13 (1971) 116.

[26] V.N. Erofeev and V.I. Nikitenko: Sov. Phys. -JETP 33 (1971) 963.

[27] A. Fischer: Exp. Tech. Phys. 23 (1975) 617.

[28] T. Suzuki and H. Kojima: Acta Metall. 14 (1966) 913.

[29] V.C. Kannan and J. Washburn: J. Appl. Phys. 41 (1970) 3589.

[30] A. George, C. Escaravage, G. Champier and W. Schröter: Phys. Status Solidi (b) 53 (1972) 483.

[31] L.S. Milevskii and I.L. Smol'skii: Sov. Phys. -Solid State 19 (1977) 772.

[32] S.B. Kulkarni and W.S. Williams: J. Appl. Phys. 47 (1976) 4318.

[33] J.R. Patel, L.R. Testardi and P.E. Freeland: Phys. Rev. B13 (1976) 3548.

[34] A. George and G. Champier: Phys. Status Solidi (a) 53 (1979) 529.

[35] S. Ōki and K. Futagami: Jpn. J. Appl. Phys. 13 (1974) 605.

[36] J. Chikawa, I. Fujimoto and T. Abe: Appl. Phys. Lett. 21 (1972) 295.

[37] K. Sumino, H. Harada and I. Yonenaga: Jpn. J. Appl. Phys. 19 (1980) L49.

[38] F. Lauchet: Philos. Mag. A43 (1981) 1289.

[39] K. Sumino: Semiconductor Silicon 1981 (Electrochem. Soc., Pennington, 1981) p. 208.

[40] Y. Nishino, U. Messerschmidt and T. Imura: to be published in Mater. Sci. Eng.

[41] C.J. Gallagher: Phys. Rev. 88 (1952) 271.

[42] W.D. Sylvestrowicz: Philos. Mag. 7 (1962) 1825.

[43] J.R. Patel and A.R. Chaudhuri: J. Appl. Phys. 34 (1963) 2788.

[44] J.R. Patel: Discuss. Faraday Soc. 38 (1964) 201.

[45] Y. Tsunekawa and S. Weissmann: Metall. Trans. 5 (1974) 1585.

[46] I. Yonenaga and K. Sumino: Phys. Status Solidi (a) 50 (1978) 685.

[47] M. Suezawa, K. Sumino and I. Yonenaga: Phys. Status Solidi (a) 51 (1979) 217.

[48] K. Sumino and I. Yonenaga: Jpn. J. Appl. Phys. 20 (1981) L685.

[49] I. Yonenaga and K. Sumino: Jpn. J. Appl. Phys. 21 (1982)47.

[50] V.G. Govorkov, Yu.V. Malov, V.I. Nikitenko and I.S. Smirnova: Sov. Phys. -Crystallogr. 11 (1966) 235.

[51] H. Siethoff and P. Haasen: Lattice Defects in Semiconductors, ed. R.R. Hashiguti (Univ. Tokyo, Tokyo, 1968) p.491.

[52] H. Siethoff: Phys. Status Solidi 40 (1970) 153.

[53] H. Siethoff: Acta Metall. 21 (1973) 1523.

[54] H. Siethoff: Philos. Mag. A37 (1978) 711.

[55] J. Doerschel, F.-G. Kirscht and R. Baehr: Kristall und Technik 12 (1977) 1191.

[56] S. Mahajan, D. Brasen and P. Haasen: Acta Metall. 27 (1979) 1165.

[57] K. Yasutake, M. Umeno and H. Kawabe: Appl. Phys. Lett. 37 (1980) 789.

[58] J. Castaing, P. Veyssière, L.P. Kubin and J. Rabier: Philos. Mag. A44 (1981) 1407.

[59] K. Yasutake, M. Umeno and H. Kawabe: Phys. Status Solidi (a) 69 (1982) 333.

[60] W. Schröter, H. Alexander and P. Haasen: Phys. Status Solidi 7 (1964) 983.

[61] J.R. Patel and P.E. Freeland: J. Appl. Phys. 38 (1967) 3087.

[62] K. Kojima and K. Sumino: Cryst. Lattice Defects 2 (1971) 159.

[63] A.L. Aseev, Yu.N. Golobokov and S.I. Stenin: Phys. Status Solidi (a) 28 (1975) 355.

[64] A. George, C. Escaravage, W. Schröter and G. Champier: Cryst. Lattice Defects 4 (1973) 29.

[65] A. George and G. Champier: Scripta Metall. 14 (1980) 399.

[66] K. Sumino and H. Harada: Philos. Mag. 44 (1981) 1319.

[67] H.J. Queisser, W. Hartmann and W. Hagen: J. Cryst. Growth 52 (1981) 897.

[68] A. George and G. Michot: J. Appl. Crystallogr. 15 (1982) 412.

[69] W.R. Scoble,Jr. and S. Weissmann: Cryst. Lattice Defects 4 (1973) 123.

[70] D.M. Maher, A. Staudinger and J.R. Patel: J. Appl. Phys. 47 (1976) 3813.

[71] T.Y. Tan and W.K. Tice: Philos. Mag. 34 (1976) 615.

[72] K.H. Yang, H.F. Koppert and G.H. Schwuttke: Phys. Status Solidi (a) 50 (1978) 221.

[73] Y. Matsushita, S. Kishino and M. Kanamori: Jpn. J. Appl. Phys. 19 (1980) L101.

[74] F. Shimura, H. Tsuya and T. Kawamura: J. Appl. Phys. 51 (1980) 269.

[75] W. Kaiser: Phys. Rev. 105 (1957) 1751.

[76] S.M. Hu and W.J. Patrick: J. Appl. Phys. 46 (1975) 1869.

[77] S.M. Hu: Appl. Phys. Lett. 31 (1977) 53.

[78] V.V. Batavin: Sov. Phys. -Solid State 8 (1967) 2478; Sov. Phys. -Crystallogr. 15 (1970) 100.

[79] T.Y. Tan, E.E. Gardner and W.K. Tice: Appl. Phys. Lett. (1977) 175.

[80] I.A. Blech and E.S. Meieran: J. Appl. Phys. 38 (1967) 2913.

[81] J.R. Patel and N. Kato: J. Appl. Phys. 44 (1973) 971.

[82] G. Franz and W. Hartmann: J. Appl. Phys. 23 (1980) 107.

# CHAPTER 2

# TENSILE DEFORMATION AND DISLOCATION CONFIGURATIONS

## 2.1. INTRODUCTION

It is well known that thermal slips are often induced in silicon crystals during wafer processing. This thermal slip, which leads to a deterioration of silicon wafers, is much more profound in float-zone silicon crystals than in Czochralski silicon crystals [1,2]. Since the only difference between Czochralski and float-zone crystals lies in the concentration of oxygen impurity (oxygen level in Czochralski crystals is much higher than that in float-zone crystals), it is believed that oxygen must play an important role in suppressing the thermal slip in Czochralski crystals. Although the probability of dislocation nucleation in initially dislocation-free crystals under thermal stress is considered to be similar in both Czochralski crystals and float-zone crystals, the thermally nucleated dislocations in Czochralski crystals cannot act as dislocation sources, while those in float-zone crystals, which are oxygen free, can act as the sources to develop the thermal slip [3].

However, detailed mechanism by which oxygen suppresses the thermal slip is not understood well. In order to understand the dislocation mechanism of the thermal slip during wafer processing, it is of fundamental importance to have a detailed knowledge on the properties of the thermally-nucleated dislocations. Close observations of dislocation configurations developed during high-temperature deformation are considered to provide a useful knowledge on this respect.

The purpose of the experimental study described in this chapter is to investigate the stress-strain characteristics of Czochralski silicon crystals as well as the features of the dislocation distribution as a function of the temperature and the strain rate and also to observe by means of transmission electron microscopy the dislocation configurations in Czochralski crystals deformed at high temperatures in tension up to various deformation stages.

## 2.2. EXPERIMENTAL PROCEDURES

### 2.2.1. High-Temperature Tensile Tests

Tensile specimens were prepared from silicon single crystals (p-type, 50 ohm·cm) grown by the Czochralski technique. The concentration of dissolved oxygen atoms was estimated to be about $1 \times 10^{18}$ $cm^{-3}$ and the density of grown-in dislocations was determined by etch pits as about $2 \times 10^{4}$ $cm^{-2}$. The geometry of

the specimens is shown in Fig. 2-1; the tensile axis and the side surface were parallel to $[\bar{1}23]$ and $(1\bar{1}1)$, respectively, and they had square cross-section approximately 4 x 4 $mm^2$ and gauge length 30 mm. These specimens were first polished mechanically with emery paper (#1500), followed by chemical polishing with an etchant of 1 part HF and 5 parts $HNO_3$ (by volume) until surface damages were removed.

An apparatus, as shown in Fig. 2-2, which is capable of carrying out tensile tests in gas atmosphere at elevated temperatures, was attached to an Instron-type tensile machine (Shimadzu, DSS-2000 Autograph). Temperature of specimens was measured with Pt-PtRh thermocouples which were located close to the top and the bottom parts of each specimen. The temperature of specimens was kept constant with accuracy of $\pm$ 1 K by a P.I.D. temperature regurator. Tensile tests were conducted in argon atmosphere in the temperature range between 1073 K and 1173 K. For the electron microscope observations of dislocation configurations in deformed crystals, specimens were deformed at 1073 K at the strain rate of $1.4 \times 10^{-5}$ $s^{-1}$ to various deformation stages, namely, lower yield point, stage I, transient stage from stage I to stage II and stage II. In order to freeze in the dislocation configurations, the specimens were cooled under load after the desired strain was reached.

The dislocation distributions in deformed crystals were observed with etch-pit technique. Dislocation etch-pits were revealed by etching the side surface of specimens with the Sirtl's reagent which consisted of HF (100 cc), $CrO_3$ (50 g) and

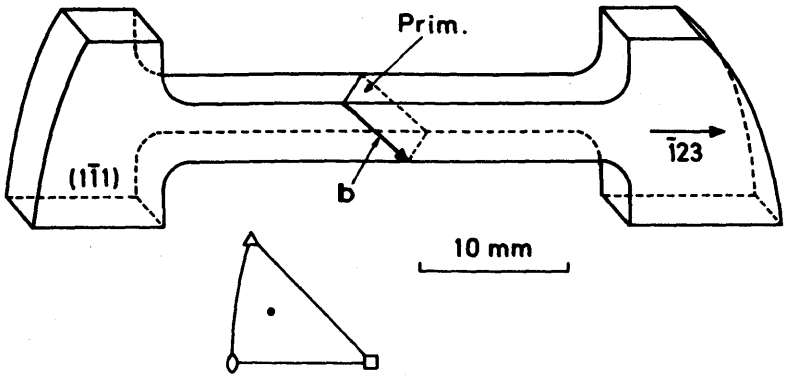


Fig. 2-1. Geometry of shoulder-type tensile specimen; tensile axis parallel to [$\bar{1}$23] and side surface parallel to (1$\bar{1}$1).

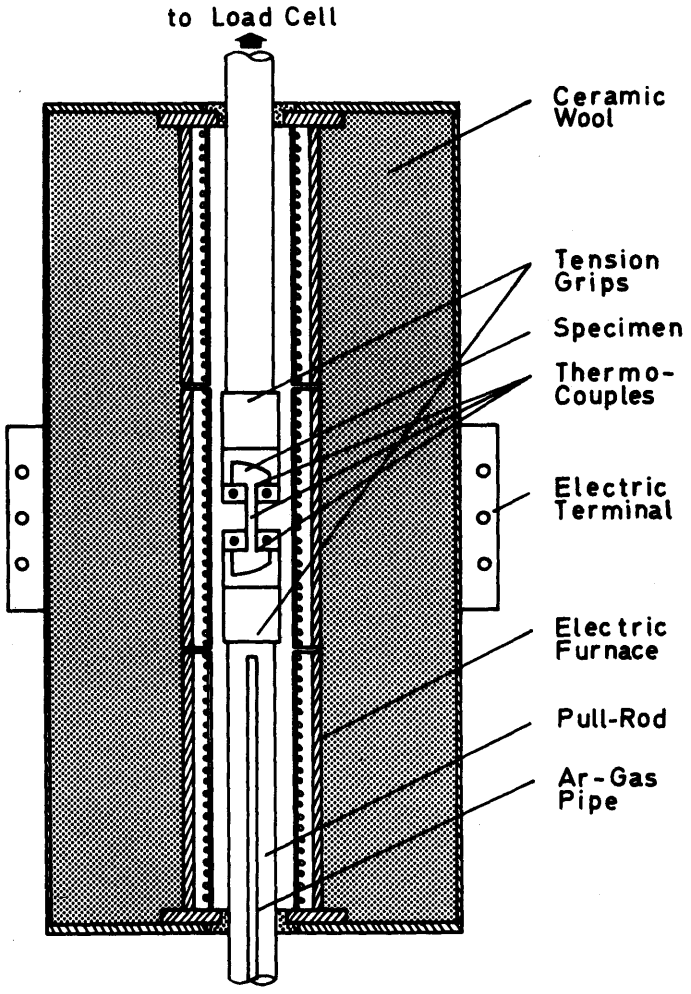


Fig. 2-2. Schematic illustration of high-temperature tensile apparatus for Instron-type testing machine.

$H_2O$ (100 cc).

### 2.2.2. Electron Microscope Observations

Deformed crystals were cut into slices of 0.4 mm thick parallel to the primary slip plane (111), ($\bar{1}$01) and (1$\bar{2}$1) by using a multi-wire saw. Each slice was first thinned mechanically with emery paper (#1000) down to a thickness of about 0.2 mm and then thinned chemically at about 280 K by using an etchant of 1 part HF and 5 parts $HNO_3$ (by volume). These specimens were examined by transmission electron microscopy using a high voltage electron microscope (Hitachi, HU-1000D) operated at 1000 kV. The dislocation densities were measured by counting dislocation intersections with a series of random circles [4].

## 2.3. EXPERIMENTAL RESULTS

### 2.3.1. Tensile Deformation Characteristics

Figure 2-3 shows the stress-strain curves of the specimens deformed in tension at 1073 K, 1123 K and 1173 K at the constant strain rate of $2.1 \times 10^{-5}$ $s^{-1}$. The stress-strain behaviour of Czochralski crystals is qualitatively similar to that of float-zone crystals [5]; with increasing the deformation temperature, the stress-strain curve is reduced in size maintaining approximately the same shape. However, the upper yield stresses of

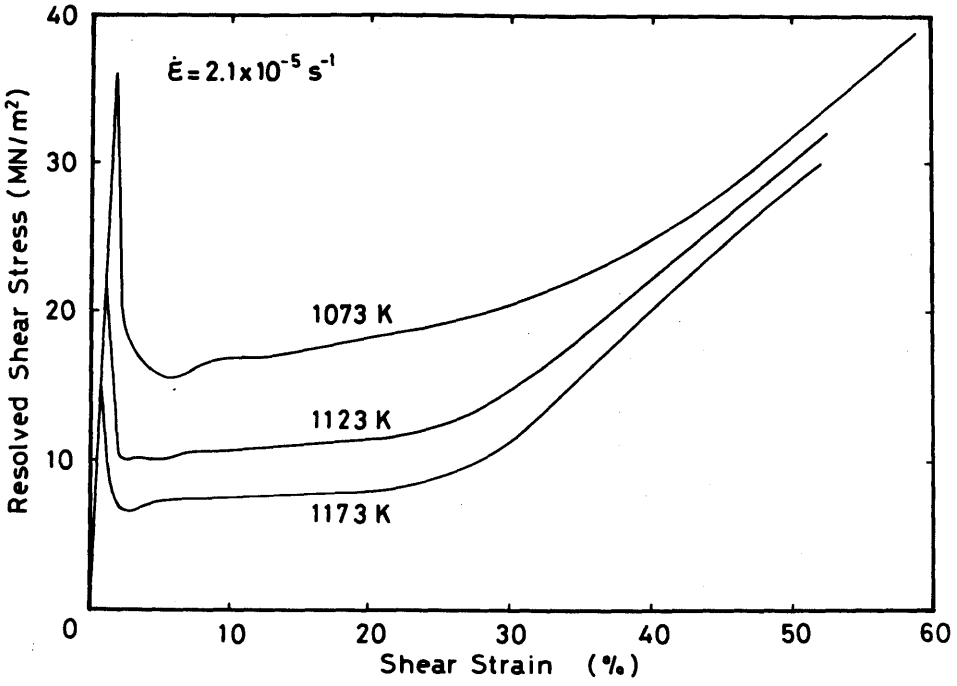


Fig. 2-3. Stress-strain curves of specimens deformed at the strain rate $2.1 \times 10^{-5}\ s^{-1}$ and T = 1073 K, 1123 K and 1173 K, respectively.

Czochralski crystals are much higher than those of float-zone crystals; at any temperature examined, a yield point phenomenon in Czochralski crystals is sharper than float-zone crystals although the initial dislocation density of both crystals is about the same. In addition to this, it was usually observed that the deformation in the yield region proceeds by means of the propagation of Lüders bands at any temperature examined. A quite similar behaviour of the stress-strain curve is also observed by the change in the strain rate, where higher strain rate takes the place of lower temperature in Fig. 2-3.

The dependence of the upper yield stress $\tau_{uy}$ and the lower

yield stress $\tau_{1y}$ on the deformation temperature T is shown in Fig. 2-4. Taking the strain-rate dependence of the upper and the lower yield stresses into consideration, both stresses are well-described by the following relation:

$$\tau = A \, (\dot{\varepsilon} \, / \, \dot{\varepsilon}_o)^{1/n} \exp \, (U \, / \, kT) \qquad (2.1)$$

where $\dot{\varepsilon}_o = 1 \ s^{-1}$ and the values of n and U are 1.7 and 1.01 (eV) for upper yield stress, and 3.3 and 0.92 (eV) for lower yield stress, respectively.

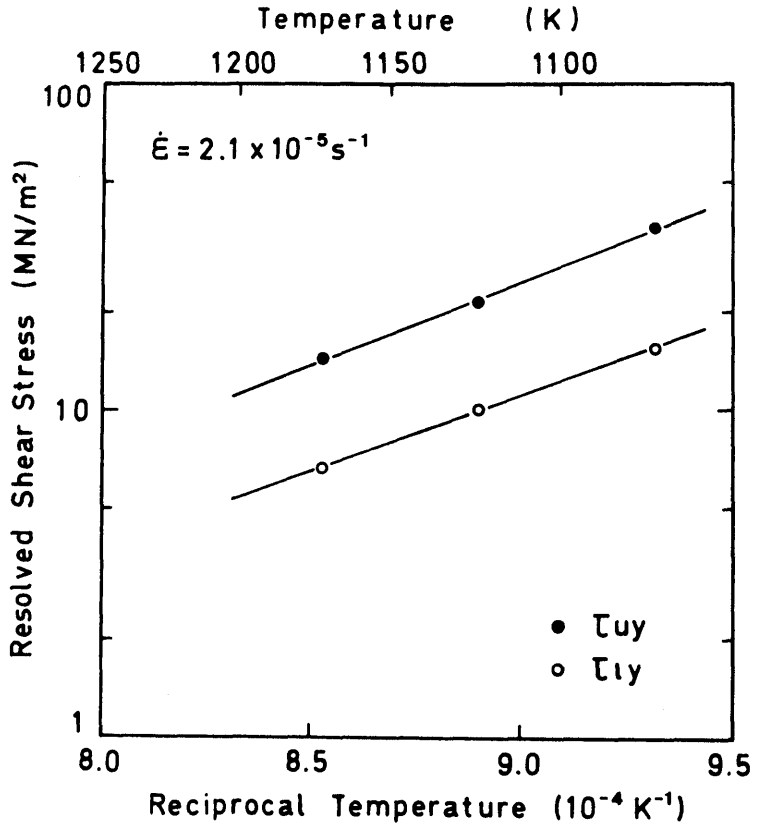


Fig. 2-4. Temperature dependence of the upper yield stress (full circle) and the lower yield stress (open circle) at the strain rate 2.1 x $10^{-5}$ $s^{-1}$.

The development of etch-pit distribution with strain is shown in Fig. 2-5. At the lower yield point (a), the etch-pit distribution is characterized by the etch-pit alignments running parallel to the trace of the primary slip plane. Inhomogenities in the etch-pit density are observed to develop as seen at A and B: the density in the region A is much higher than that in the region B. In stage I (b), etch pits are distributed rather homogeneously over the most area on the surface, while in the region C the density of etch pits is still lower than the other regions. Moreover, alignments of etch pits which belong to the critical slip system are also observed as seen at D. In the transient stage from stage I to stage II (c), one can no longer resolve individual etch pits distinctly since they overlap each other. Narrow regions of the lower etch-pit density are observed to run through the surrounding regions of high etch-pit density, as seen at E. Such regions of low dislocation density are called stripes [6,7]. Although boundaries of stripes are approximately parallel to the trace of the primary slip plane, the etch-pit arrangement inside stripes is dispersed. It is found that stage II begins when the secondary slip system is activated throughout the whole crystal. In stage II (d), the sharp distinction in distribution pattern between regions inside stripes and the surroundings is being lost. A new type of stripes whose boundaries deviate from the direction of the trace of the primary slip plane appears and deformation bands are found. There are two regions in the distribution of etch pits; in the region F, primary dislocations are mainly arranged homogeneously while

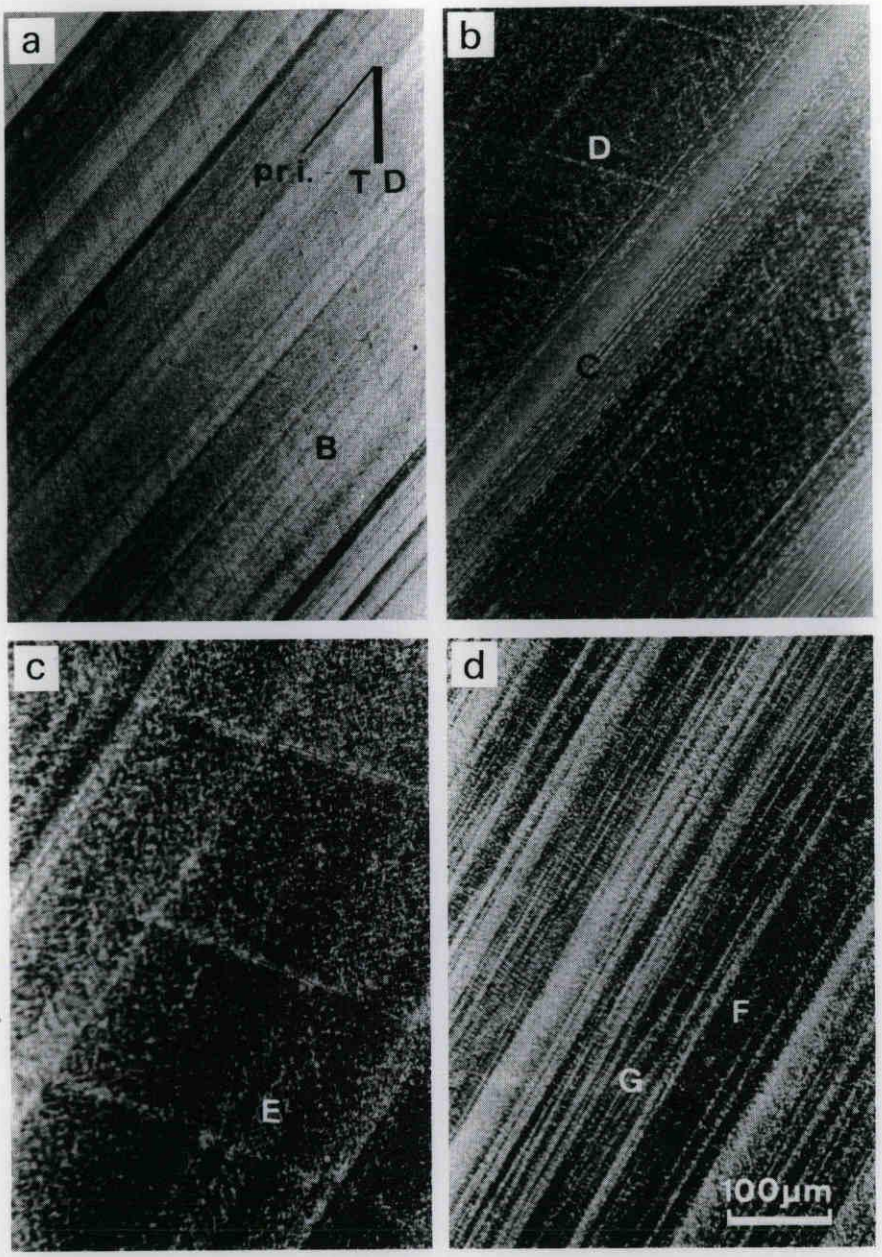


Fig. 2-5. Development of etch-pit distribution with strain on the side surface of the specimens deformed at 1073 K and $\dot{\varepsilon} = 1.4 \times 10^{-5}\ s^{-1}$ : (a) lower yield point ($\varepsilon = 4.5$ %), (b) stage I ($\varepsilon = 24.6$ %), (c) transient stage from stage I to stage II ($\varepsilon = 38.4$ %), (d) stage II ($\varepsilon = 53.7$ %).

in the region G, the density of dislocations of the secondary slip systems is exceedingly high.

### 2.3.2. Dislocation Configurations in Various Deformation Stages

Figure 2-6 shows the dislocation configuration on the primary slip plane at the lower yield point: resolved shear stress 11.5 $MN/m^2$, shear strain 4.5 %. In crystals deformed after the upper yield point, dislocations lying along the close packed direction are scarcely observed. It is found from this figure that long curved primary dislocations (several tens microns in length) are more predominant and the dipole configuration is also revealed. On the other hand, Czochralski crystals showed the heterogeneous deformation accompanied with the propagation of Lüders bands, so that the dislocation distribution was very inhomogeneous over the specimen length. This fact indicates that grown-in dislocations make little contribution to the initial deformation except for the heterogeneous deformation at the specimen ends near the tension grips. At the lower yield point, therefore, the dislocation density may be different in different localities. The total dislocation density is about $9.0 \times 10^7$ $cm^{-2}$, measured in this particular case.

The hardening mechanism of stage I deformation is characterized by the increase of the elastic interaction of primary dislocations which assume often dislocation dipoles [8]. Figure 2-7 shows the dislocation configuration on the primary slip plane in the middle of stage I: resolved shear stress 14.5 $MN/m^2$,

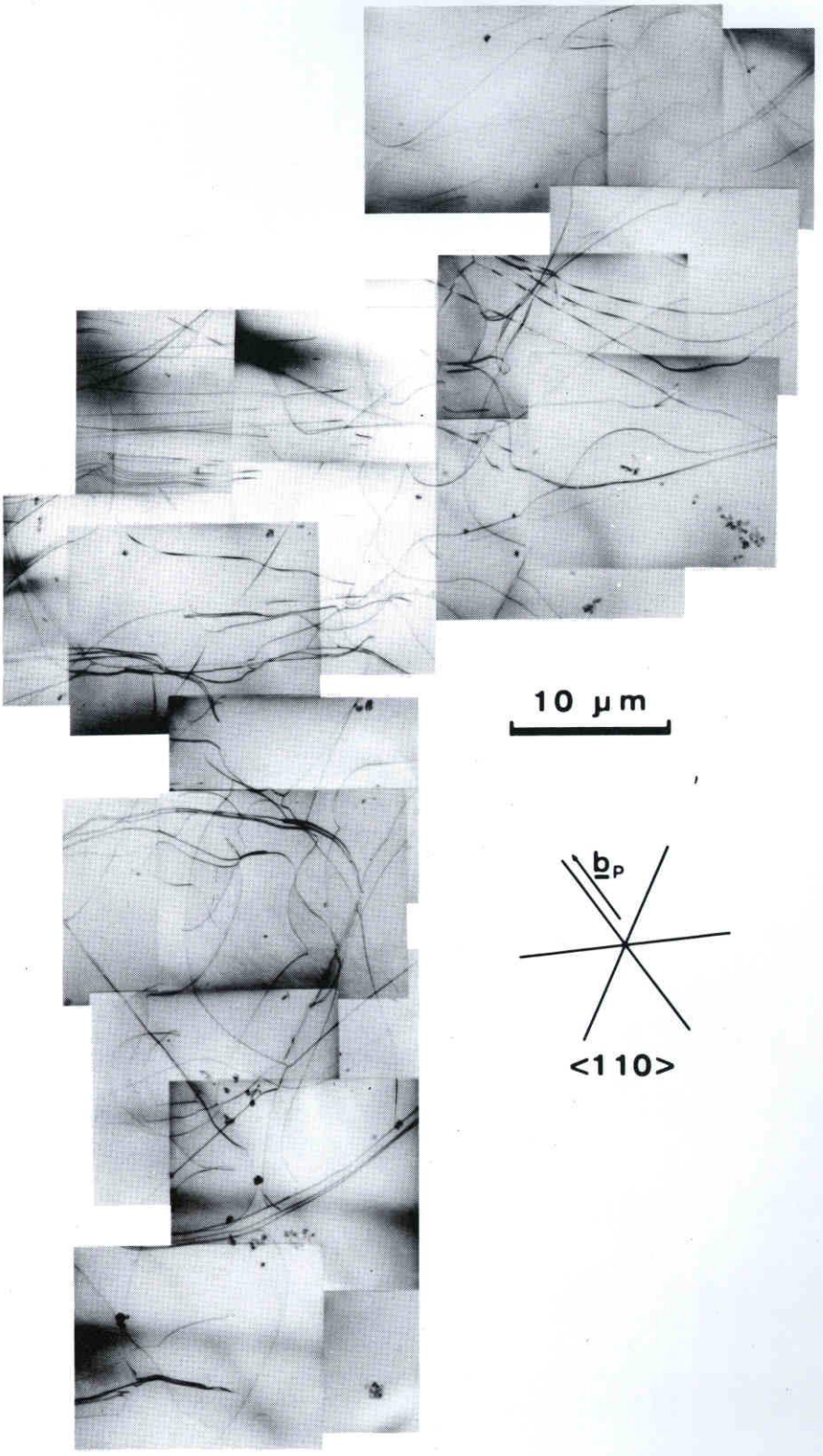


Fig. 2-6. Dislocation configuration on the primary slip plane at the lower yield point: resolved shear stress 11.5 $MN/m^2$, shear strain 4.5 %. The direction of primary Burgers vector is shown in the figure.

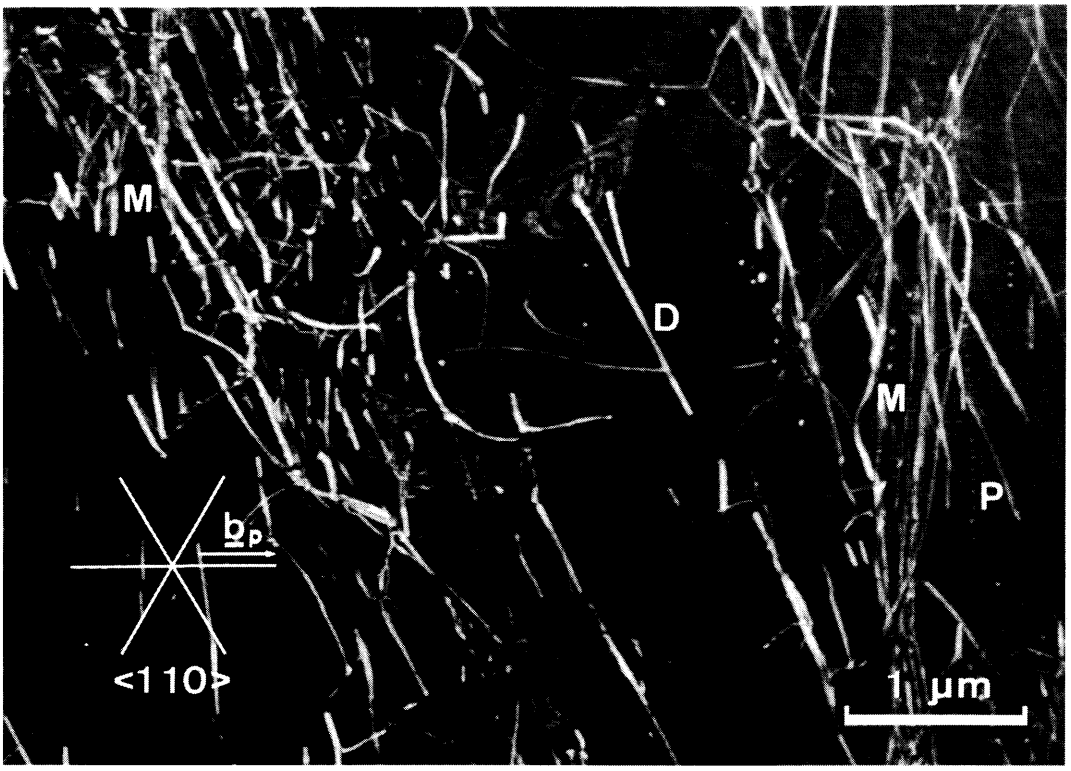


Fig. 2-7. Dislocation configuration on the primary slip plane in the middle of stage I: resolved shear stress 14.5 $MN/m^2$, shear strain 24.6 %. The direction of primary Burgers vector is shown in the figure.

shear strain 24.6 %. The existing dislocations are mainly those of the primary system, and secondary dislocations are hardly observed. The total dislocation density is, in this case, about $8.9 \times 10^8$ $cm^{-2}$. Most of dislocations assume dislocation dipole and/or multipole configuration; each dipole is about 1 - 2 μm in length. Long curved screw dislocations are also found; they are considered moving dislocations. In the region of high dipole density, dipoles are cut into shorter length by the slip of dislocations on other slip planes. In addition to this, rows of prismatic loops (for example, labelled P) are often seen along the direction of the primary edge dislocation. They are most likely to be introduced by break up of a dipole [9]. On the other hand, even by using the weak-beam technique, no detectable obstacles for the motion of dislocations could be observed except for the deformation products such as dislocation dipoles.

Figure 2-8 shows the three-dimensional dislocation configuration in the middle of stage I: resolved shear stress and shear strain are the same as those of Fig. 2-7. The section whose normal is parallel to $[\bar{1}01]$ reveals that dislocation tangles are scarcely present in this stage. Moreover, no lattice misorientation was observed, and the dislocation configuration is fairly uniform on the section though dislocations tend to be extended parallel to $[1\bar{2}1]$ direction. On $[1\bar{2}1]$ section, dislocations are observed to lie strictly parallel to $[\bar{1}01]$ direction which is the intersection direction of the primary slip plane and the foil plane. From this observation, it can be seen that the density of secondary dislocations is much lower than that of primary

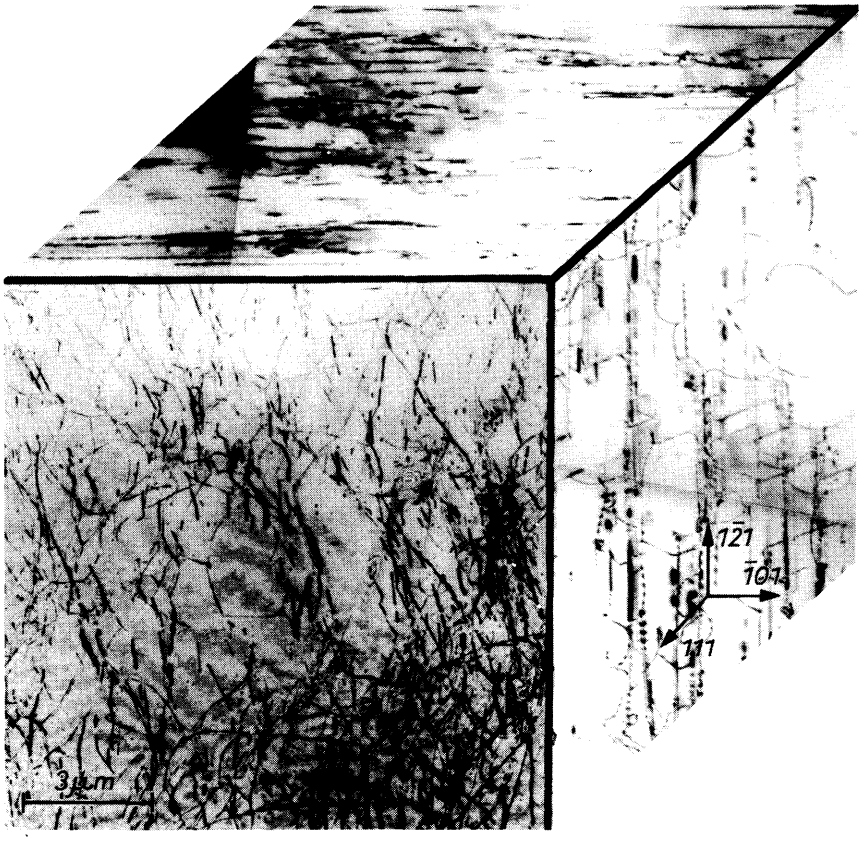


Fig. 2-8. Three-dimensional dislocation configuration in the middle of stage I: resolved shear stress 14.5 $MN/m^2$, shear strain 24.6 %. Crystal faces: (111), ($\bar{1}$01) and (1$\bar{2}$1).

dislocations in stage I.

In stage II, more complicated configurations are observed since dislocations on the secondary slip systems are activated and they interact with the dislocations of the primary system [8]. In the beginning of stage II ( resolved shear stress 18.2 $MN/m^2$, shear strain 38.4 %), the foil consisted of two types of area on the primary slip plane; one was the area of high dislocation density and the other of low dislocation density. The average density of total dislocations is about $1.2 \times 10^9$ $cm^{-2}$. In the former area, secondary dislocations were contained which had about the same density as that of the primary dislocations. The configuration of dislocations in this area was characterized by the bundle of the primary edge dislocation multipoles which were shorter, denser and less regular than those in stage I. These bundles were linked together by secondary dislocations and they served as barriers to dislocation motion. Between the bundles of the primary dislocation multipoles, primary dislocations of the same sign bowed out and arranged in groups, each of which consists of about ten dislocations. In the middle of stage II (resolved shear stress 28.2 $MN/m^2$, shear strain 53.7 %), complicated networks are formed nearly parallel to the primary slip plane as shown in Fig. 2-9. These networks consist of the primary dislocations, the secondary dislocations and their reaction products. The total dislocation density is about $1.9 \times 10^9$ $cm^{-2}$. Configurations which may be associated with short sessile Lomer-Cottrell segments were often observed locally as the consequences of incomplete intersections of the primary and the secondary dis-

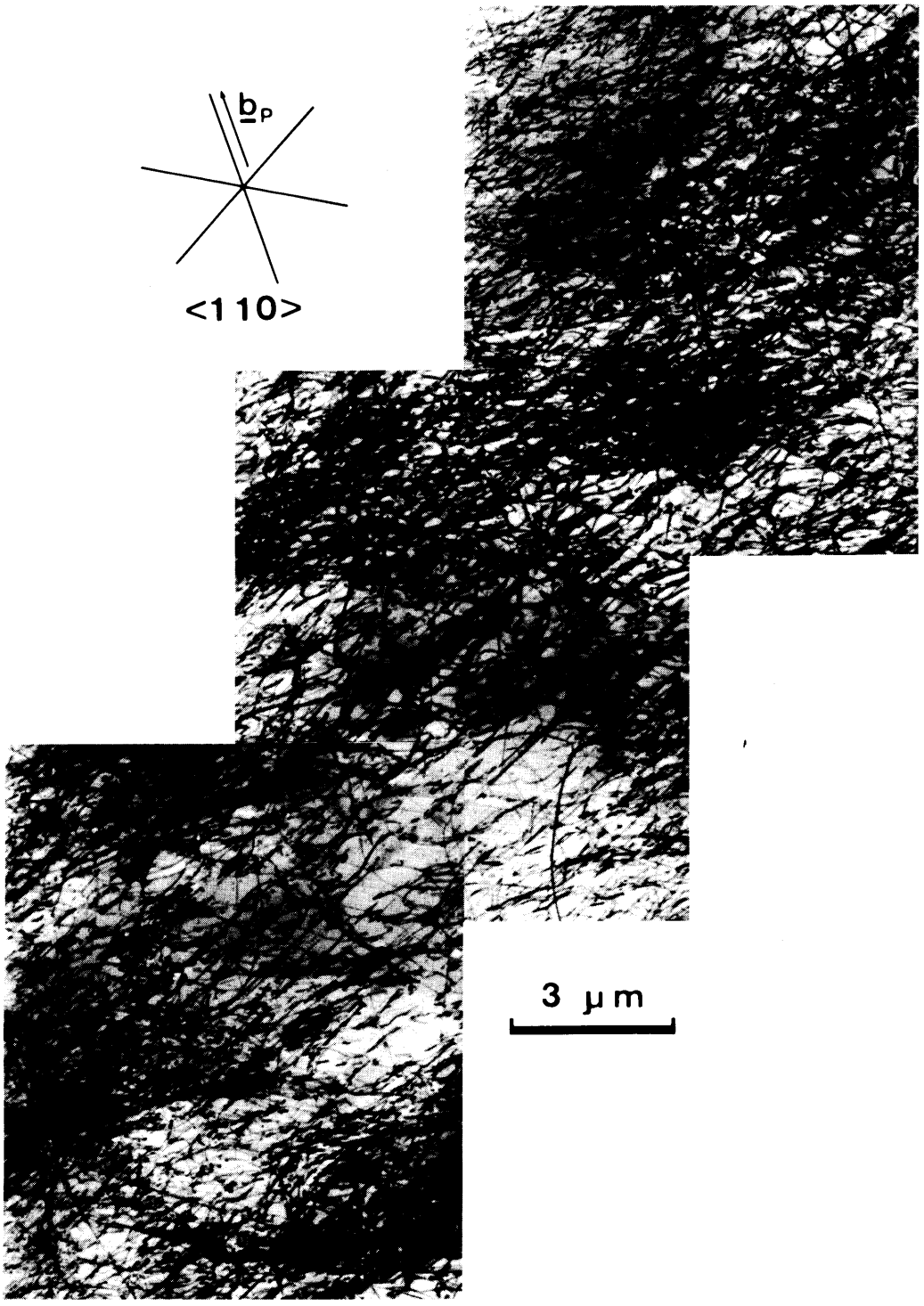


Fig. 2-9. Dislocation configuration on the primary slip plane in the middle of stage II: resolved shear stress 28.2 $MN/m^2$, shear strain 53.7 %. The direction of primary Burgers vector is shown in the figure.

locations. They are not necessarily very prominant features of the dislocation configuration in this stage but may contribute to work hardening by forming grids of dislocations.

Figure 2-10 shows the three-dimensional dislocation configuration in the middle of stage II: resolved shear stress and shear strain are the same as those of Fig. 2-9. The sections perpendicular to the primary slip plane (111) reveal that the dislocation density is high in sets of closely neighbouring planes, each set of which is isolated from the next by an almost dislocation-free zone. The crystal is thus divided into coarse layers approximately parallel to the primary slip plane. The sections, in which the primary slip plane is viewed edge on, assume bands of black-white contrast which are associated with lattice misorientations induced by Lomer-Cottrell network region [10]. However, because black-white contrast is not so distinct, the misorientations are not so strong as f.c.c. metals. Many areas on $[\bar{1}01]$ section contain regions of heavily tangled dislocations and these are also distributed in layers approximately parallel to $[1\bar{2}1]$ direction.

It is noted from the above observations that the total dislocation density on the primary slip plane increases linearly with the strain. Figure 2-11 shows such a relationship together with the stress-strain curves of the specimens deformed at 1073 K and at the strain rate of $1.4 \times 10^{-5}$ $s^{-1}$. Each circle represents the experimental value averaged over twenty measurements and the vertical line attached to each circle represents the scatter range of the observed value. It is also found that the

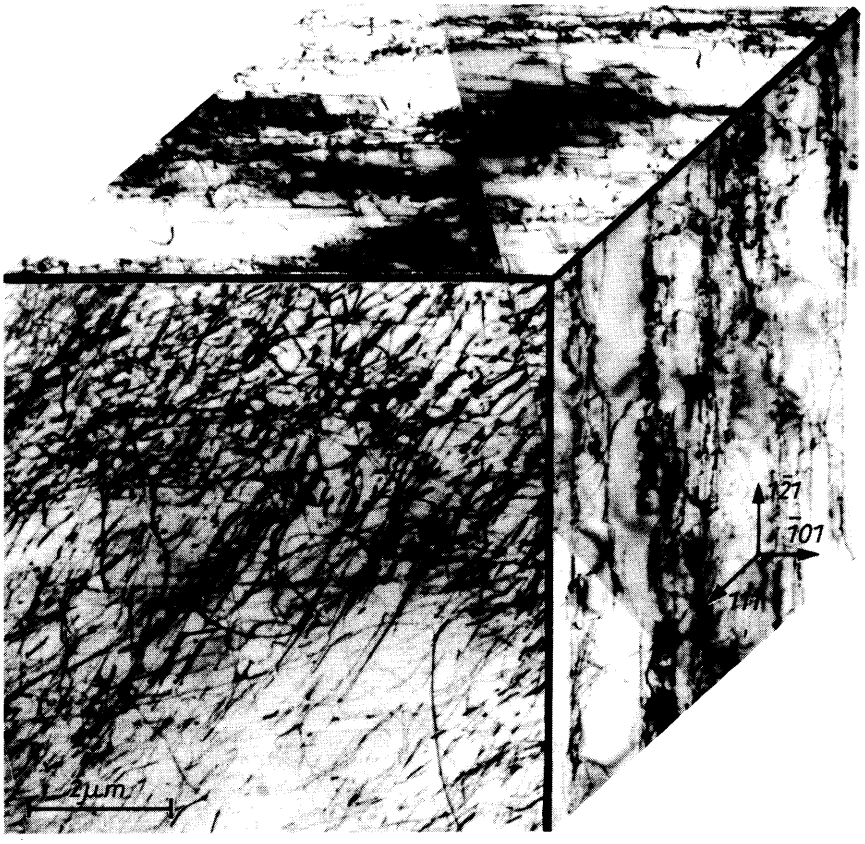


Fig. 2-10. Three-dimensional dislocation configuration in the middle of stage II: resolved shear stress 28.2 $MN/m^2$, shear strain 53.7 %. Crystal faces: (111), $(\bar{1}01)$ and $(1\bar{2}1)$.

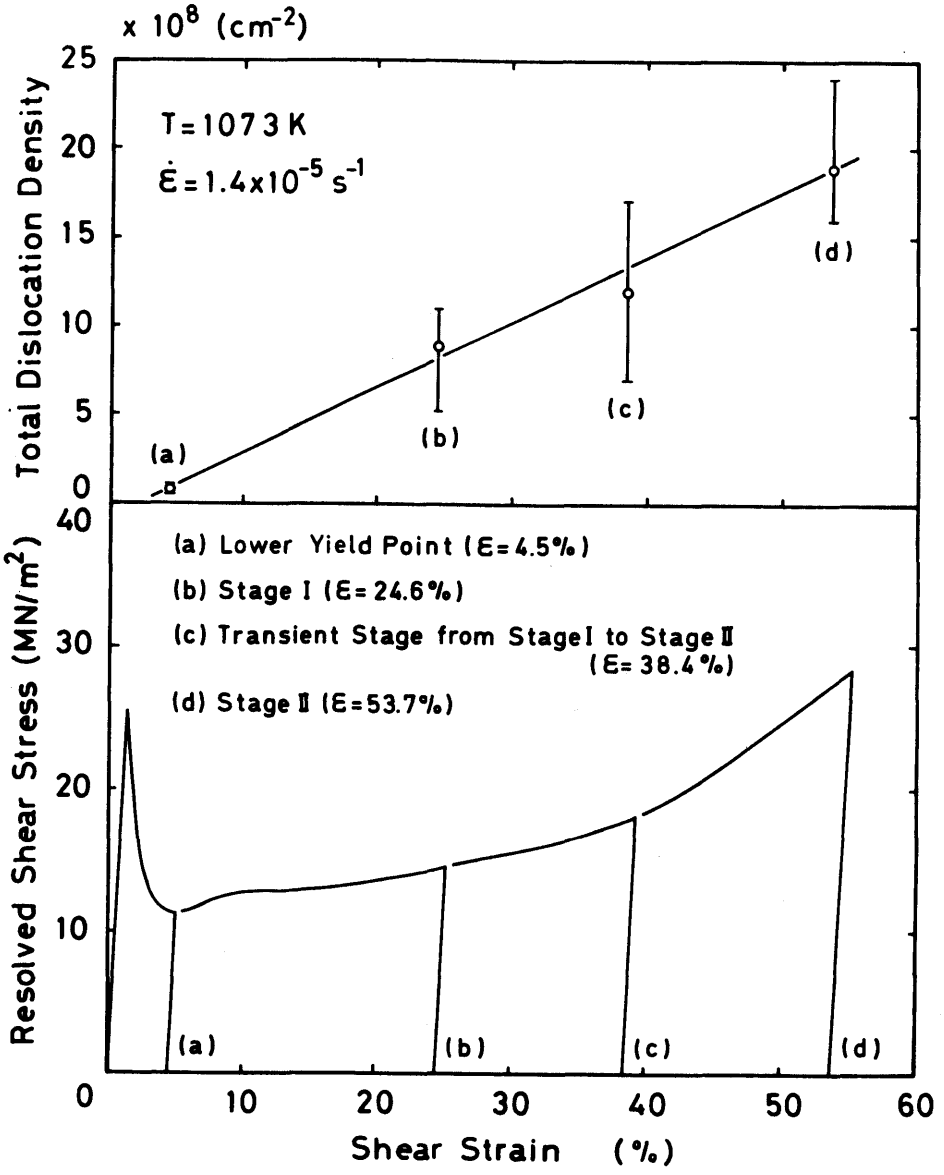


Fig. 2-11. Total dislocation density as a function of shear strain. Stress-strain curves of the specimens deformed at T = 1073 K and the strain rate 1.4 x $10^{-5}$ $s^{-1}$ are also shown; (a) lower yield point (4.5 %), (b) stage I (24.6 %), (c) transient stage from stage I to stage II (38.4 %), (d) stage II (53.7 %).

total dislocation density increases much sharper than proportional to the square of flow stress in stage I and increases linearly with the flow stress in stage II. This relationship agrees well with that obtained by the etch-pit studies of germanium crystals [11]. This figure also shows that the scatter range of the transient stage from stage I to stage II is larger than that of other deformation stages. That is because the dislocation configuration in the transient stage is very inhomogeneous over the primary slip plane. It is supposed, therefore, that work hardening begins inhomogeneously in crystals by the intersections of the primary and the secondary dislocations.

## 2.4. DISCUSSION

The aforementioned observations show that the dislocation configurations at various deformation stages in Czochralski silicon crystals are very similar to those of germanium crystals [12] and also of copper single crystals [13,14]. Accordingly, it leads to a conclusion that there is a close resemblance in the process of work hardening between silicon crystals and f.c.c. metals in spite of the extreme difference in Peierls potential. The similarity may be rationalized by the fact that the diamond cubic lattice is equivalent geometrically to two interpenetrating f.c.c. lattices, so that silicon crystals have the same slip systems and dislocation geometry as f.c.c. metals [15] (see Section 1.2.1.).

Some mechanisms for the hardening effects of oxygen in silicon crystals have been proposed so far in relation of the thermal slip during wafer processing; (i) precipitation hardening by $SiO_2$ particles [16], (ii) dislocation-pinning effect by isolated oxygen atoms and/or their clusters [1,2], (iii) dislocation-locking effect by oxygen atoms [3]. In the present observations, any detectable particles for the motion of dislocations could not be found even by the high-resolution observations. Therefore, it should be the reason for higher mechanical strengths in Czochralski crystals that grown-in and/or nucleated dislocations are locked by oxygen atoms by forming a Cottrell atmosphere around dislocations unless the particular heat treatments are performed.

By the way, although the work-hardening process during plastic deformation has been revealed on the basis of the observed facts mentioned in Section 2.3., the detailed characteristics of dislocation process in the beginning of deformation are not identified at present. It is essential to know the mechanism of generation and multiplication processes of dislocations for understanding the mechanical behaviour of highly perfect crystals.

## REFERENCES

[1] S.M. Hu and W.J. Patrick: J. Appl. Phys. 46 (1975) 1869.

[2] S.M. Hu: Appl. Phys. Lett. 31 (1977) 53.

[3] K. Sumino, H. Harada and I. Yonenaga: Jpn. J. Appl. Phys. 19 (1980) L49.

[4] J.W. Steeds: Proc. R. Soc. London A 292 (1966) 343.

[5] I. Yonenaga and K. Sumino: Phys. Status Solidi (a) 50 (1978) 685.

[6] H. Alexander and P. Haasen: Can. J. Phys. 45 (1967) 1209.

[7] K. Kojima and K. Sumino: J. Phys. Soc. Jpn. 26 (1969) 1213.

[8] H. Mughrabi: Constitutive Equations in Plasticity, ed. A.S. Argon (M.I.T. Press, Cambridge, 1975) p. 199.

[9] A.T. Winter, S. Mahajan and D. Brasen: Philos. Mag. A37 (1978) 315.

[10] S.J. Basinski and Z.S. Basinski: Dislocations in Solids, ed. F.R.N. Nabarro (North-Holland, Amsterdom, 1980) Vol. 4, p. 261.

[11] K. Kojima and K. Sumino: Cryst. Lattice Defects 2 (1971) 147.

[12] H. Alexander: Phys. Status Solidi 27 (1968) 391.

[13] U. Essmann: Phys. Status Solidi 3 (1963) 932; 12 (1965) 707, 723.

[14] H. Mughrabi: Philos. Mag. 23 (1971) 869, 879, 931.

[15] J.P. Hirth and J. Lothe: Theory of Dislocations (MacGrow-Hill, New York, 1968) p. 353.

[16] V.V. Batavin: Sov. Phys. -Solid State 8 (1967) 2478: Sov. Phys. -Crystallogr. 15 (1970) 100.

# CHAPTER 3

# REAL-TIME X-RAY TOPOGRAPHY

## 3.1. INTRODUCTION

In order to investigate the dynamic properties of dislocations, in particular, mobility and multiplication of dislocations directly, various methods such as dislocation etching [1-3], in-situ electron microscopy [4,5] and X-ray topography [6-9] have been used. Among these methods, X-ray topography is a unique and powerful method which enables one to observe non-destructively the behaviour of dislocations in a bulky specimen.

However, when a conventional X-ray source is used, a long exposure is usually needed to record the diffraction image of dislocations because of the weakness of the X-ray intensity. Therefore, to measure the dislocation velocity, for instance, observations of stationary dislocations before and after the application of a stress pulse of a fixed time-interval have been made so far.

By using a recently developed 90 kW-class ultra high intensity X-ray generator or SOR (Synchrotron Orbital Radiation) unit as an X-ray source and by using a TV imaging system [8] as a

detector, it is now possible to observe on a monitor TV screen the image of dislocations moving under an applied stress and to record them continuously on a video tape. For studying the dislocation process of deformation in crystalline materials by real-time X-ray topography, a high-temperature deformation apparatus for use with X-ray topographic goniometer has been newly developed.

The following functions are at least required for the deformation apparatus for real-time X-ray topographic observations : (i) the apparatus can be set on a topographic goniometer stage and a large area of the specimen, for instance, 45 mm in diameter (in the present apparatus) can be studied, (ii) a load-displacement curve can be recorded in parallel with recording of images of moving dislocations, (iii) the specimen can be stretched smoothly along a single axis with a given constant strain rate, (iv) studies can be made in any environmental gas atmosphere or in vacuum at any desired temperature below 1273 K (in the present case), (v) the Bragg condition should be kept or, if necessary, adjusted during deformation.

The purpose of the experimental study described in this chapter is to construct the high-temperature deformation apparatus which satisfies the aforementioned requirements. In the following, the design and the functional features of the apparatus are described in some detail. A TV-VTR system is employed to record continuously the dynamical phenomena occurring in a bulk crystal.

## 3.2. HIGH-TEMPERATURE DEFORMATION APPARATUS FOR DYNAMIC OBSERVATION

### 3.2.1. Detailed Design of Deformation Apparatus

Figures 3-1 (a) and (b) show the whole view and a schematic illustration of the high-temperature deformation apparatus, respectively. This apparatus is composed of three parts: (i) the part for heating the specimen, (ii) the part for straining the specimen in an environmental gas or vacuum and (iii) the part for measuring the applied load and elongation of the specimen. All the parts of the apparatus are made of stainless steel except the tension grips which are made of Inconel. Any temperature up to 1273 K can be obtained with an alumina ring furnace in which Ni-Cr wire of 0.4 mm in diameter is wounded along the alumina ring. This furnace is set close to the specimen but does not interfere with incident and reflected X-ray beams. After mounting the specimen, both sides of the alumina ring furnace facing the X-ray windows are covered with thin nickel foil for heat shielding. The temperature of the specimen is measured by a Pt-PtRh thermocouple located close to one end of the specimen and can be kept constant with accuracy of $\pm$ 1 K. The water-cooled specimen chamber has two beryllium windows of 45 mm in diameter to pass through incident and reflected X-ray beams and is evacuated to about $2 \times 10^{-3}$ Pa or filled with any environmental gas.

The straining mechanism is in principle similar to that of

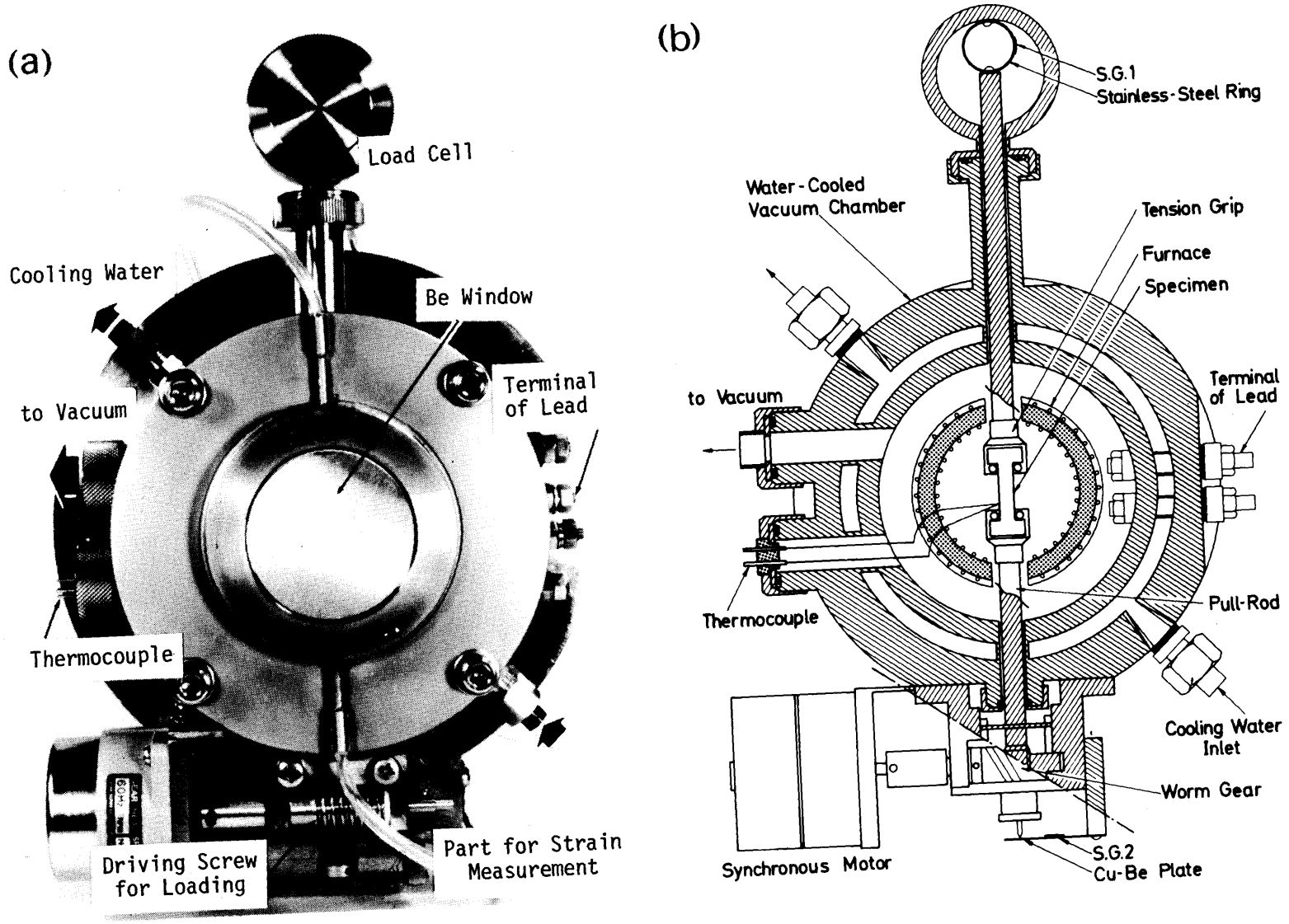


Fig. 3-1. Whole view (a) and schematic illustration (b) of high-temperature deformation apparatus for real-time X-ray topography.

an Instron-type tensile machine, so that the apparatus is of a hard type. The motion of the pull rod is activated by rotating the micrometer screw, which is driven by a synchronous motor ( 1 - 6 r.p.m.) through the worm gear. A load-displacement curve is recorded on an X-Y recorder in parallel with tensile deformation. For this purpose two sets of strain gauges, S.G.1 and S.G.2, are used. In this case, one set of strain gauges (S.G.1) is glued on a stainless steel ring attached to the upper rod of the apparatus and it serves as a load cell. On loading, the ring is deformed elastically to an amount corresponding to the force applied to the specimen. An example of a calibration curve of the load cell is reproduced in Fig. 3-2. With this load cell, measurements of load from 0.5 N to 80 N are possible and the liniarity is exceedingly good. In the practical measurement, the output voltage is increased by one hundred times with the use of a strain amplifier. The other set of strain gauges (S.G.2) is glued on a thin plate of Cu-Be alloy attached to the apparatus. As the lower pull rod moves downward, the plate is bend elastically to an amount corresponding to the displacement of the pull rod (that is, the elongation of the specimen). The calibration curve of the displacement of the pull rod is similar to that for the load cell. The output signals from two sets of strain gauges (S.G.1 and S.G.2) are fed into an X-Y recorder to record a load-displacement curve automatically. Therefore, deformation stages (stage I, II and III) of crystal being deformed can be easily identified along a load-displacement curve.

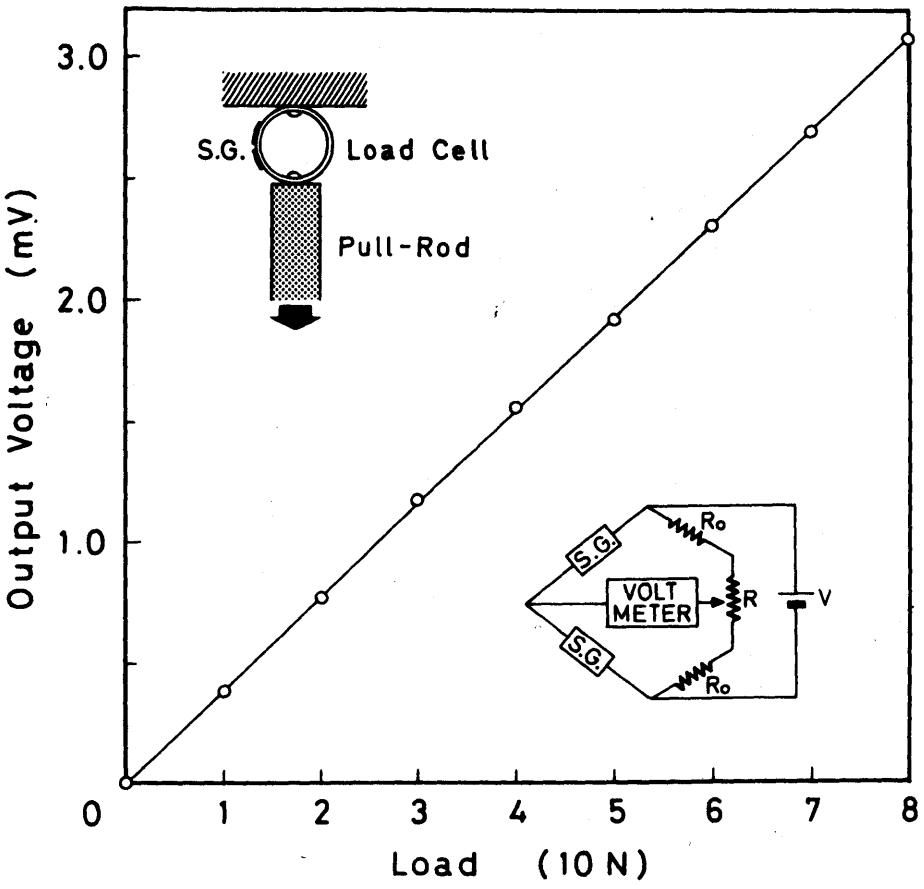


Fig. 3-2. An example of a calibration curve of output voltage from the strain gauges (S.G.1) versus load applied to the stainless-steel ring.

For adjusting the Bragg condition, the rotation of the specimen about an axis perpendicular to the crystal surface and also the rotation about an axis parallel to an intersection of the crystal surface and the reflection plane, can be made after setting this deformation apparatus on the topographic goniometer stage which enables θ-rotation. This apparatus has the following functional features; the maximum heating temperature: 1273 K, the maximum applied load: 80 N, the deformation speed range: $1.7 \times 10^{-2}$ to $1.0 \times 10^{-1}$ mm/min.

Figures 3-3 (a) and (b) show the whole view and a schematic illustration of the high-temperature deformation apparatus of modified type, respectively. The outer wall of this vacuum chamber is shaped as thin as possible so as to reduce the weight of the apparatus. In this case, the motion of the pull rod is performed through the crossheads which slide along the guide rods with ball bushings. As a result, the glide motion of crossheads becomes extremely smooth and no bending of the specimen occurs during tensile deformation. Axial alignment becomes much easier than the former. The depth of the vacuum chamber, i.e., the distance between the two berylium windows was made thin enough to get better resolution. On the one hand, since the wall thickness of the apparatus was made thinner, the inner volume of the apparatus became wider so as to make specimen-exchange easier. As regard the resistant wire, instead of using Ni-Cr wire, kantal wire was used, so that the maximum usable temperature became 1373 K. The straining mechanism and the method of measuring a load-displacement curve are the same as

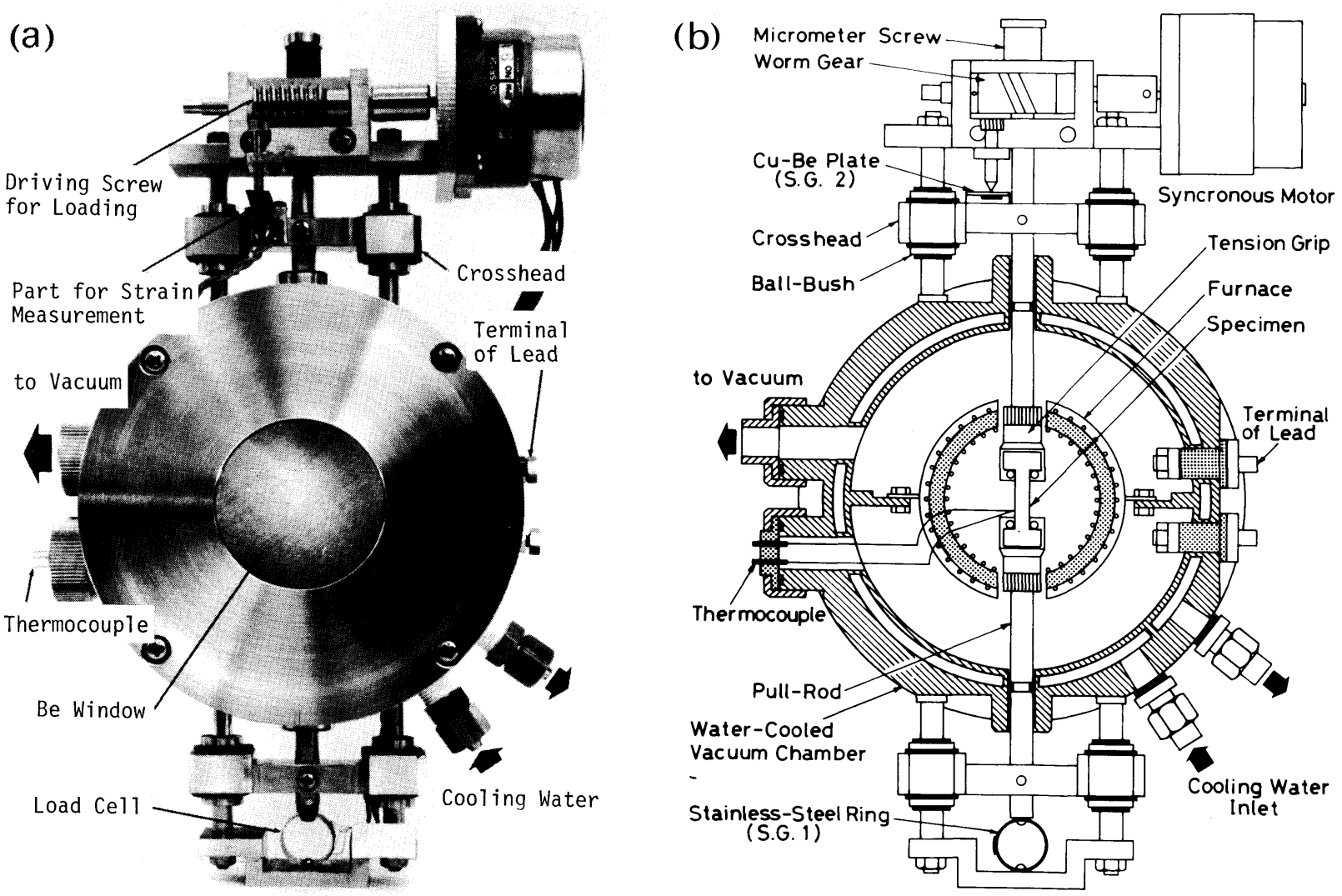


Fig. 3-3. Whole view (a) and schematic illustration (b) of high-temperature deformation apparatus of modified type.

those of the aforementioned apparatus (Fig. 3-1).

### 3.2.2. Tensile Specimens

The specimens used were prepared from dislocation-free silicon single crystals grown both by the Czochralski technique with a growth direction along [100] and by the floating-zone technique with a growth direction along [111]. The concentration of dissolved oxygen atoms in the Czochralski crystal (p-type, 4.3 ohm·cm) was about $1.5 \times 10^{18}$ $cm^{-3}$, according to the infra-red absorption measurements, while that in the float-zone crystal (n-type, $1.3 \times 10^{3}$ ohm·cm) was lower than the detectable limit. Tensile specimens having shoulders at the both ends were prepared with the procedure illustrated in Fig. 3-4, by using a multi-wire saw. At first, a block, for example, 10 x 10 x 25 $mm^3$ with a desired orientation was cut from an ingot of silicon crystal and then the parallel specimen part of a fixed gauge length was made by means of wire cutting as shown in Fig. 3-4. Finally, the block was cut into slices of about 1 mm thick with the aid of a multi-wire saw. In this case, the

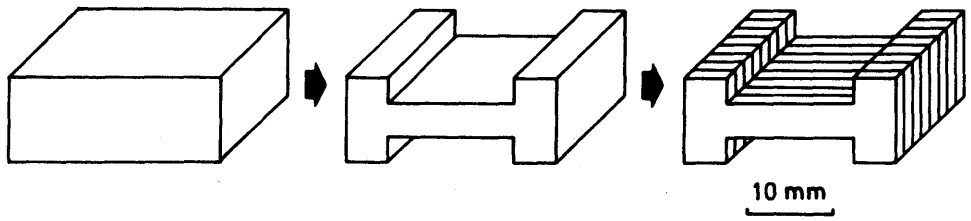


Fig. 3-4. Schematic illustration of the procedure for preparing tensile specimens having shoulders at the both ends.

tensile axis was parallel to [1$\bar{1}$0] and the surface orientation parallel to (112). Each specimen was mechanically polished with a mixture of water and alumina powders of 800 mesh, followed by chemical polishing using an etchant of 1 part HF and 5 parts $HNO_3$ (by volume) to the depth of 100 μm below each surface until surface damages were removed. The final polish was made carefully to get smooth surface by stirring the solution. The specimen thus obtained had a gauge length of about 15 mm, a width of about 4 mm and a thickness of 0.7 - 0.8 mm.

For application of a uniaxial tensile load, the specimen was held by the tension grips of the deformation apparatus, as shown in Fig. 3-5. On applying a tensile load, the stress was distributed homogeneously through the gauge length. There are two activated slip planes. ($\bar{1}$11) and (1$\bar{1}$1), in this orientation of specimen and four slip systems, [0$\bar{1}$1]/($\bar{1}$11), [101]/($\bar{1}$11), [$\bar{1}$01]/(1$\bar{1}$1) and [011]/(1$\bar{1}$1), had the maximum Schmid factor.

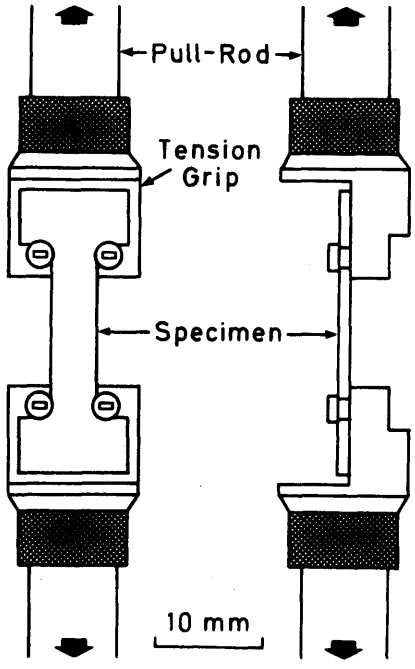


Fig. 3-5. Schematic illustration of tension grips with a specimen attached to them.

## 3.3. TV IMAGING SYSTEM

A block diagram of the TV imaging system is shown in Fig. 3-6. The TV system consists of a TV camera unit with a PbO vidicon tube (Hamamatsu T.V., N-603), video amplifier, camera control unit and TV monitor operating as a normal closed-circuit TV system. TV frame speed is a standard one, i.e., 30 frame/s. By orientating the crystal so as to satisfy the Bragg condition for the slightly divergent X-ray incident beam, two images due to the diffracted $K\alpha_1$ and $K\alpha_2$ beams, each with a width of 1 mm, are received by the vidicon tube. These two rectangular regions of the crystal are imaged simultaneously with a magnification of about 20 times on the monitor TV screen. Such images are called "direct-view image" [10]. To image larger areas of the crystal, the video signals due to the $K\alpha_1$ image is selected by the electric slit unit and stored in the image storage unit while the carriage is moved for about 10 s. The position of the electric slit is moved in synchronization with the carriage motion. The initial position, slit width and traversing speed are adjusted during viewing the topographic images on the monitor TV screen. A Lang traverse topograph over an area 9 x 12 $mm^2$ in the crystal is displayed on the monitor TV screen after each scan. Such images are, hereafter, referred to as "synthesized image" [10]. The direct viewing is made for $K\alpha_1$ and $K\alpha_2$ radiations while the synthesized images are obtained only with $K\alpha_1$ image of 1 mm width.

For the dynamic observation of dislocation processes at

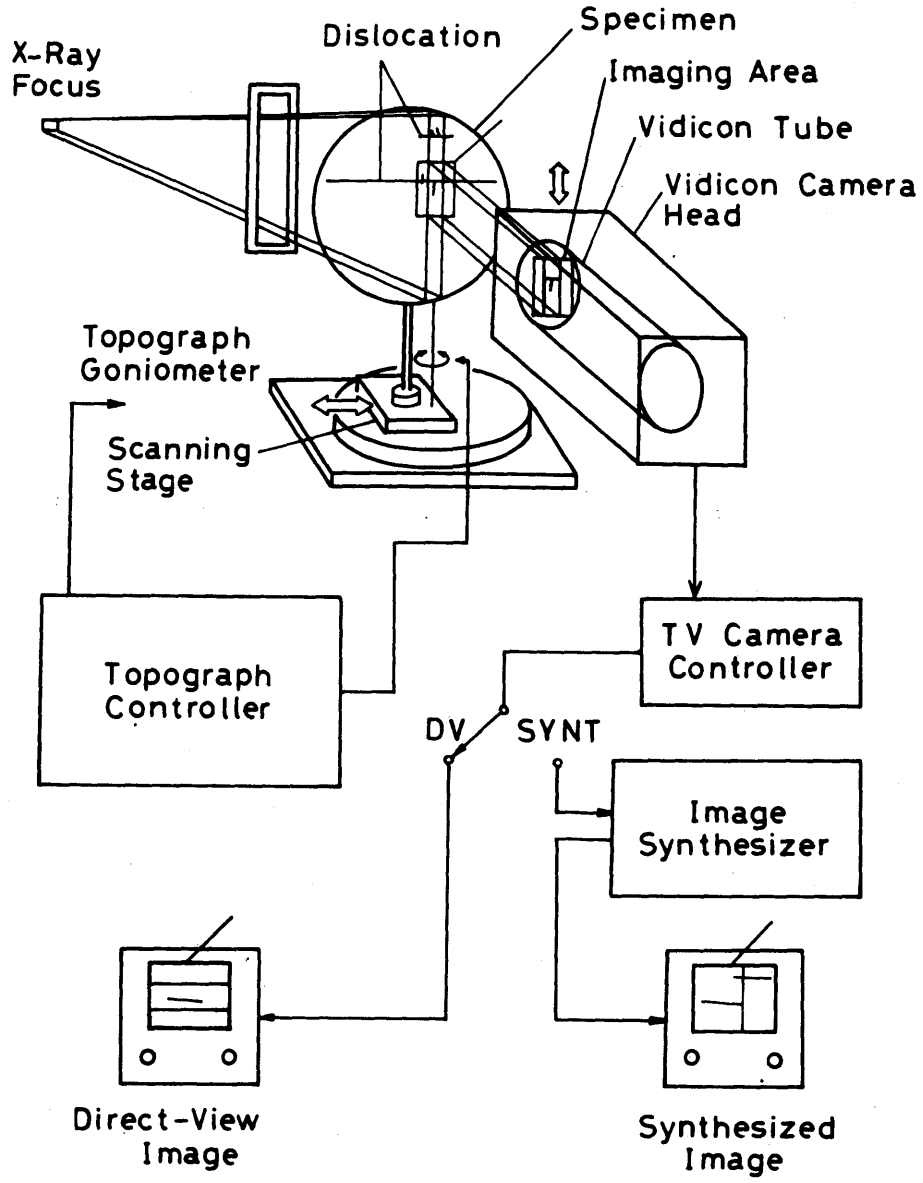


Fig. 3-6. Schematic diagram of TV imaging system for X-ray topography.

elevated temperature under controlled stress, the aforementioned high-temperature deformation apparatus (Fig. 3-1, Fig. 3-3) was combined with an X-ray diffraction topographic system which consisted of a 90 kW-class ultra high intensity X-ray generator ( Rigaku, RU-1500), a large topographic goniometer and a TV imaging system (Fig. 3-6). The generator with a Ag rotating target was operated at 50 kV, 1200 mA and a bias voltage of 1000 V and Ag $K\alpha_1$ radiation was used for the topography. The effective size of the focus was 1.0 x 1.0 $mm^2$, so that geometrical resolution was 3 μm in the horizontal direction and 25 μm in the vertical direction. The experimental arrangement is shown schematically in Fig. 3-7. Either symmetric 220 reflection or 111 reflection of X-rays was employed for real-time observations. The dynamic phenomena occurring in bulk crystals were continuously observed on the screen of monitor TV and video images were recorded by a video tape recorder (VTR) in parallel with observation. The resolution of the TV system was lower than the geometrical one; the resolution of the TV camera is of the order of 20 μm. Therefore, to reveal the details of dislocation configurations and also to determine the Burgers vector of dislocations by the invisibility criterion [11], the images were also recorded intermittently on Ilford-L4 nuclear research plate.

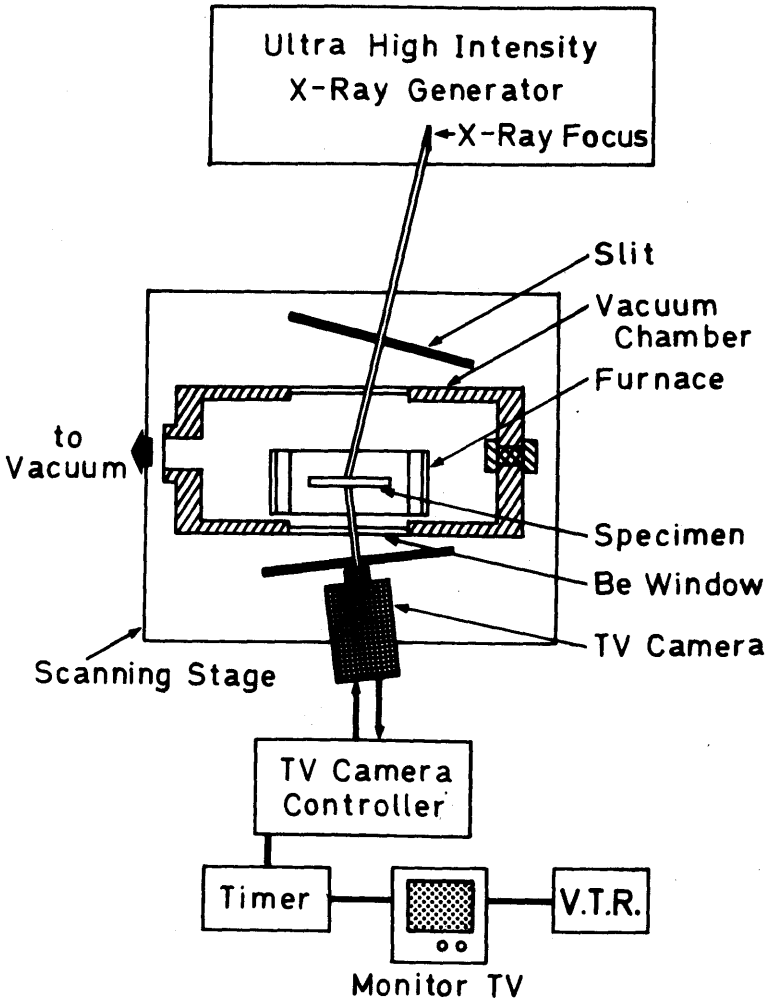


Fig. 3-7. Scematic diagram of real-time X-ray topography arrangement for high-temperature experiment in transmission geometry.

## REFERENCES


[1] W.G. Johnston and J.J. Gilman: J. Appl. Phys. 30 (1959) 129.

[2] D.F. Stein and J.R. Low, Jr.: J. Appl. Phys. 31 (1960) 362.

[3] K. Marukawa: J. Phys. Soc. Jpn. 22 (1967) 499.

[4] H. Saka and T. Imura: J. Phys. Soc. Jpn. 32 (1972) 702.

[5] H. Saka, K. Noda and T. Imura: Cryst. Lattice Defects 4 (1972) 702.

[6] T. Suzuki and H. Kojima: Acta Metall. 14 (1966) 913.

[7] F.W. Young, Jr. and F.A. Scherrill: J. Appl. Phys. 42 (1971) 230.

[8] J. Chikawa, I. Fujimoto and T. Abe: Appl. Phys. Lett. 21 (1972) 295.

[9] K. Sumino and H. Harada: Philos. Mag. 44 (1981) 1319.

[10] J. Chikawa and I. Fujimoto: NHK Technical Monograph (1974) No. 23.

[11] A.E. Jenkinson and A.R. Lang: Direct Observation of Imperfections in Crystals, eds. J.B. Newkirk and J.H. Wernick (Interscience, New York, 1962) p. 471.

# CHAPTER 4

# TEMPERATURE DEPENDENCE OF FRICTION FORCE ACTING ON DISLOCATIONS

## 4.1. INTRODUCTION

Silicon crystal is a typical crystalline material in which the Peierls-Nabarro barrier for dislocation motion is extremely large because of the covalent bonding [1]. In such a crystal, thermal fluctuations assist the applied stress in letting a dislocation past the barrier. It has been shown by X-ray topography that the mobility of dislocations in silicon crystals is much lower than those in other types of crystals and that the dislocation velocity is sensitive to the temperature but rather insensitive to the stress [2-7]. The dislocation velocity v in silicon crystals is expressed approximately with an equation:

$$v = B_o \tau^m \exp(-E / kT) \qquad (4.1)$$

where $\tau$ is the applied shear stress, T the temperature and k the Boltzmann constant. According to the in-situ X-ray topographic observations [7,8], the magnitudes of E estimated are 2.1 $\pm$ 0.1

eV for screw dislocation and 2.2 ± 0.15 eV for 60° dislocation, and the magnitude of m is 1.1 ± 0.1 for both types of dislocations. It has been also disclosed that dislocations in float-zone crystals move at velocities given by Eq. (4.1) under applied stresses above 1.5 $MN/m^2$ [7,8]. The dislocation behaviours there are those under external stress.

It is known that expanded dislocation half-loops shrink during annealing at elevated temperatures [9-11] and that the driving forces of this process are image forces and line tension. It is also expected that dislocations inside the crystals can move under the elastic interaction forces between dislocations at fairly high temperatures, overcoming the Peierls-Nabarro barrier. These movements of dislocations under the elastic interaction forces are the unique one which takes place at much lower stress level than in the previous dislocation-velocity measurements. Because of this dislocation motion, the shape of dislocation half-loops is considered to change gradually with increasing annealing temperature so as to balance the interaction force between dislocations with the friction force acting on these dislocations.

The purpose of the experimental study described in this chapter is to investigate the motion of individual dislocations in silicon crystals during annealing by means of in-situ X-ray topographic observations. From the changes in dislocation configurations at elevated temperatures, the friction forces acting on respective dislocation segments are estimated as a function of annealing temperature.

## 4.2. EXPERIMENTAL PROCEDURES

### Specimen Preparation

Specimens were prepared from dislocation-free silicon crystals (n-type, 1.3 x $10^3$ ohm.cm) grown by the floating-zone technique. Shoulder-type specimens were prepared by means of wire-cutting, in the same manner as described in Section 3.2.2. These specimens had a gauge length of 15 mm, a width of 4 mm and a thickness of 1 mm; tensile axis parallel to [1$\bar{1}$0] and surface orientation parallel to (112). Each specimen was mechanically polished and then the surface damaged layers were removed by chamical polishing; the final thickness of specimens was 0.7 - 0.8 mm.

### Introduction of Isolated Dislocation Half-Loops

The preferential nucleation sites for dislocations were introduced intentionally by scratching the (112) surface with a diamond needle, the line direction of which is perpendicular to the direction of the trace of (1$\bar{1}$1) planes. The scratched specimens were held at 1023 K under the applied stress of about 2.5 $MN/m^2$ for 10 min, so that many dislocation half-loops were nucleated at the scratch. At this stage, however, the density of dislocations in the vicinity of the scratch was too high for the individual dislocations to be resolved on X-ray topograph. Therefore, the scratch was polished off after cooling by chemical polishing to reduce the dislocation density. The specimens, having isolated dislocation half-loops, were again loaded at

1073 K under an applied stress between 1.0 - 4.0 $MN/m^2$ and held for 10 min under each stress to permit the isolated dislocation half-loops to expand to such an extent that they can be resolved by X-ray topography.

In-Situ X-Ray Topographic Observations

The motion of isolated dislocation half-loops during annealing at elevated temepratures was observed in-situ using the specimen heating apparatus [12] described in Section 3.2, installed on a high-power X-ray diffraction topographic system. The specimens were annealed stepwise between 1173 K and 1273 K in vacuum; they were annealed for 30 min at each temperature. Ag $K\alpha_1$ radiation was used for the topography under the operating condition of 50 kV and 1200 mA and symmetric 111 reflection was employed. The motion of dislocations was observed continuously on a monitor TV; to reveal the details of dislocation configurations, the images were also recorded intermittently on Ilford-L4 nuclear research plates. The exposure time for a traverse topograph was about 1 min.

## 4.3. EXPERIMENTAL RESULTS

### 4.3.1. Generation of Isolated Dislocation Half-Loops

Large isolated dislocation half-loops were introduced by tensile deformation from the scratch made on the surface, as

shown in Fig. 4-1. Figures 4-2 (a) and (b) show the topographs taken at room temperature on the specimen stressed up to 3.6 $MN/m^2$ for 10 min at 1073 K. The dislocation half-loops consist of four straight segments lying along the <110> directions and the maximum loop diameter is about 2 mm in this case. Contrast experiment and trace analysis showed that dislocations generated from the scratch mostly belong to either the $[0\bar{1}1]/(\bar{1}11)$ slip system or the $[10\bar{1}]/(1\bar{1}1)$ slip system. From the dislocation configurations, the process for this multiplication is identified to be the Frank-Read mechanism with a single pole [13]. The multiplication was usually observed to take place in the vicinity of the intersection point of the two dislocations moving on non-parallel slip planes. For the observation of the motion of isolated dislocations which are not disturbed by other dislocations, hereafter, the analysis of annealing effects was performed on the dislocations near which the multiplication did not take place.

### 4.3.2. Motion of Isolated Dislocations during Annealing

The specimens, in which isolated dislocation loops were introduced at 1073 K, were again heated to a temperature between 1173 K and 1273 K and the changes in dislocation configurations during annealing were observed continuously, as shown in Fig. 4-3. Figure 4-3 (a) is the topograph taken at room temperature before heating. As was found in Fig. 4-2, large dislocation loops, which assume a half-hexagonal shape, were observed. The

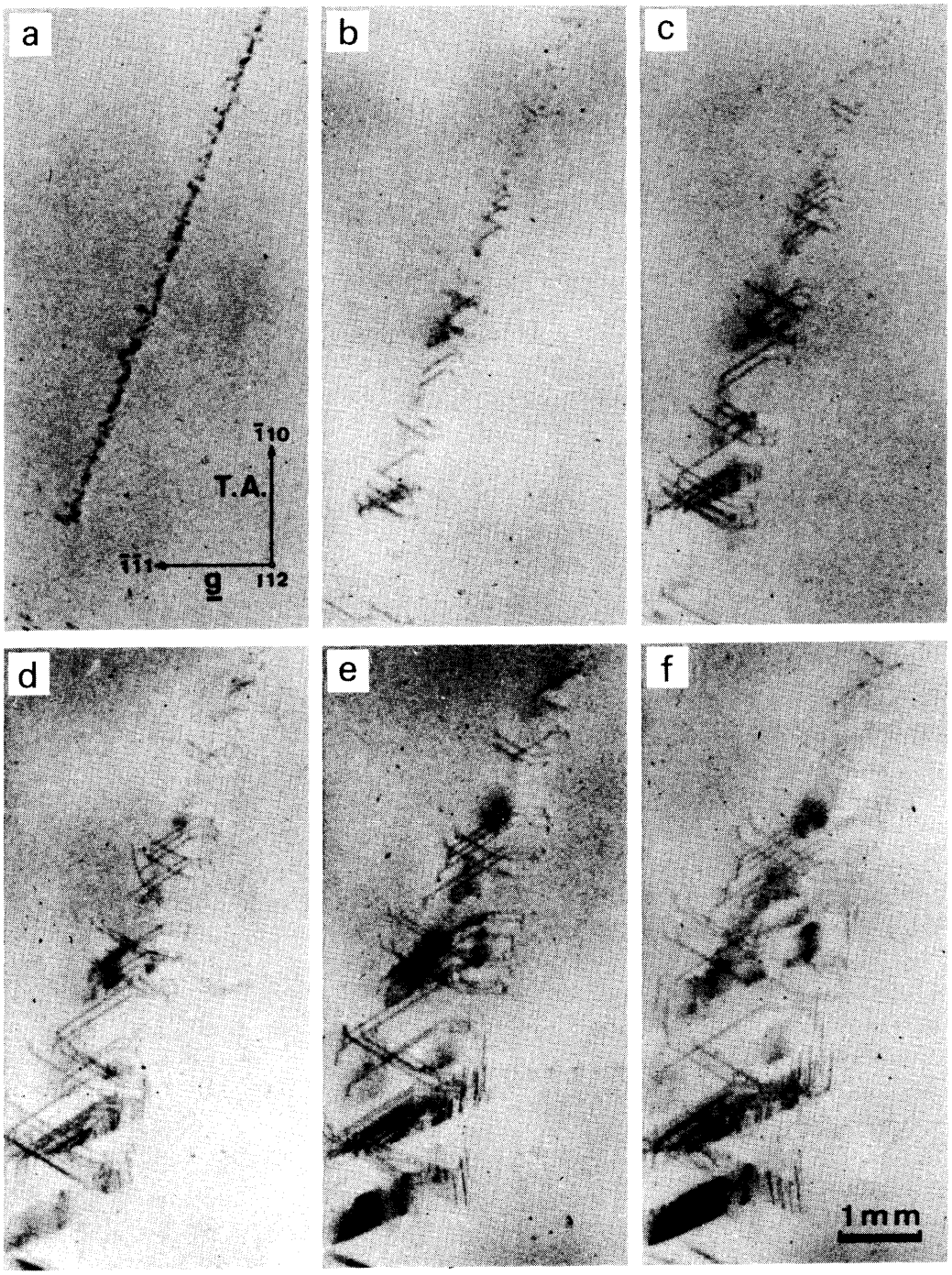


Fig. 4-1. Generation of dislocation half-loops from the scratch during tensile deformation at 1073 K. Topographs were taken at the applied stresses of 2.0 MN/m$^2$ (a), 2.5 MN/m$^2$ (b), 2.8 MN/m$^2$ (c), 3.2 MN/m$^2$ (d) and 3.6 MN/m$^2$ (e) after holing for 10 min at each stress: $\bar{1}\bar{1}1$ reflection.

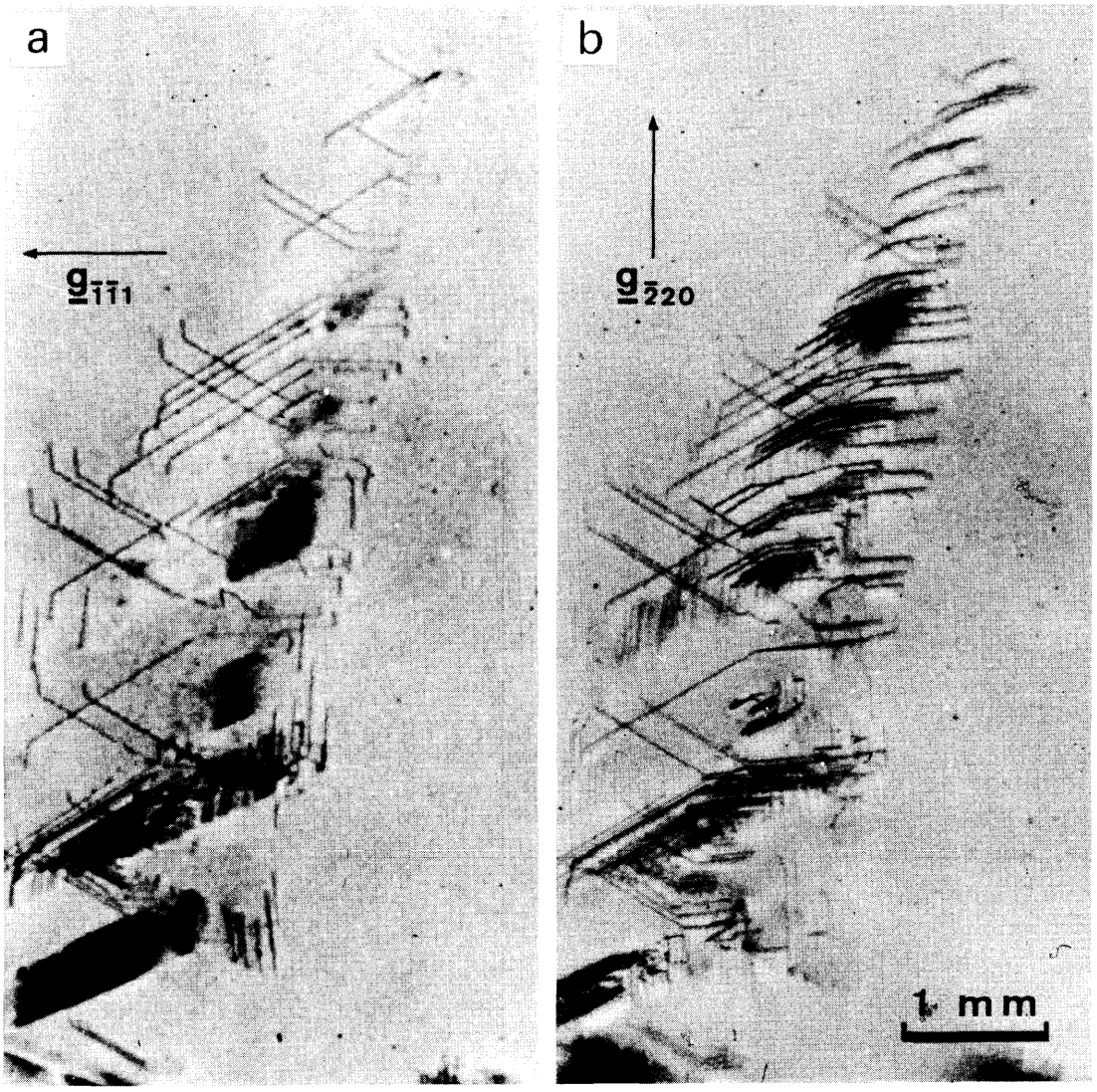


Fig. 4-2. Large isolated dislocation half-loops expanded from the scratch by tensile deformation at 1073 K. Topographs were taken at room temperature after the applied stress was increased up to 3.6 $MN/m^2$ and then holding there for 10 min: (a) $\bar{1}\bar{1}1$ reflection, (b) $\bar{2}20$ reflection.

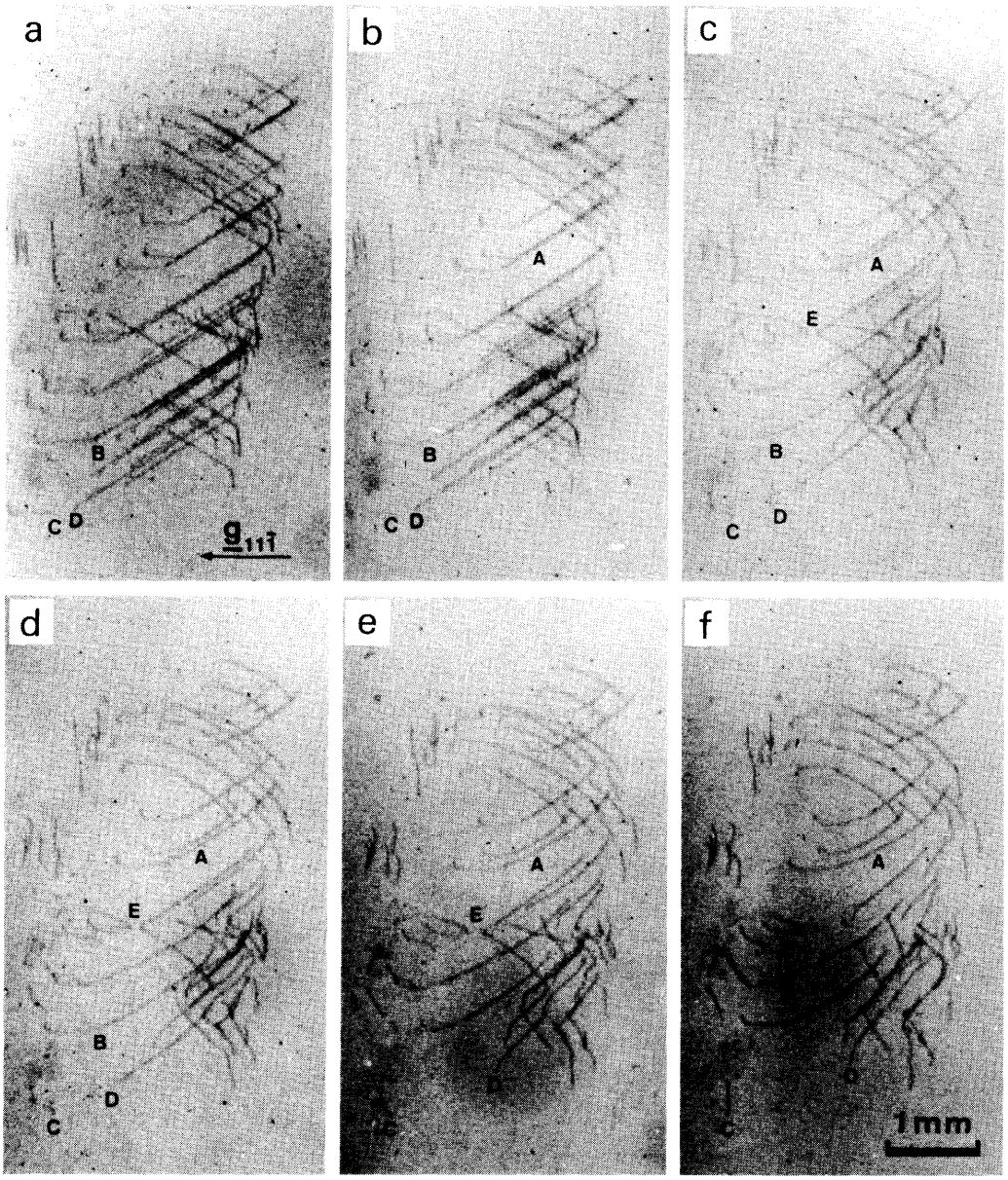


Fig. 4-3. Evolution of dislocation configurations during annealing. (a) is the topograph taken at room temperature before heating. The specimen was held at 1173 K for 30 min (b), at 1223 K for 30 min (c), and then at 1273 K for 10 min (d), 20 min (e) and 30 min (f): $11\bar{1}$ reflection.

specimen was heated to 1173 K at a heating rate of about 100 K/min and held at that temperature for 30 min (b), and then at 1223 K for additional 30 min (c). The specimen was subsequently heated up to 1273 K and held there for 10 min (d), 20 min (e) and 30 min (f).

It can be seen from these topographs that initially straight dislocation segments, which were strictly parallel to the <110> direction, turned into slightly curved ones. The shape of the loops after annealing is half-elliptical with the long axis parallel to the Burgers vector, i.e. the screw direction, and the radius of curvature of the edge segments $R_e$ was always smaller than that of the screw segments $R_s$. This and other noticeable features in dislocation movements during annealing are summarized as follows;

(i) Repulsive interaction between parallel screw dislocations with the same sign can be seen at A. As a result, the distance between two dislocations became longer at higher annealing temperature.

(ii) Displacement in position of the portion corresponding to one of the vertexes of a hexagonal loop can be seen at B; the portion is referred to as the dislocation bend [14] in the following. That is to say, the sharp dislocation bend turned into the gradually curved bend.

(iii) Movement of dislocations which are intersected with surface can be seen at C and D, where the 60° segment terminated at the surface at the point A and the screw segment at B since the portion corresponding to the vertex of a hexagonal loop had

slipped out of the crystal during tensile deformation. Both the 60° and the screw segments emerging at the surface moved gradually during annealing and eventually they were intersected with the surface perpendicularly.

(iv) Attractive reaction between dislocations on non-parallel slip planes can be seen at E, and this reation leads to the formation of Lomer dislocations.

### 4.3.3. Estimation of Friction Force as a Function of Temperature

As was observed in Fig. 4-3, isolated dislocations move during annealing at elevated temperatures under the influences of the elastic interaction force between dislocations and of the image force near the surface. However, the friction force acting on dislocations prevents the aforementioned motion of dislocations, and consequently the dislocation segments assume an equilibrium position at each temperature so as to balance the friction force with the interaction force between dislocations and the image force. Accordingly, it is possible to estimate the friction force from the configurational changes of dislocations during annealing.

In this section, the friction forces are determined as a function of annealing temperature by analyzing (i) the repulsive interaction force between parallel screw dislocations with the same sign and (ii) the interaction forces caused by the other segments of the same dislocation half-loop (dislocation bend).

Estimation of Friction Force from Repulsive Interaction between Parallel Dislocations with the Same Sign

Figures 4-4 (a),(b) and (c) show the topographs of the specimen which was annealed stepwise at 1173 K for 30 min (a), at 1223 K for 30 min (b) and at 1273 K for 10 min (c), respectively. It can be seen that the repulsive interaction between two parallel screw dislocations was realized with increasing annealing temperature, as indicated by the white arrows. Figure 4-4 (d) is a schematic illustration of Fig. 4-4 (c). From the trace analysis as shown by dotted line, it is found that the distance between the two slip planes, on which the two dislocation half-loops lie, is extremely small since the surface traces of two half-loops almost coincide with each other. When two parallel screw dislocations with the same sign are on the same slip plane, the repulsive interaction force between these dislocations per unit length is given by

$$F/L = \mu b^2 / 2\pi \Delta d \qquad (4.2)$$

where $\Delta d$ is the distance between the two screw dislocations on the same slip plane, b the Burgers vector of the screw dislocation, L the length of the dislocation and $\mu$ the shear modulus. By measuring the distance $\Delta d$ at each temperature, the repulsive interaction force between the two screw dislocations are estimated from Eq. (4-2) as a function of annealing temperature. Although the two screw dislocations repel each other due to this interaction force, however, the friction force acts so as to prevent this repulsive motion of dislocations. In a state of

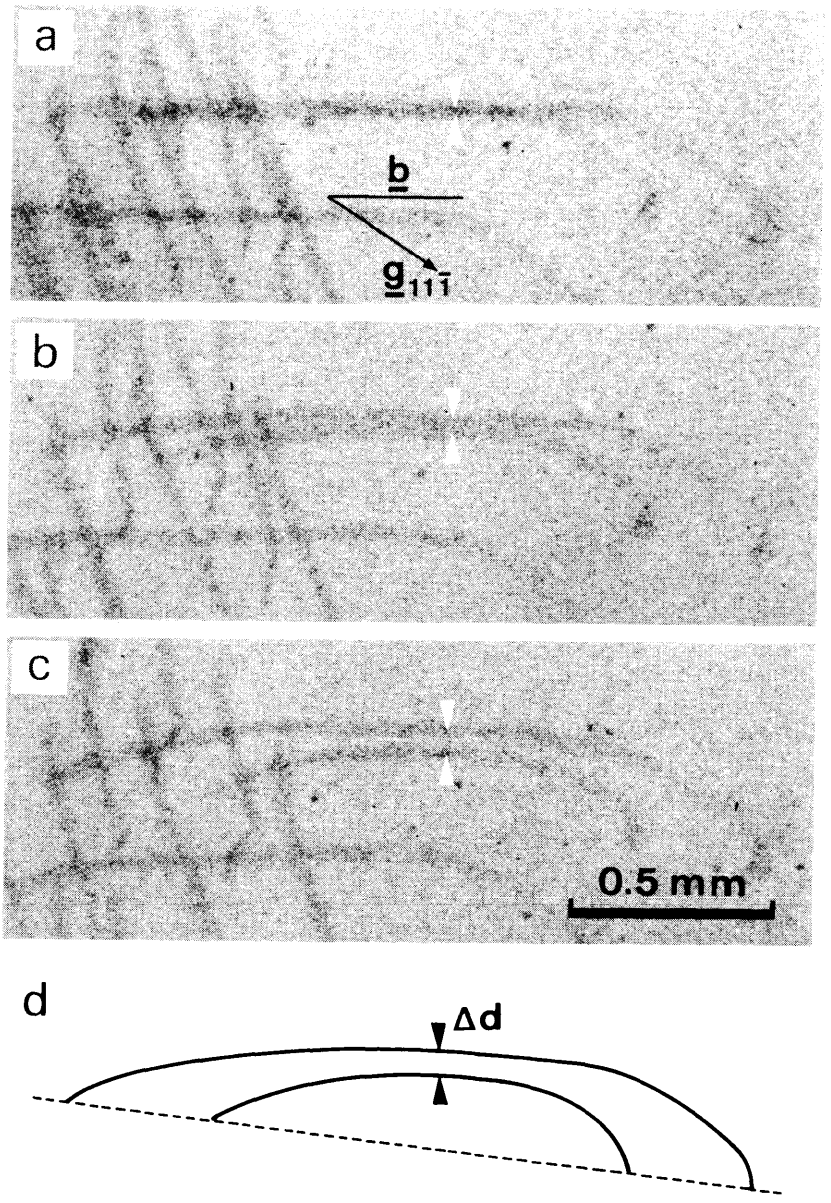


Fig. 4-4. Repulsive interaction between parallel screw dislocations at elevated temperatures. Topographs of the specimen annealed stepwise at 1173 K for 30 min (a), at 1223 K for 30 min (b) and at 1273 K for 10 min (c): 11$\bar{1}$ reflection. Each set of white arrows indicates the distance Δd between two dislocations. b: Burgers vector. Schematic illustration of (c) is shown in (d); the dotted line represents the surface trace.

equilibration at each annealing temperature, the repulsive interaction force between two screw dislocations is balanced with the friction force acting on each of them. Here, it should be noticed that near one of the surfaces the dislocation may get the effects of image force with the increase in the distance $\Delta d$. This can be seen at A in Fig. 4-3 (e) and (f), where the two screw dislocations unusually repelled each other with time at 1273 K. Such being the case, the measurement of the distance $\Delta d$ at 1273 K was attempted on the specimen annealed for 10 min (Fig. 4-4 (c)). The friction forces thus estimated will be shown collectively afterwards.

Estimation of Friction Force from Configurational Changes of Dislocation Half-Loop (Dislocation Bend)

Figures 4-5 (a),(b) and (c) show the topographs taken at 1173 K (a), 1198 K (b) and 1223 K (c), respectively, each of which was observed after holding for 30 min at each temperature. In the same manner as in Fig. 4-3, the sharp dislocation bend turned into the gradually curved bend with the increase in annealing temperature, as indicated by the white arrows. Figure 4-5 (d) is a schematic illustration of Fig. 4-5 (c) and it represents that the equilibrium configuration of the dislocation bend was changed from the position drawn by a straight broken line to that drawn by a curved solid line after this annealing. Namely, the curvature of the bend became smaller for higher temperature.

Here, it is very convenient to analyze the angular disloca-

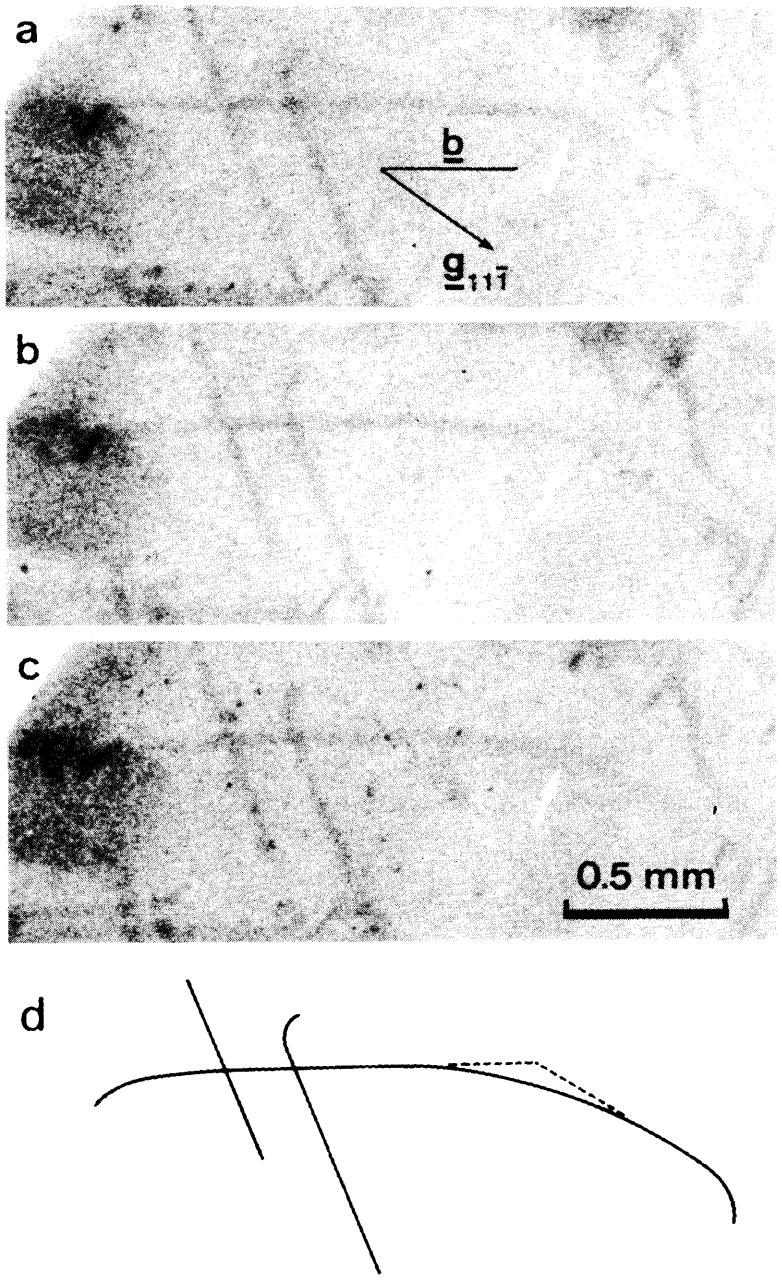


Fig. 4-5. Configurational change of dislocation bend during annealing. Topographs were taken at 1173 K (a), 1198 K (b) and 1223 K (c), respectively, each of which was observed after holding for 30 min at each temperature: 11$\bar{1}$ reflection. The white arrows indicate the dislocation bend and $\underline{b}$ Burgers vector. Schematic illustration of (c) is shown in (d); broken line and solid line represent the position of the dislocation before and after annealing, respectively.

tion shown in Fig. 4-6 since each dislocation segment is strictly parallel to the <110> direction before annealing. By heating the specimen, the dislocation segments near the bend move to adjust their positions because each of straight line segments (1) and (2) of the dislocation is under the influence of the interaction force caused by the other segments of the same dislocation line. In the case of the dislocation bend of angle θ (; the segments (1) and (2) are in directions separated by angle θ) as in Fig. 4-6 (a), the interaction force per unit length on the dislocation (1) at a distance $l$ from the bend P is given by [14]*

$$\frac{F_2}{L} = \frac{\mu}{4\pi l}\left[b_s^2\left(\frac{\cos\theta - 1}{\sin\theta} - \frac{\nu\sin\theta\cos\theta}{1-\nu}\right) + b_s b_e \frac{2\nu\sin^2\theta}{1-\nu} - b_e^2 \frac{\cos\theta - 1 + \nu\sin^2\theta\cos\theta}{(1-\nu)\sin\theta}\right] \qquad (4.3)$$

where $b_s$ and $b_e$ are the screw and the edge components of the Burgers vector for the dislocation segment (2), L the length of the dislocation segment (1) and ν the Poisson ratio. The distance $l$ is a length from the bend P to the point Q at which the displacement of the segment (1) is ended.

When the sharp dislocation bend turns into the curved one, the segment (1) is also exerted by the force $F_3/L$ which is caused by the curved dislocation segment. In order to determine this force, the curved segment is approximated by the straight line segments (1),(2) and (3), as shown in Fig. 4-6 (b). This

* Lothe [15] has shown that the force $F_2/L$ can be derived from simple line-tension considerations.

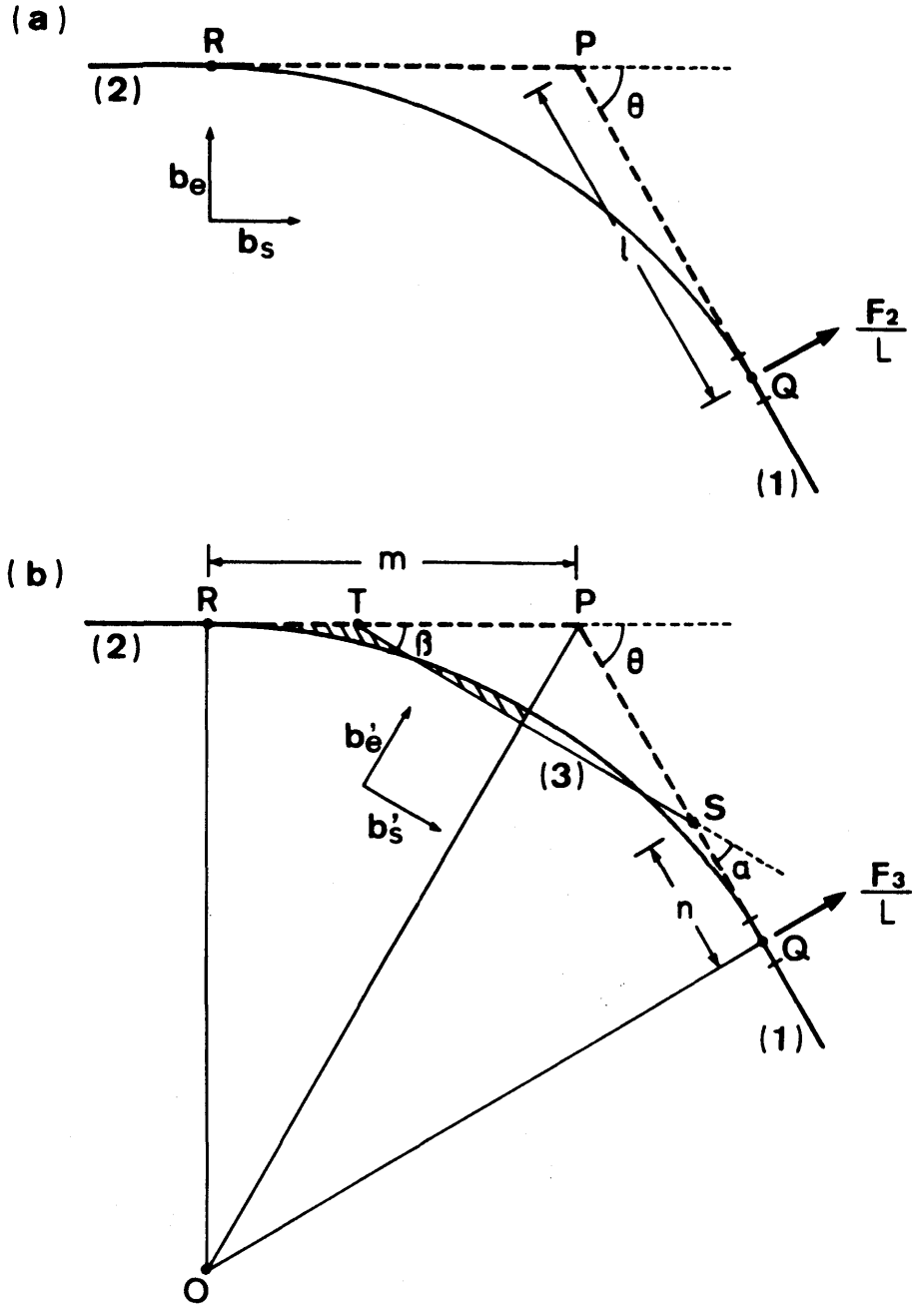


Fig. 4-6. (a) Schematic diagram showing dislocation bend of angle θ. Broken line and solid line represent the position of the dislocation before and after annealing, respectively. (b) Straight-line approximation of curved dislocation segment. Straight line segment (3) is settled so as to equalize the both shaded areas; $n=0.39l$ for $l=m$.

straight line segment (3) is settled so as to equalize the both shaded areas in Fig. 4-6 (b), granting that the distance $m$ is equal to $l$. Then, instead of the distance $l$ in Eq. (4.3), the distance $n$ can be determined to be equal to 0.39 $l$. As a result, the interaction force per unit length on the dislocation (1) at the distance $n$ from the point S, which is exerted by the dislocation segment (3), is derived from the same consideration as that for Eq. (4.3) and given by

$$\frac{F_3}{L} = \frac{\mu}{4\pi n}\left[b_s'^2\left(\frac{\cos\alpha - 1}{\sin\alpha} - \frac{\nu\sin\alpha\cos\alpha}{1-\nu}\right) + b_s'b_e'\frac{2\nu\sin^2\alpha}{1-\nu} - b_e'^2\frac{\cos\alpha - 1 + \nu\sin^2\alpha\cos\alpha}{(1-\nu)\sin\alpha}\right] \tag{4.4}$$

where $b_s'$ and $b_e'$ are the screw and the edge components of the Burgers vector for the dislocation segment (3) and this segment (3) is inclined at angles $\alpha$ and $\beta$ to the segment (1) and (2), respectively. The values of $\alpha$ and $\beta$ can be easily caluculated geometrically.

After all, the resultant interaction force per unit length on the dislocation (1) at the distance $l$ from the bend P is the summation of both $F_2/L$ and $F_3/L$. According to Eqs. (4.3) and (4.4), it is recognized that these forces are infinite at the dislocation bend P, that is, $l = 0$ and become smaller rapidly for the longer distance. Therefore, the dislocation in the vicinity of the bend can move easily due to the large interaction force, while it is very difficult for the segment far from the bend to move. That is to say, the dislocation segment at

the distance $l$ from the bend P does not move anymore due to the resultant interaction force. This means that the resultant interaction force on the dislocation segment at the distance $l$ is now equal to the friction force acting on this segment.

The energy which is supplied by thermal fluctuations to overcome the Peierls-Nabarro barrier would increase in proportion to the increase in annealing temperature. As the dislocation bend turns into a curved one with increasing temperature, the distance $l$ also increases together. By measuring the distance $l$, the friction force for both screw and 60° dislocations can be estimated at each temperature using Eqs. (4.3) and (4.4). Figure 4-7 shows the relation between the friction force acting on dislocations and the annealing temperature for both screw and 60° dislocations. The friction forces estimated previously are also included together in this figure. Each circle represents the experimental value and the virtical line attached to each circle represents the scatter range of the observed value. It is found from this figure that the friction force decreases exponentially as the annealing temperature is increased.

## 4.4. DISCUSSION

### 4.4.1. Annealing Effects on the Motion of Isolated Dislocations

On the basis of the observations mentioned in Section 4.3., two effects on the motion of individual dislocations can be ex-

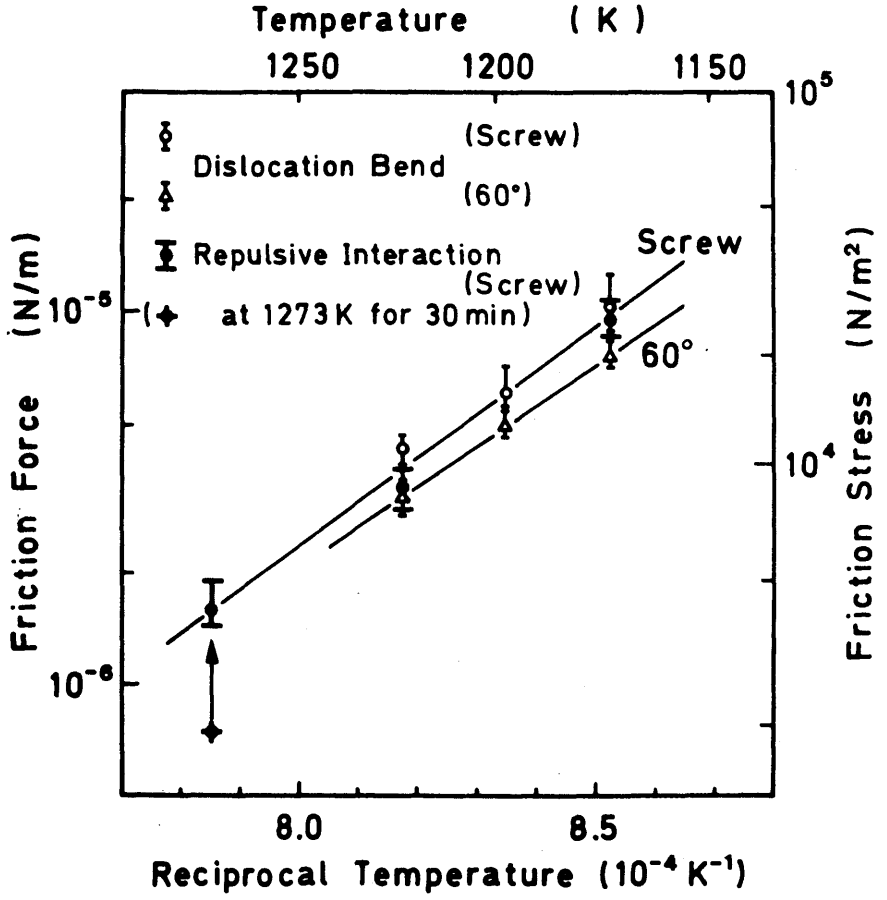


Fig. 4-7. Friction force acting on screw and 60° dislocations as a function of annealing temperature. Friction forces are determined by estimating interaction forces between dislocations from the analysises of (i) repulsive interaction between parallel screw dislocations with the same sign and (ii) configurational changes of dislocation bend.

pected during annealing; one is due to the elastic interaction forces between dislocations and the other due to the image force in the vicinity of the surface. Due to the interaction forces, the dislocation loop of half-hexagonal shape before heating changes to that of half-elliptic shape with the increase in annealing temperature, as observed in Figs. 4-4 and 4-5. In these observations, the specimen was annealed for 30 min at each temperature and then a traverse topograph was taken at the same temperature to reveal the change in dislocation configurations; at 1273 K, however, the measurement was attempted on the specimen annealed for 10 min. The displacements of dislocations during exposure were negligible in most cases. Accordingly, the annealing time settled in the annealing experiments is considered to be sufficient to reach the equilibrium configurations of dislocations at each temperature.

It has been shown that from the changes in dislocation configurations, the friction force acting on dislocations can be determined by estimating the interaction forces between dislocations. In Section 4.3.3., the friction force has been estimated as a function of temperature by the two procedures; one is based on the repulsive interaction between parallel dislocations with the same sign (Fig. 4-4) and the other the configurational change of the dislocation bend (Fig. 4-5). Although these measurements have been performed independently, the magnitudes of the friction forces acting on screw dislocations coincide well with each other at each temperature, as shown in Fig. 4-7. The friction forces determined from the repulsive interaction are

expected to be more accurate on the magnitudes of friction force since the procedure is very simple and direct. On the other hand, the differences in friction force between screw and 60°dislocations are known from the measurements based on the configurational changes of dislocation bend. Still, one can recognize that dislocations in silicon crystals are movable under the lower stress than expected in spite of the extremely large Peierls-Nabarro barrier at low temperatures.

### 4.4.2. Analysis of the Temperature Dependence of Friction Force

From Fig. 4-7, it is realized that the observations of dislocation motion in this case have been carried out in much lower stress range, i.e. the order of magnitude $10^{-2}$ MN/m$^2$, than that covered by the conventional measurements of dislocation velocity. The in-situ X-ray topographic observations have suggested that isolated dislocations move under fairly low stress and this movement follows the velocity equation given in Eq. (4.1). Now, Eq. (4.1) is used for analyzing the observed results. It is considered to be reasonable to conduct the analysis here by taking m = 1 since the value of m in Eq. (4.1) is almost equal to a unity for both screw and 60° dislocations. Furthermore, the dislocation density observed in Section 4.3.2. is extremely low, so that one-dislocation approximation can be employed in the following.

Namely, the mean velocity $\bar{v}$ of mobile dislocations is given by

$$\bar{v} = B_o \tau_{eff} \exp(-E / kT) \qquad (4.5)$$

where $\tau_{eff}$ is the effective stress. It is noted that the friction stress estimated in Section 4.3.3. corresponds to this effective stress. The maximum dislocation velocity in this case is considered to be obtained from the segment near the dislocation bend. This velocity was measured in Fig. 4-5 to be $1.8 \times 10^{-6}$ cm/s in average and almost constant at any temperature examined, but it decreased with annealing time as the dislocation segment approached its equilibrium position. Whereas, the velocity of the segment far from the bend would be much lower than that of the segment near the bend and may be approximately the same at each temperature.

Accordingly, it is natural to consider that as for the segment near the point where the dislocation displacement is ended, the mean velocity $\bar{v}$ is constant at each annealing temperature and the following relation is derived from Eq. (4.5).

$$\ln \tau = (E / kT) + C_o \qquad (4.6)$$

$$C_o = \ln \bar{v} - \ln B_o$$

where $\tau$ is the friction stress given in Fig. 4-7. It can be found from this relation that the temperature dependence of the friction force yields the activation energy E for dislocation motion. The activation energy is the slope of the curve shown in Fig. 4-7, which gives 2.4 eV for screw dislocation and 2.2 eV for 60° dislocation. It should be noticed that these values of activation energy have been evaluated from the analysis in the

extremely low stress range where the dislocation-velocity measurements are almost impossible. Nevertheless, they are in good agreement with the activation energies determined in the velocity measurements by in-situ X-ray topography [7,8].

## REFERENCES


[1] H. Alexander and P. Haasen: Solid State Phys. 22 (1968) 27.

[2] V.C. Kannan and J. Washburn: J. Appl. Phys. 41 (1970) 3589.

[3] V.N. Erofeev and V.I. Nikitenko: Sov. Phys. -JETP 33 (1971) 963.

[4] A. George, C. Escaravage, G. Champier and W. Schröter: Phys. Status Solidi (b) 53 (1972) 483.

[5] A. Fisher: Exp. Tech. Phys. 23 (1975) 617.

[6] S.B. Kulkarni and W.S. Williams: J. Appl. Phys. 47 (1976) 4318.

[7] K. Sumino, H. Harada and I. Yonenaga: Jpn. J. Appl. Phys. 19 (1980) L49.

[8] K. Sumino: Semiconductor Silicon 1981 (Electrochem. Soc., Pennington, 1981) p. 208.

[9] S. Schäfer: Phys. Status Solidi 19 (1967) 197.

[10] H. Schaumburg: Philos. Mag. 25 (1972) 1427.

[11] H.-J. Möller: Acta Metall. 27 (1979) 1355.

[12] Y. Nishino, M. Suzuki, T. Tono, H. Saka and T. Imura: Jpn. J. Appl. Phys. 20 (1981) 1533.

[13] K. Sumino and H. Harada: Philos. Mag. A44 (1981) 1319.

[14] J.P. Hirth and J. Lothe: Theory of Dislocations (MacGrow-Hill, New York, 1968) p. 126.

[15] J. Lothe: Philos. Mag. 15 (1967) 353.

# CHAPTER 5

# GENERATION PROCESS OF DISLOCATIONS AT OXIDE PRECIPITATES

## 5.1. INTRODUCTION

It is well recognized in Czochralski silicon crystals that the magnitudes of the upper yield stress and of the yield drop are reduced by heat treatment at temperatures around 1273 K [1-3]. Such a characteristic of the deformation behaviour is supposed to arise from the precipitation of supersaturated oxygen atoms in Czochralski crystals during heat treatment because various types of lattice defects are introduced in connection with this precipitation [4]. These precipitates are determined as silicon oxide by various kinds of analytical techniques [4,5]. It is generally known that an extremely large shear stress can be concentrated at the interface between a large precipitate and the matrix crystal to nucleate dislocations during cooling after heat treatment [6,7]. In practice, dislocation loops are generated under internal stress around precipitates during heat treatment by the mechanism of prismatic punching [4,8-11]. In this case, when the concentration of dissolved oxygen atoms

in the matrix is reduced by the precipitation, the crystal becomes soft because of the increase of dislocation nucleation and of the reduced dislocation locking effect by oxygen atoms [12]. It has been also suggested from a theoretical analysis of the yield behaviour that dislocations punched out from the precipitates are the most important dislocation sources responsible for the precipitation softening [3]. Such being the case, the lowering of the yield stress observed in the macroscopic deformation is possibly due to the increased generation and multiplication of dislocations at oxide precipitates. It should be ascertained, therefore, what dislocation processes actually take place in heat-treated crystals, through which the macroscopic deformation behaviour can be strikingly affected.

In order to clarify the role of oxide precipitates for the deformation behaviour of heat-treated crystals, it is essential to observe dynamically the generation and multiplication processes of dislocations at large oxide precipitates during high-temperature deformation. In the experimental study described in this chapter, the deformation behaviour of precipitate-containing silicon crystals is investigated by means of real-time X-ray topographic observations. The roles of oxide precipitates of various sizes are also discussed in relation to the macroscopic deformation behaviour.

## 5.2. EXPERIMENTAL PROCEDURES

Specimens were prepared from dislocation-free silicon crystals (p-type, 4.3 ohm·cm) grown by the Czochralski technique with a growth direction along [100]. The concentration of oxygen atoms was about $1.5 \times 10^{18}$ $cm^{-3}$ and that of carbon atoms was about $5.0 \times 10^{16}$ $cm^{-3}$, according to the infra-red absorption measurements. In order to introduce thermally-induced microdefects such as oxide precipitates, specimens with (111) surface were at first subjected to an isothermal annealing at 1073 K, 1273 K and 1473 K, respectively, for 20 - 60 h in nitrogen ambient and then cooled slowly.

Shoulder-type tensile specimens were prepared from the same ingots used above by means of wire cutting followed by mechanical and chemical polishing, in the same manner as described in Section 3.2.2.; the tensile axis was parallel to $[1\bar{1}0]$ and the surface orientation parallel to (112), and the gauge dimensions were 15 x 4 x 0.8 $mm^3$. They were also subjected to an isothermal annealing at 1473 K for 50 h in nitrogen ambient and the surface layers of specimens were removed by chemical polishing after the heat treatments.

In-situ deformation experiments were performed with the aid of the high-temperature deformation apparatus [13] described in Section 3.2., being set on a goniometer stage. For the application of the Lang technique, Ag $K\alpha_1$ radiation was used under the operating condition of 50 kV and 1200 mA and symmetric 220 reflection of X-ray was employed for dynamic observation. The dislocation processes were continuously observed on a monitor TV and the video images were recorded in parallel with the observa-

tion by a VTR. To reveal the details of dislocation configurations developed during high-temperature deformation, the specimens were also examined photographically, using Ilford-L4 nuclear research plates.

## 5.3. EXPERIMENTAL RESULTS

### 5.3.1. Oxide Precipitates Produced by Heat Treatment

By means of the heat treatment of Czochralski crystals, large precipitates were observed to be produced at room temperature, the strain field of which could be detected by X-ray topography. Precipitates were easily found since they exhibit a contrast characterized by lobe patterns independent of diffraction condition [14]. Figure 5-1 shows the distribution of precipitates in the specimens which were subjected to the isothermal annealing for 60 h at 1073 K (a), 1273 K (b) and 1473 K (c), respectively. The formation of precipitates was realized at any temperature examined in this experiment. It is seen that the density of oxide precipitates becomes higher for lower annealing temperature and their size becomes larger for higher annealing temperature.

Figure 5-2 shows the density of thermally-induced microdefects as a function of the annealing time. Three specimens were annealed at a different temperature, i.e., 1073 K, 1273 K or 1473 K, and at each temperature annealing was made for 20 h, 40

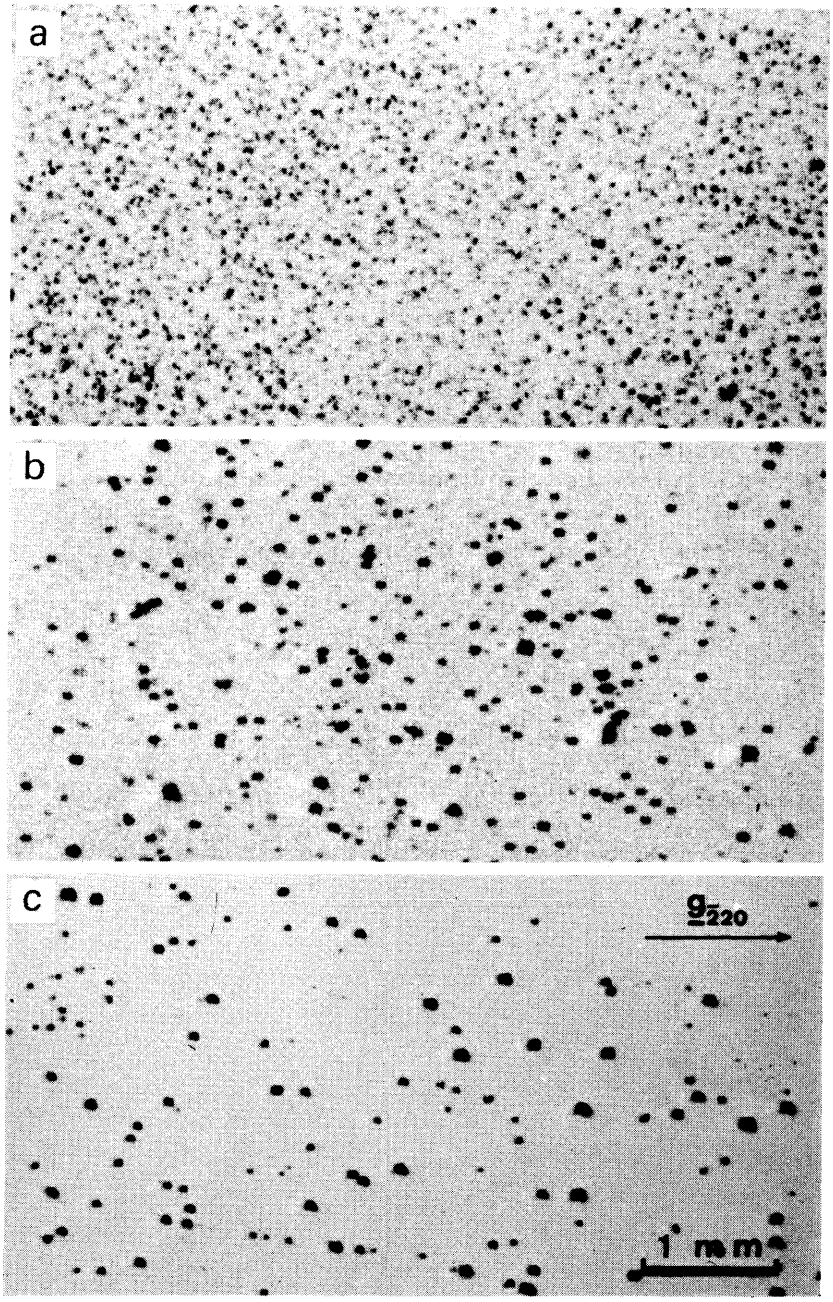


Fig. 5-1. Distribution of microdefects (mostly oxide precipitates) produced by isothermal annealing for 60 h at 1073 K (a), 1273 K (b), 1473 K (c): $\bar{2}20$ reflection.

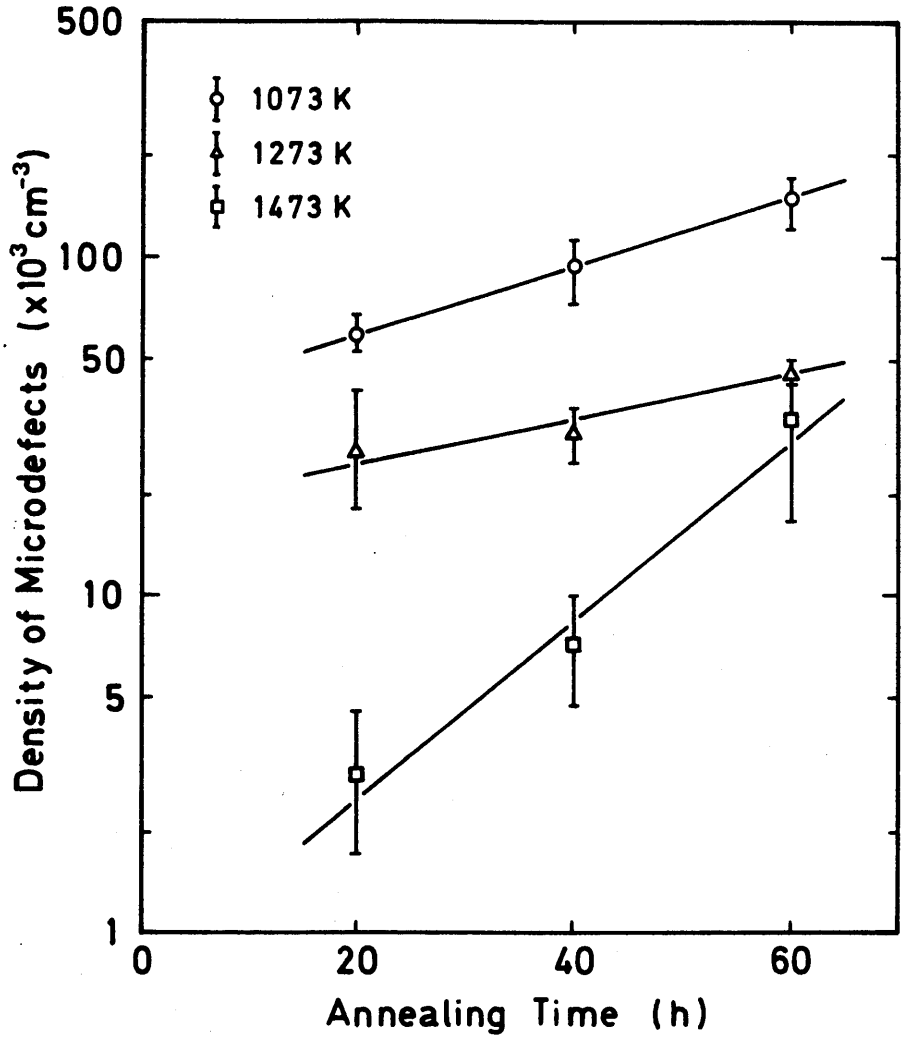


Fig. 5-2. Density of microdefects as a function of annealing time. Three specimens were annealed at a different temperature, i.e., 1073 K, 1273 K and 1473 K, and at each temperature annealing was made for 20 h, 40 h and 60 h.

h and 60 h. Each specimen was then served for observation at room temperature after each annealing treatment. Each circle represents the experimental value averaged over six measurements and the vertical line attached to each circle represents the scatter range of the observed value. Microdefects observed in this case seemed to be mostly oxide precipitates. It is noted that the density of microdefects increases exponentially with annealing time at any temperature examined. This fact is probably due to the growth of each precipitate by prolonged annealing [10], so that the density of microdefects, which could be determined by X-ray topography, increased with the annealing time. It may be said in this connection that a number of extremely fine precipitates which could not be resolved clearly seemed to be nucleated in a striated distribution especially in the earliest stage of precipitation.

From the above observations, it is considered that the crystals annealed at high temperature for long time are suitable for X-ray topographic observation since each precipitate can be identified clearly. For the dynamical observations of dislocation generation at oxide precipitates, therefore, tensile specimens used in this experiment were subjected to the isothermal annealing at 1473 K for 50 h before deformation.

### 5.3.2. Dislocation Generation at Oxide Precipitates

In order to observe the generation of dislocations at oxide precipitates, heat-treated specimens were deformed in tension

along [$\bar{1}$10] direction at 973 K. Figures 5-3 (a) and (b) are the topographs of the specimen containing oxide precipitates before and after the application of stress of 4.9 MN/m$^2$, respectively, and Fig. 5-3 (c) is the enlarged photograph of the area surrounded by the square in Fig. 5-3 (b). Even under the stress significantly lower than the macroscopic yield stress, dislocations were observed to be always generated and propagated at the sites where relatively large precipitates (A, B, C and D) existed before deformation. The generation of dislocations was also observed at other sites of the specimen (for example, E and F) where fine precipitates existed. It is seen from Fig. 5-3 (c) that these dislocations usually belong to one of the slip systems with the maximum Schmid factor. Dislocation half loops originated at the large precipitate (B) were propagated on some slip planes but those originated at the small one (E) on only one slip plane. The projected direction of Burgers vector of dislocations originated at the site indicated by E is also shown in Fig. 5-3 (c). A dislocation shear loop on a slip plane intersecting such a precipitate, usually assumed a half hexagonal shape in spite of a roughly circular shape in ductile metals [7]. In such a manner, the plastic flow already proceeded preferentially at oxide precipitates before the propagation of dislocations originated at the specimen-holding positions although dislocations were also generated near the specimen end as seen at the right top corner of Fig. 5-3 (b).

The generation and propagation process of dislocations was observed continuously and recorded with a TV-VTR system during

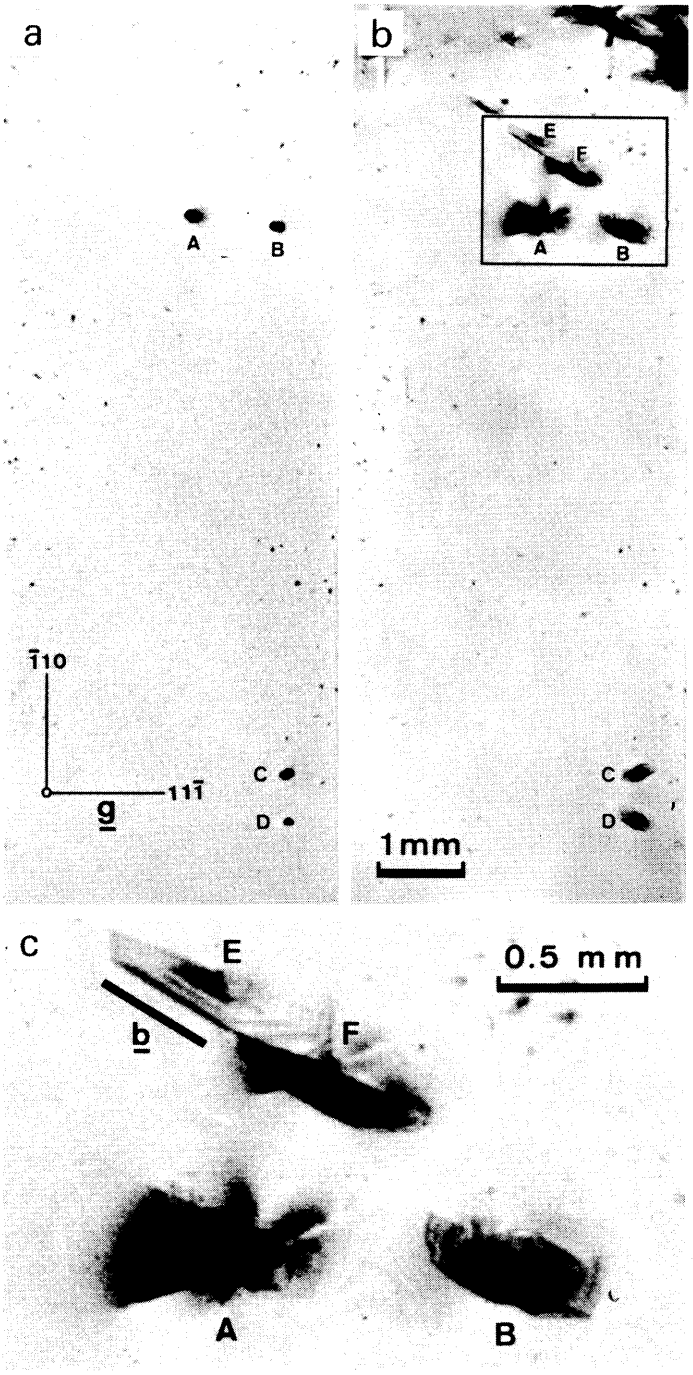


Fig. 5-3. Topographs of the specimen containing oxide precipitates (A - F) before (a) and after (b) the application of stress of 4.9 MN/m$^2$: $11\bar{1}$ reflection. The specimen annealed at 1473 K for 50 h was deformed in tension along [$\bar{1}$10] at 973 K. An enlargement of the area surrounded by the square in (b) is shown in (c).

the deformation. The pictures shown in Fig. 5-4 are synthesized TV images. In parallel with the increase in stress at 1073 K, the sites (A, B and C) where oxide precipitates existed were concentrated in stress (a), and dislocations began to generate and propagate at these sites when the applied stress was increased up to 10.8 $MN/m^2$ (b); the resolved shear stress on the $[0\bar{1}1]/(\bar{1}11)$ shear system is 4.4 $MN/m^2$. The specimen was, thereafter, observed under the constant applied stress and the pictures (b) to (h) were reproduced from a VTR at intervals of about 45 s. The stress required to generate and propagate dislocations seemed to become higher with decreasing precipitate size. Especially from the site indicated by C, a group of dislocation half loops were observed to generate and move slowly and smoothly under the constant stress, the projected direction of the Burgers vector of which is also shown in (c). These dislocations moved on the $(\bar{1}11)$ slip plane with increase in time, assuming a half hexagonal shape with straight arms which are parallel to the <110> direction. Also after that part of dislocation corrsponding to one of the vertexes of a hexagonal loop slipped out of the crystal (e), each segment of dislocations moved independently with the same velocities as before and propagated on the slip plane maintaining a rectilinear figure.

Dislocation loops originated at an oxide precipitate always moved in group under stress, and the motion of leading dislocations seemed to be not disturbed by other dislocations. The distance moved by this group of dislocations increased approximately linearly as a function of time under load, as shown in

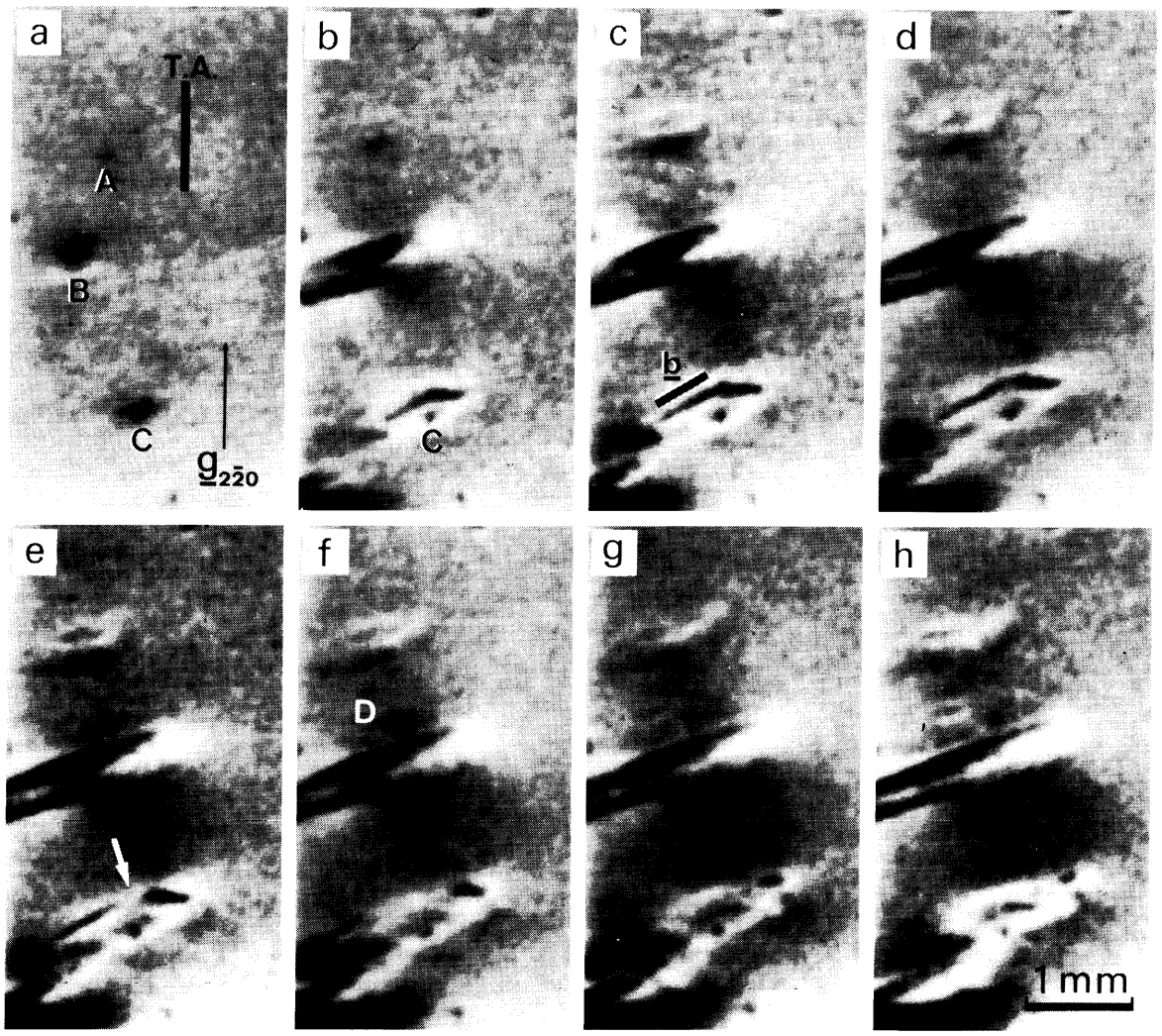


Fig. 5-4. Generation and propagation process of dislocations at oxide precipitates (A - D) under the applied stress of 10.8 $MN/m^2$. The specimen annealed at 1473 K for 50 h was deformed in tension along [1$\bar{1}$0] (T.A.) at 1073 K. Each figure is a synthesized TV image and (b) to (h) at intervals of about 45 s.

Fig. 5-5. This distance is the length of a perpendicular from the precipitate (C in Fig. 5-4) to each dislocation segment and the load time is the duration for which the specimen was held under the resolved shear stress of 4.4 $MN/m^2$ on the $(\bar{1}11)$ slip plane. Both the screw and 60° segments of dislocation moved with the constant velocities and the velocity of dislocations at 1073 K is the slope of the curve, which gives 1.2 x $10^{-4}$ cm/s for 60° dislocation and 9.5 x $10^{-5}$ cm/s for screw dislocation.

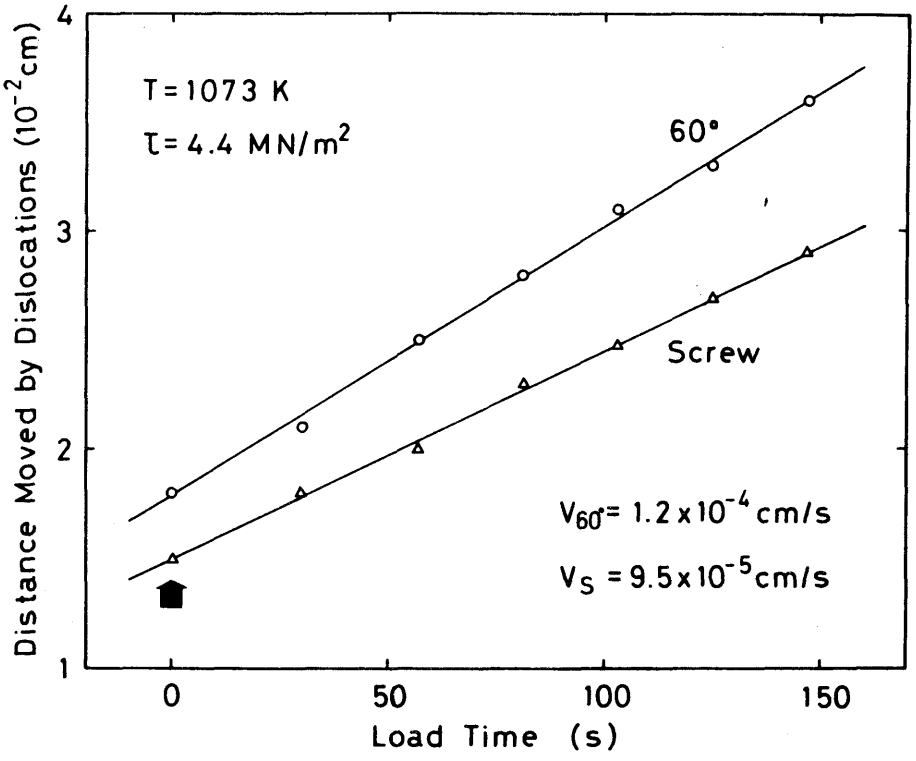


Fig. 5-5. Distance moved by a group of dislocations at 1073 K as a function of time under the resolved shear stress of 4.4 $MN/m^2$ on $(\bar{1}11)$ slip plane. The dislocation velocity is 1.2 x $10^{-4}$ cm/s for 60° dislocation and 9.5 x $10^{-5}$ cm/s for screw dislocation.

In order to reveal the dislocation configuration in the deformed crystal, the topograph was taken at room temperature after removing the stress. Figure 5-6 shows that most dislocations belonged to the slip systems with the maximum Schmid factor, and the points indicated by A, B, C and D in the figure correspond to those in Fig. 5-4. Dislocations originated at the site indicated by A disappeared under this condition of diffraction ($\bar{1}\bar{1}1$ reflection) and only the slip trace was observed as a stripe with black contrast. Even at stress level much lower than the macroscopic yield stress, dislocations were generated at oxide precipitates scattered through the specimen and propagated on the slip planes without the transfer of dislocations from one slip plane onto another in the incipient deformation.

## 5.4. DISCUSSION

From the view point of crystal plasticity, two roles of oxide precipitates are considered in the deformation process; (i) obstacles to the motion of dislocations, (ii) active sites for initiating the plastic flow. It is natural to think that the former is effective in eliminating wafer warpage and the latter is not. On the basis of the observations mentioned in Section 5.3.2., however, the plastic flow always initiated at the large oxide precipitates under stress significantly lower than the macroscopic yield stress. In this case, dislocation sources which bring about precipitation softening may be punched-out

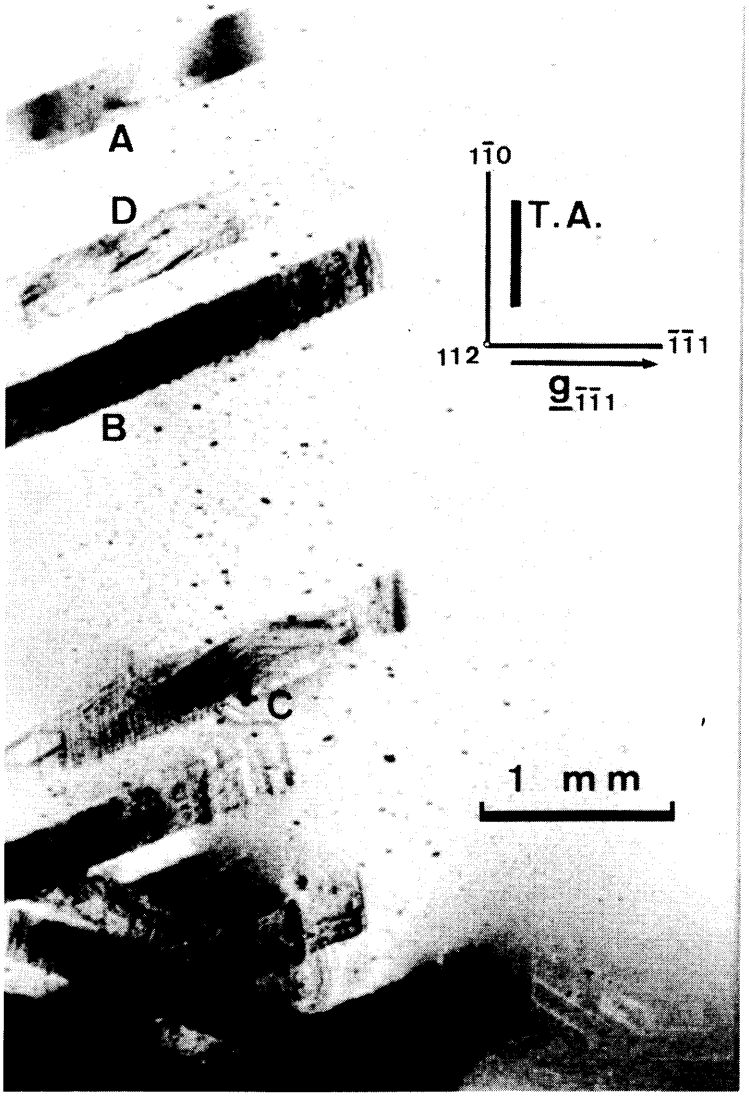


Fig. 5-6. Topograph showing dislocation configuration in the specimen deformed along [1$\bar{1}$0] (T.A.) at 1073 K: $\bar{1}\bar{1}$1 reflection. The point indicated by A - D correspond to those in Fig. 5-4.

dislocations around oxide precipitates, as was suggested from a theoretical analysis of the yield behaviour [3].

It is generally known that silicon crystals show a marked yield drop phenomenon by means of the propagation of Lüders bands [2,15,16] in the macroscopic deformation. Lüders bands usually start from the specimen-holding positions and the strain distribution is very inhomogeneous in the early stage of deformation. It has been also confirmed by weak-beam electron microscopy that no oxide precipitates are revealed in deformed Czochralski crystals which are not subjected to heat treatment [16] (see Fig. 2-7 in Chapter 2). The deformation behaviour, in this case, is not influenced by the precipitation of oxygen atoms. However, the magnitude of the upper yield stress is reduced after annealing Czochralski crystals at temperatures around 1273 K [1-3]. Lüders strain is also absent and slip lines are not discernible, implying that slip is occurring on an extremely fine scale [2]. The observations mentioned in Section 3.2. seem to support these facts exactly. Dislocations have been observed to generate preferentially at oxide precipitates and propagate on the slip planes by loading slightly. The stress to cause the local plastic flow seems to become higher with decreasing precipitate size. That is why more dislocations are punched out to release the increased misfit strain associated with the precipitation as the precipitates grow in size. It is therefore envisaged that the plastic flow would be increasingly caused even around small precipitates in company with the increase in the applied stress. In view of the fact that vast amounts of oxide precipitates are distributed

at random in heat-treated crystals, it is considered that the macroscopic deformation takes place homogeneously all over the specimen.

On the other hand, it is supposed that oxide precipitates produced by the heat treatment may act as obstacles to the motion of dislocations as in precipitation hardening [17]. Such a case was also observed and the pinning points for a dislocation are indicated by the arrows in Fig. 5-7 (a). In this case, since the regions near the specimen-holding positions were concentrated in stress inhomogeneously, dislocations which did not belong to the primary system were generated at the specimen ends and propagated on the slip planes parallel to the tensile axis, as shown in Fig. 5-7. One of these dislocations bulged from the deformed region near the specimen-holding position to the undeformed region and was pinned by oxide precipitates as indicated by the arrows. In such a manner, oxide precipitates scattered around the crystal inherently possess the ability to act as obstacles to dislocation motion. If it is the case, an increase in flow stress would be expected during deformation. However, the lowering of the yield stress has been usually observed in practice in macroscopic deformation. That is explained as follows. As schematically shown in Fig. 5-8, dislocations are generated at many oxide precipitates (open circle) and propagated under stress. Especially, dislocations originated at the large precipitates are propagated on some slip planes which intersect with the precipitates. Dislocations moving on a slip plane may accidentally come across the small precipitate (full circle)

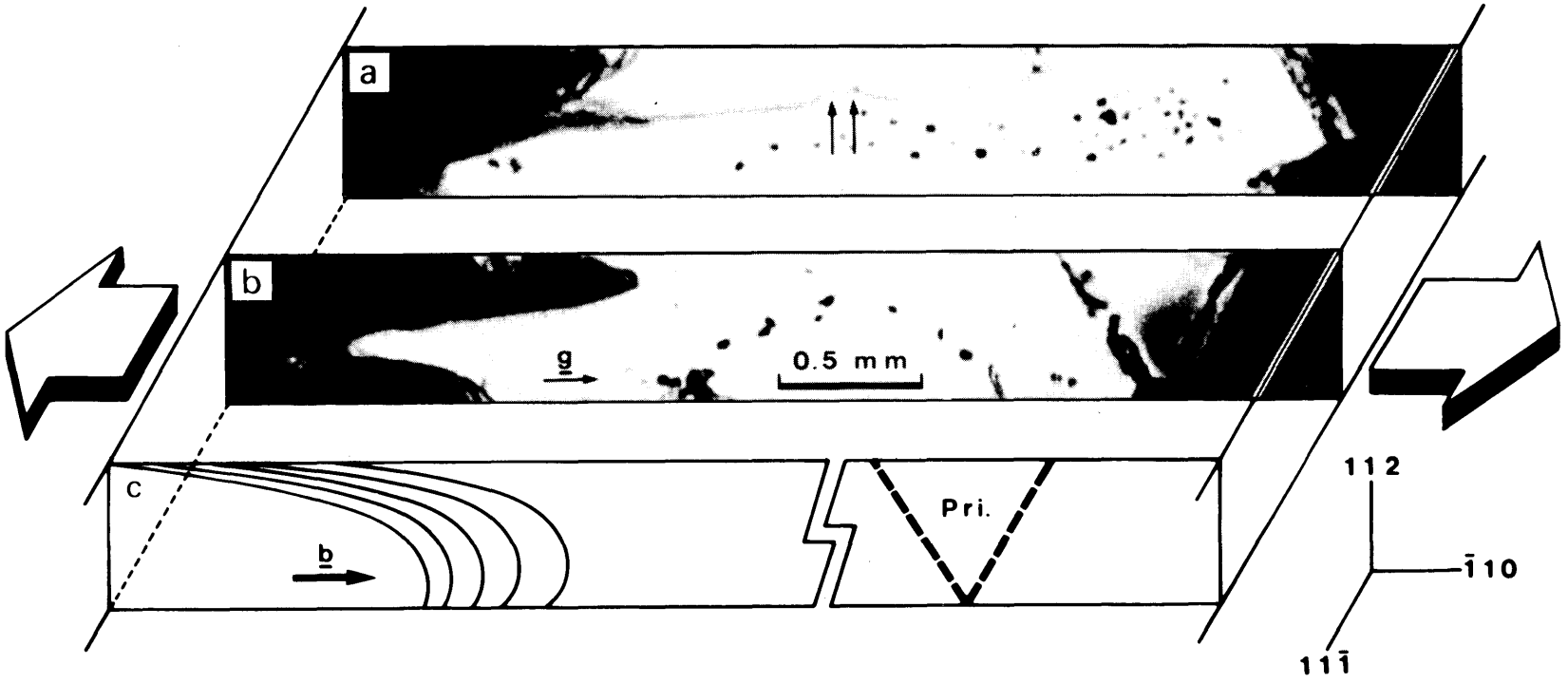


Fig. 5-7. Topographs (a), (b) of cross section of the specimen deformed along $[1\bar{1}0]$ at 1093 K: $\bar{2}20$ reflection and schematic illustration (c) showing dislocation generation on the slip plane parallel to the tensile axis. The pinning points for the dislocation are indicated by the arrows in (a).

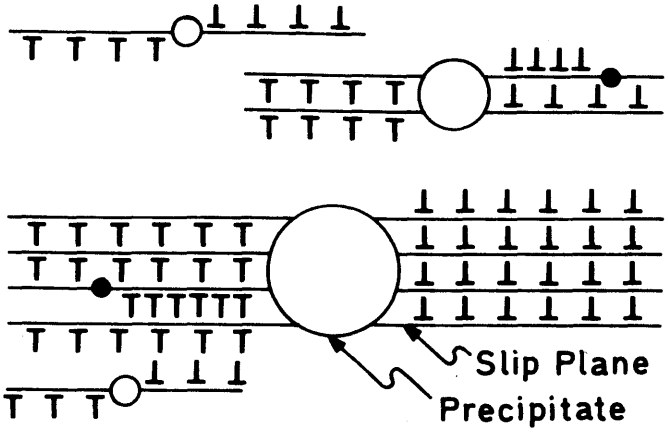


Fig. 5-8. Schematic illustration showing dislocation process in precipitate-containing crystals. Dislocations are generated at large precipitates (open circles) but some dislocations are pinned by small precipitates (full circles).

around which plastic flow has not yet been caused under this applied stress. Although some dislocations are pinned by precipitates in this way and cannot move further, most dislocations on other slip planes still propagate by means of shear stress acting on these slip planes.

Here, which role precipitates play is likely dependent on the size of precipitates [18], in other words, either the precipitates act as active sites for initiating plastic flow or they act as obstacles to dislocation motion. It is generally observed that the generation and propagation of dislocations hardly takes place at relatively small precipitates because a higher stress is required to cause the plastic flow at small precipitates.

In the much higher stress level during ordinary macroscopic deformation, however, it is proposed that plastic flow takes place around most oxide precipitates produced by the heat treatment and the probability of pinning of dislocations is not high enough to cause precipitation hardening. This situation is considered to be reflected in the macroscopic deformation that the heat treatment reduces the magnitudes of the yield stress and of the yield drop.

## REFERENCES


[1] J.R. Patel: Discuss. Faraday Soc. 38 (1964) 201.

[2] S. Mahajan, D. Brasen and P. Haasen: Acta Metall. 27 (1979) 1165.

[3] I. Yonenaga and K. Sumino: Jpn. J. Appl. Phys. 21 (1982) 47.

[4] D.M. Maher, A. Staudinger and J.R. Patel: J. Appl. Phys. 47 (1976) 3813.

[5] W. Kaiser: Phys. Rev. 105 (1957) 1751.

[6] F.R. Nabarro: Theory of Crystal Dislocations (Oxford, London, 1967) p. 708.

[7] M.F. Ashby and L. Johnson: Philos. Mag. 20 (1969) 1009.

[8] T.Y. Tan and W.K. Tice: Philos. Mag. 34 (1976) 615.

[9] K.H. Yang, H.F. Kappert and G.H. Schwuttke: Phys. Status Solidi (a) 50 (1978) 221.

[10] Y. Matsushita, S. Kishino and M. Kanamori: Jpn. J. Appl. Phys. 19 (1980) L101.

[11] F. Shimura, H. Tsuya and T. Kawamura: J. Appl. Phys. 51 (1980) 269.

[12] K. Yasutake, M. Umeno and H. Kawabe: Phys. Status Solidi (a) 69 (1982) 333.

[13] Y. Nishino, M. Suzuki, T. Tono, H. Saka and T. Imura: Jpn. J. Appl. Phys. 20 (1981) 1533.

[14] B.K. Tanner: X-Ray Diffraction Topography (Pergamon, Oxford, 1976) p. 84.

[15] K. Sumino, H. Harada and I. Yonenaga: Jpn. J. Appl. Phys. 19 (1980) L49.

[16] Y. Nishino, H. Saka and T. Imura: Phys. Status Solidi (a) 70 (1982) 729.

[17] V.V. Batavin: Sov. Phys. -Solid State 8 (1967) 2478.; Sov. Phys. -Crystallogr. 15 (1970) 100.

[18] K. Yasutake, M. Umeno and H. Kawabe: Appl. Phys. Lett. 30 (1980) 789.

# CHAPTER 6

# NOTCH EFECT IN INITIATION OF FRACTURE

## 6.1. INTRODUCTION

In the plastic deformation of dislocation-free silicon crystals, dislocations are usually generated at first in stress-concentrated regions near the specimen-holding positions. However, when the crystal contains surface steps and/or oxide precipitates, in particular, at the side surface of the specimen, deformation proceeds by means of the propagation of plastic zones originated from such sites [1]. The development of these plastic zones can be realized only at high temperatures since silicon crystals are extremely brittle at lower temperatures because of the high Peierls-Nabarro barrier [2]. Investigation of the deformation of this type of crystals may provide useful information on the fracture mechanism of metals as well as that of ceramics. From this point of view, Weissmann et al. [3,4] revealed the importance of microplasticity in the fracture of silicon crystals and determined the elastic and plastic strain distribution in deformed crystals. In order to clarify the fracture mechanism, it is also important to investigate the

process of generation and multiplication of dislocations at the beginning of deformation because plastic deformation precedes the propagation of crack [5].

The purpose of the experimental study described in this chapter is to carry out the real-time X-ray topographic observation of the deformation behaviour of notched silicon crystals as a function of applied stress and to discuss the role of dislocation generation in crack propagation.

## 6.2. EXPERIMENTAL PROCEDURES

Shoulder-type tensile specimens were prepared in the same manner as described in Section 3.2.2. from dislocation-free silicon crystals grown by the Czochralski technique; the tensile axis was parallel to [1$\bar{1}$0] and the surface orientation parallel to (112), and the gauge dimensions were 15 x 4 x 0.8 $mm^3$. A U-shaped notch was introduced into the specimen by wire-cutting, and the surface damage caused by cutting was completely removed by mechanical and chemical polishing. In-situ deformation experiments were performed with the aid of the high-temperature deformation apparatus [1] described in Section 3.2., being set on a goniometer stage. The deformation temperature set up in this study was 973 - 1023 K which is a little above the notch-brittle transition temperature of about 920 K [3], and the applied stress was in the range from 1.0 to 25.0 $MN/m^2$ in nominal stress. Symmetric 220 reflection using Ag $K\alpha_1$ radiation

was employed for dynamic observation and the X-ray topographic images observed on a monitor TV were recorded by a VTR. To reveal the details of dislocation configurations in the vicinity of the notch tip, the deformed crystals were also examined by transmission electron microscopy using a high voltage electron microscope (Hitachi, HU-1000D) operated at 1000 kV.

## 6.3. EXPERIMENTAL RESULTS AND DISCUSSION

The propagation of plastic zone originating at the notch tip was observed continuously during tensile deformation. The pictures shown in Fig. 6-1 are synthesized TV images at stress levels of (a) 0, (b) 1.0, (c) 14.7, (d) 20.6, (e) 24.5, (f) 22.5 $MN/m^2$; the deformation was interrupted at stress level (e) and the stress was relaxed at level (f). The crystal was distorted elastically around the notch tip simultaneously with loading (b), and a contrast characterized by lobe patterns appeared, as expected from the theory of the dynamical diffraction of distorted crystals [6]. This elastically-distorted region increased in size with deformation (c), and at a stress level of about 20 $MN/m^2$ dislocations were generated at the notch tip (d). Besides the black area around the notch tip, groomy areas scattered over the specimen surface were also observed in the stress-applied state. These are due to elastic strain associated with the surface roughness caused by chemical polishing. The stress of 20 $MN/m^2$ is the elastic-plastic transition stress

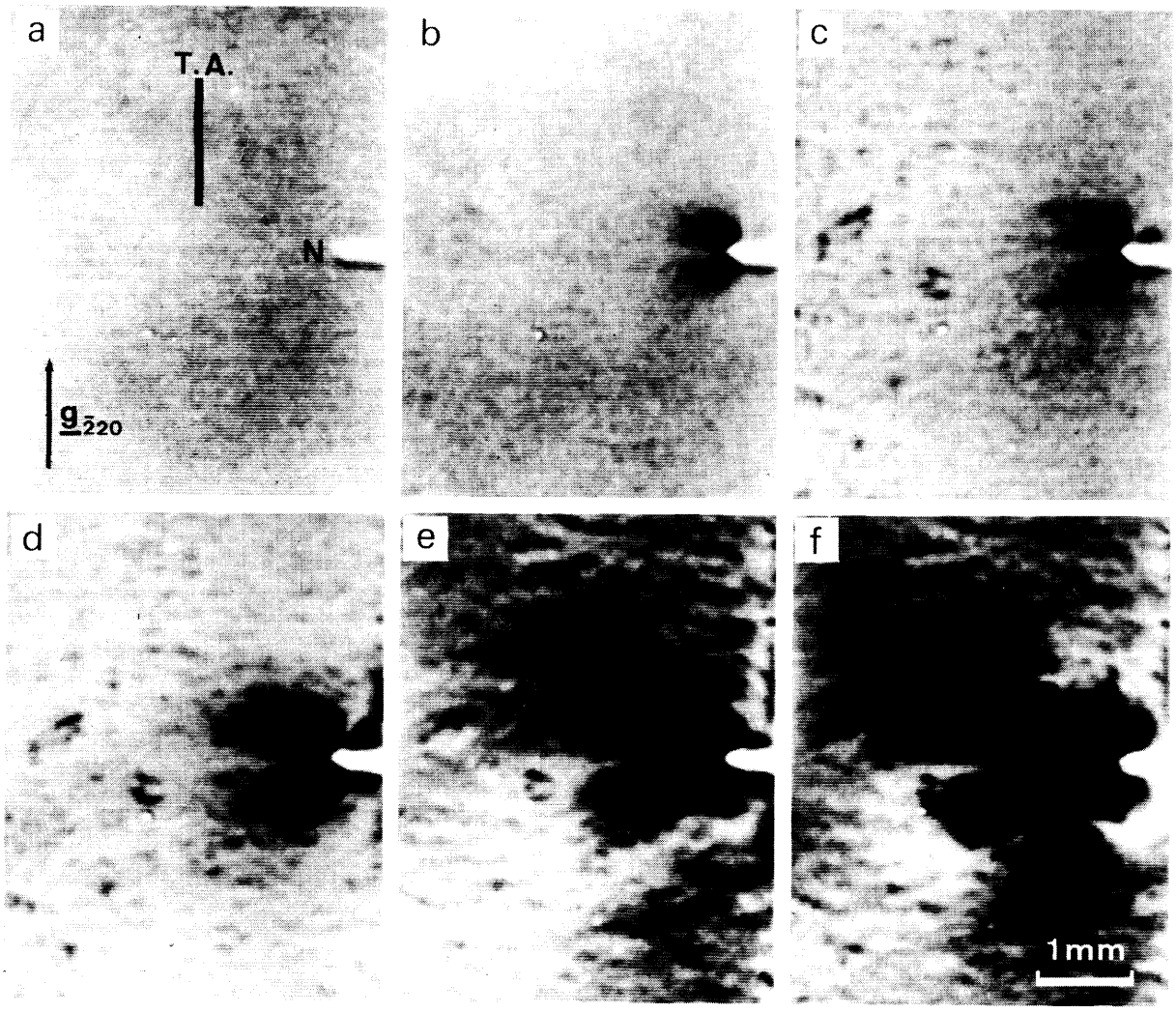


Fig. 6-1. Propagation of plastic zone originating at the notch tip (N). The specimen was deformed along [$\bar{1}$10] at 973 K. Synthesized TV images at stress levels of (a) 0, (b) 1.0, (c) 14.7, (d) 20.6, (e) 24.5, (f) 22.5 MN/m$^2$: $\bar{2}$20 reflection.

determined experimentally at 973 K. Below this transition stress, the strain contrast which appears around the notch during deformation can be eliminated entirely by unloading. Once dislocations were generated, the plastic zone propagated in front of the notch without the increase in the applied stress (f).

The plastic zone and residual elastic strain distribution around the notch could be seen after removing the stress at room temperature. Figures 6-2 (a) to (d) show the strain distribution in the specimen deformed in Fig. 6-1 after removal of 130 μm of the surface layers. They are conventional traverse topographs showing the same area of the specimen, obtained with various reflections indicated in the figures. The size of the elastically distorted region was hardly changed by the change in the specimen thickness. These topographs, however, become very different for different reflection vectors. Apart from the image detail, it is realized by reversing the reflection vector as shown in Fig. 6-2 (a) and (b) that the image due to the strain around the notch is developed symmetrically about the central axis of the notch, which is perpendicular to the tensile axis. From direct observation by HVEM, it has been suggested that when dislocations generated from the crack tip propagate into the region where the stress concentration is no longer strong, they are stopped and form cell walls by mutual interaction [5]. That is why the region of dislocation generation is restricted to the notch tip and its vicinity. In spite of this, the elastic strain contrast associated with the plastic zone also appears on

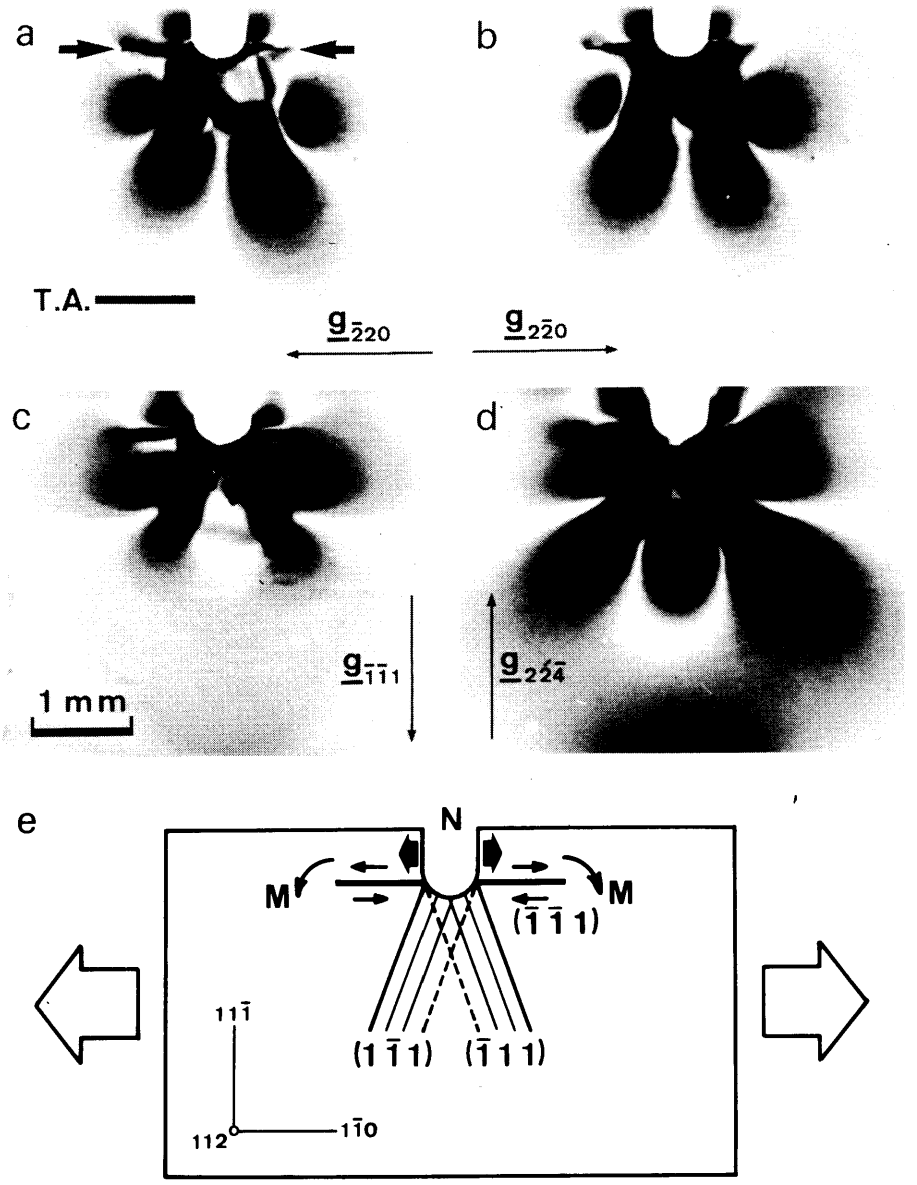


Fig. 6-2. Strain distribution around the notch (N) of the specimen deformed in Fig. 6-1 after removal of surface layers of 130 μm. Conventional traverse topographs obtained with $\bar{2}20$ reflection (a), $2\bar{2}0$ reflection (b), $\bar{1}\bar{1}1$ reflection (c) and $22\bar{4}$ reflection (d). Schematic illustration (e) shows the operation of bending moment (M) and generation of dislocations on the slip plane parallel to the tensile axis (T.A.).

the other edge of the specimen, away from the notch, as seen in Fig. 6-2 (d). It can be said that there is a long-range strain field due to the constraining influence of the plastic zone. On the other hand, as shown by the arrows in Fig. 6-2 (a), dislocations are observed to generate on the slip planes parallel to the tensile axis although these dislocations belong to a slip system whose Schmid factor is zero. It is considered as shown schematically in Fig. 6-2 (e) that the bending moment, indicated by M, about the axis perpendicular to the specimen surface operates at the notch tip as a consequence of the activity of two slip systems with the maximum Schmid factor. Even if the Schmid factor is zero, therefore, the dislocations can be generated on these slip planes through shearing caused by the operation of the bending moment at the notch tip. Consequently, it is thought that the resultant bending moment acts as if it cleaved the specimen, as indicated by the heavy arrows.

The development of plastic deformation from the notch was not always observed in company with tensile deformation. In the same manner as the deformation behaviour of unnotched specimen, dislocations were often generated and multiplied at the specimen ends near the specimen-holding positions already at the stress level below the elastic-plastic transition stress because of the complicated stress concentration. Moreover, in specimens containing preferred sites for dislocation generation at or near the surface, these sites became activated during deformation. The notch sensitivity is, in this case, lowered because the generation and multiplication of dislocations proceeds increasingly

with deformation at preferred sites other than the notch. An example of such a case is shown in Fig. 6-3, which shows synthesized TV images at stress levels of (a) 0, (b) 2.9, (c) 5.9, (d) 8.8, (e) 11.8 $MN/m^2$ and (f) was observed after unloading. The site indicated by A in (b) was activated in company with loading and this plastic zone propagated into the undeformed region of the specimen in proportion to the increase in the stress. A contrast characterized by lobe patterns also appeared at the notch tip (b) and increased in size with loading (c). The elastically distorted region around the notch, however, decreased in size with the advance of the plastic zone originating from the side surface opposite to that containing the notch; the notch sensitivity was lowered because of the reduction of the effect of stress concentration. The observation after unloading (f) confirmed that neither elastically nor plastically distorted region was formed around the notch.

On the other hand, the deformation behaviour of the specimen containing a mechanically damaged notch exhibited a striking contrast to that of the specimen containing a strain-free notch. This is because a damaged notch is considered to contain a vast number of surface steps with strain. Figures 6-4 (a) to (d) are synthesized TV images showing the deformation process associated with the damaged notch. First, the specimen was subjected to 1.0 $MN/m^2$ at 1023 K and observed after the removal of surface damage (a). It was subsequently held under 2.9 $MN/m^2$ at 1023 K (b), and for 10 min under the same stress (c), for 20 min (d). Simultaneously with loading, dislocations were generated at the

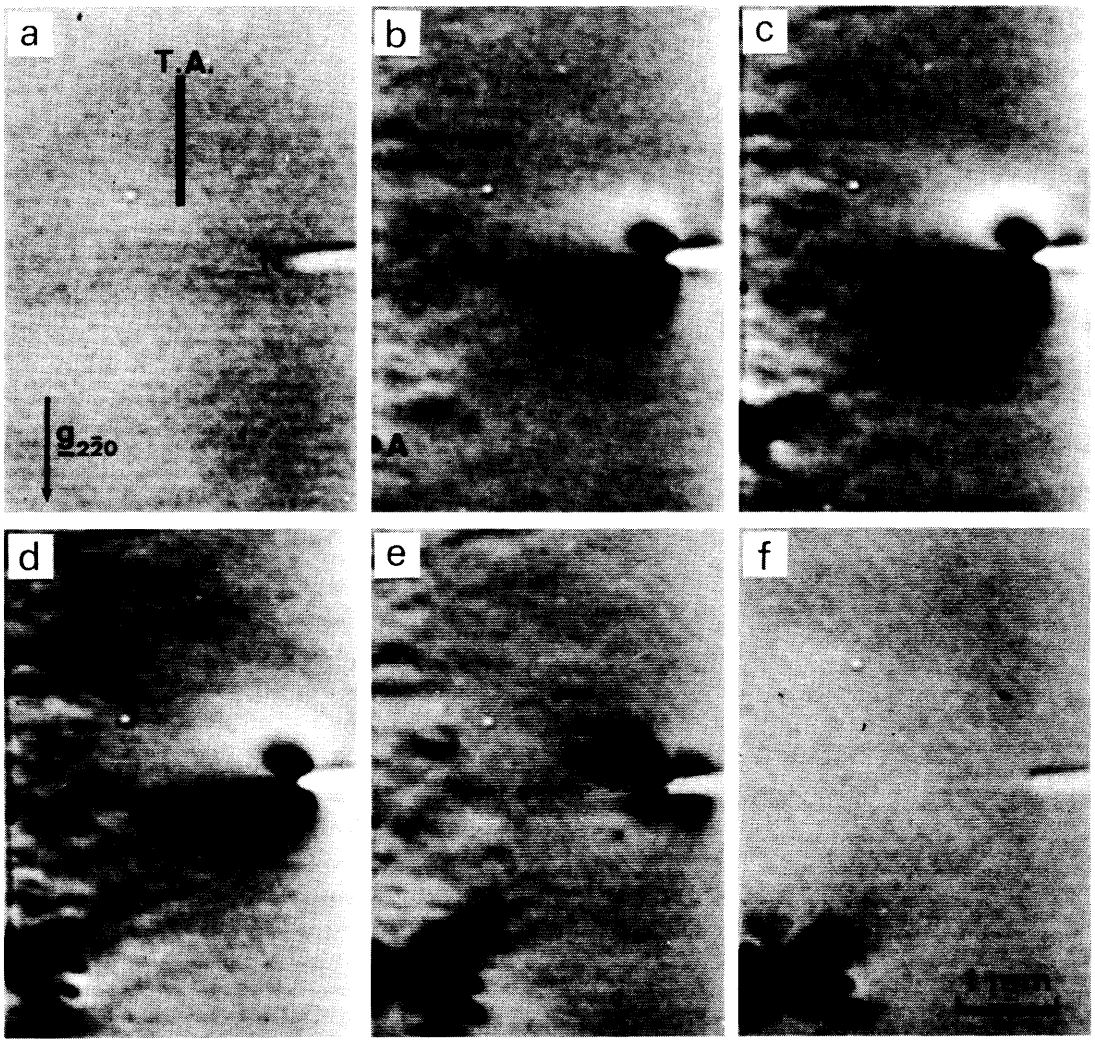


Fig. 6-3. Propagation of plastic zone originating at the strain center (A). The specimen was deformed along [$\bar{1}$10] at 973 K, but the notch tip (N) was not deformed plastically. Synthesized TV images at stress levels of (a) 0, (b) 2.9, (c) 5.9, (d) 8.8, (e) 11.8 $MN/m^2$ and (f) was observed after unloading: 2$\bar{2}$0 reflection.

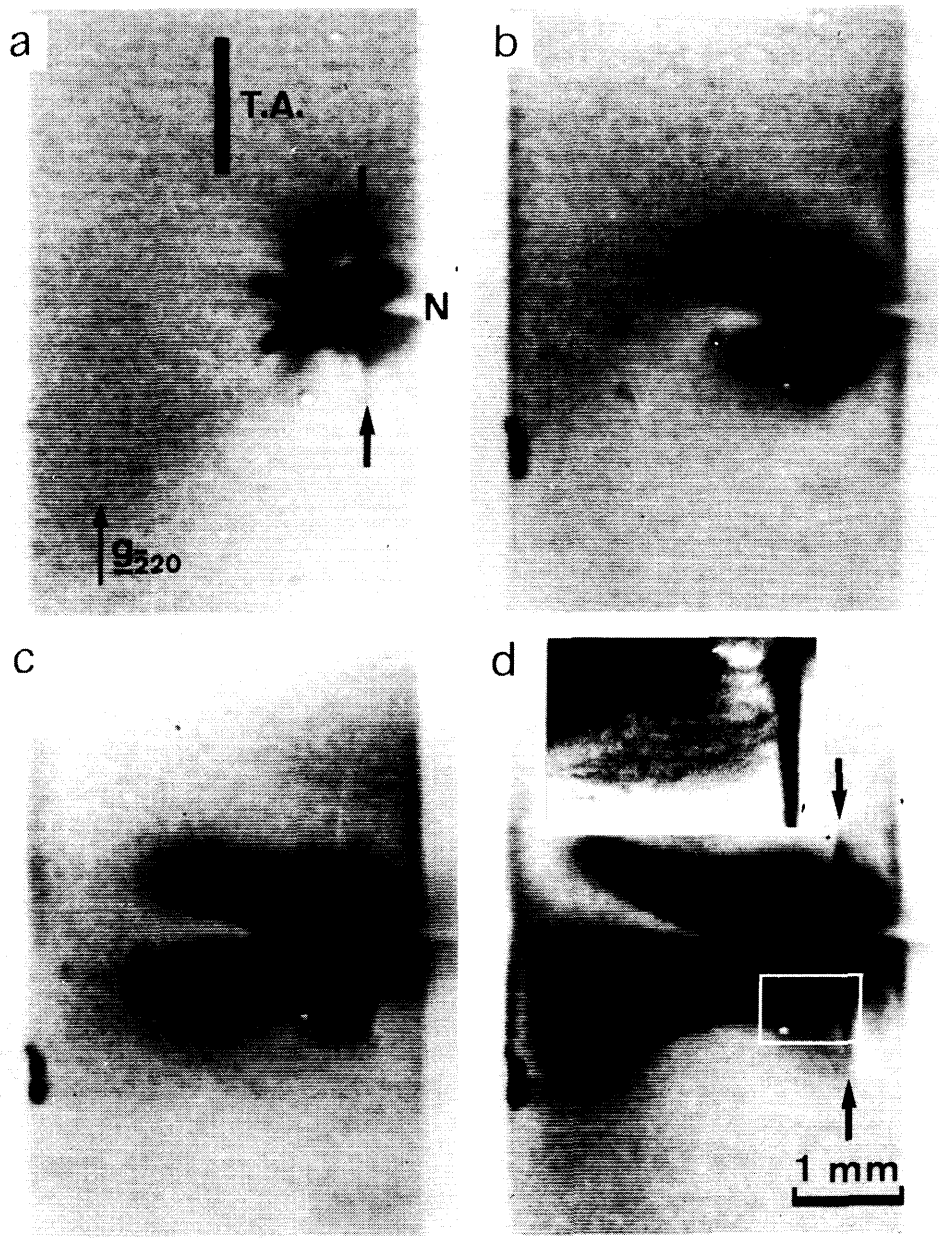


Fig. 6-4. Deformation behaviour of the specimen containing the mechanically damaged notch (N). The specimen was held along [$\bar{1}$10] at 1023 K under 1.0 MN/m$^2$ (a) and under 2.9 MN/m$^2$ (b) to (d). Each figure is a synthesized TV image and (b) to (d) at intervals of 10 min: $\bar{2}$20 reflection. At the top of (d), an enlargement of the area surrounded by the square which was taken after unloading is illustrated.

damaged notch tip by means of the activation of multiple slip systems (a). The generation and multiplication of dislocations was, thereafter, to take place easily over the extensive area across the specimen by loading slightly (c). Dislocations were also observed to generate and move on the slip planes parallel to the tensile axis as indicated by the arrows. It was found after unloading that the area assuming black contrast ahead of the notch was, for the most part, deformed plastically and many dislocations were observed to generate as shown at the top of Fig. 6-4 (d) by enlarging the area surrounded by the square. The details of dislocation configuration in the vicinity of the notch tip were revealed by transmission electron microscopy after the deformation shown in Fig. 6-4. The dislocation configuration was very similar to that of the crystal deformed to the lower yield point [7] (see Fig. 2-6 in Chapter 2), as shown in Fig. 6-5. There are two activated slip planes, $(\bar{1}11)$ and $(1\bar{1}1)$, in this orientation of the specimen. Long curved primary dislocations (about ten microns in length) were more predominant and the dipole and/or multipole configuration was also revealed. Dislocations with two different Burgers vectors are usually present; $[0\bar{1}1]$ and $[\bar{1}0\bar{1}]$, and the dislocation density is, in this case, about $6.7 \times 10^6$ $cm^{-2}$. As seen along the dotted lines in the figure, dislocations were observed with sharp changes of their directions as a result of the formation of Lomer dislocations. They are thought to be produced by the intersection of dislocations gliding on the $(11\bar{1})$ slip planes parallel to the tensile axis since these dislocation interactions can be expected

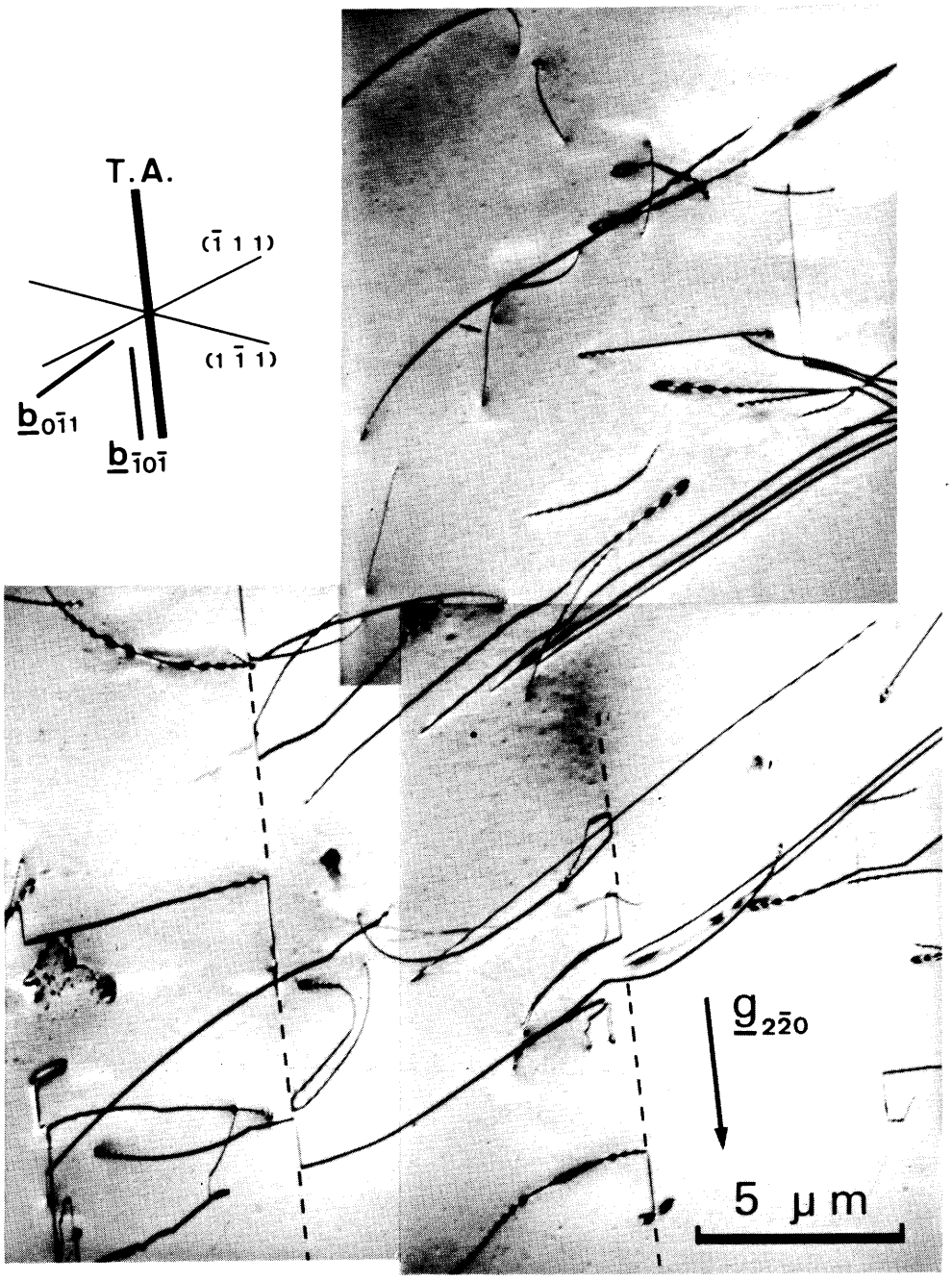


Fig. 6-5. Electron micrograph showing dislocation configuration in the vicinity of notch tip of the deformed specimen in Fig. 6-4: $2\bar{2}0$ reflection. Two different projected Burgers vectors ($\underline{b}$) are also shown: $[0\bar{1}1]$ and $[\bar{1}0\bar{1}]$.

to occur in the vicinity of the notch.

From the above observations, it is considered that the crack propagation is induced by the release of excess strain energy accumulated as a long-range elastic strain accompanied by entangled dislocations in the plastic zone near the notch tip. In this case, unless other preferred sites for dislocation generation become activated during deformation, the operation of the bending moment at the notch tip seems to play, as expected, an important role as the driving force of crack propagation.

## REFERENCES


[1] Y. Nishino, M. Suzuki, T. Tono, H. Saka and T. Imura : Jpn. J. Appl. Phys. 20 (1981) 1533.

[2] H. Alexander and P. Haasen: Solid State Phys. 22 (1968) 27.

[3] Y. Tsunekawa and S. Weissmann: Metall. Trans. 5 (1974) 1585.

[4] S. Weissmann and T. Saka: Advance in X-Ray Analysis, eds. H.F. McMurdie, C.S. Barrett, J.B. Newkirk and C.O. Ruud (Plenum, New York, 1977) Vol. 20, p. 237.

[5] H. Saka and T. Imura: Jpn. J. Appl. Phys. 9 (1970) 1185.

[6] Y. Ando and N. Kato: J. Appl. Crystallogr. 3 (1970) 74.

[7] Y. Nishino, H. Saka and T. Imura: Phys. Status Solidi (a) 70 (1982) 729.

# CHAPTER 7

# CYCLIC DEFORMATION AND DISLOCATION CONFIGURATIONS

## 7.1. INTRODUCTION

It is known that silicon crystals behave like metals during tensile deformation at elevated temperatures, exhibiting stress-strain curve consisting of three deformation stages, which are analogous to that of f.c.c. metals [1-3]. In addition, the present investigation has revealed by the electron microscope observations that the dislocation configurations at various deformation stages in silicon crystals are very similar to those of copper single crystals [3] (see Chapter 2). Such being the case, it may be expected that there is a close resemblance in the work-hardening process between silicon crystals and f.c.c. metals in spite of the extreme difference in Peierls-Nabarro barriers.

In contrast to a unidirectional deformation such as tension or compression, the cyclic deformation behaviour of semiconductor crystals has not yet been thoroughly investigated. One exception is the cyclic deformation carried out by reversed cantilever bending [4], which has found that increased cycling of

germanium crystals results in the formation of a regular cell structure which finally consumes the bundled dislocation structure. The difficulties in carrying out the push-pull type cyclic deformation of semiconductor crystals like germanium and silicon are considered to arise from the rigid grip system for push-pull since silicon crystals are extremely brittle. Nevertheless, it is hoped that the fundamental research on cyclic deformation of silicon crystals will provide some significant information on the fatigue hardening process which should be characteristic of highly perfect crystals with large Peierls-Nabarro barriers.

Now, real-time X-ray topography [5-9] has shown that dislocations in silicon crystals move and multiply at elevated temperatures under stresses which are much lower than the yield stress. Accordingly, there is a possibility that the multiplication of dislocations takes place during cyclic deformation even within the macroscopic elastic limit in stress-strain curve and that the dislocation configurations characteristic of fatigue cycling may be established in advanced stage of cyclic deformation.

In the experimental study described in this chapter, the stress-strain characteristics in cyclic deformation of silicon crystals are at first investigated by using a high-temperature fatigue apparatus which has been newly constructed for the present fatigue experiments. In order to verify whether or not the fatigue hardening takes place during cyclic deformation in the elastic region, silicon crystals have been stressed cyclically

in tension and in compression at the stress level within the macroscopic elastic limit. Observations of microstructures are made intensively on the early stages of fatigue hardening to identify dislocation processes characteristic of fatigue cycling. In order to clarify the differences and also the similarities in dislocation configuration between tensile deformation and cyclic deformation, the obtained results have been compared with those observed during tensile deformation.

## 7.2. EXPERIMENTAL PROCEDURES

### 7.2.1. High-Temperature Fatigue Tests

#### Specimens for Fatigue Test

Specimens were prepared from silicon crystals (n-type, 100 - 500 ohm·cm) grown by the floating-zone technique. The density of grown-in dislocations was determined by etch pit as about $2 \times 10^4$ $cm^{-2}$. Specimens of desired geometry and shape suitable for fatigue test were prepared by means of ultrasonic cutting, as illustrated in Fig. 7-1. The sizes were about $4 \times 4$ $mm^2$ in cross section and 8 mm in gauge length. The deformation axis and the side surface were parallel to $[\bar{1}23]$ and $(1\bar{1}1)$, respectively. They were mechanically polished, followed by chemical polishing.

#### High-Temperature Fatigue Apparatus

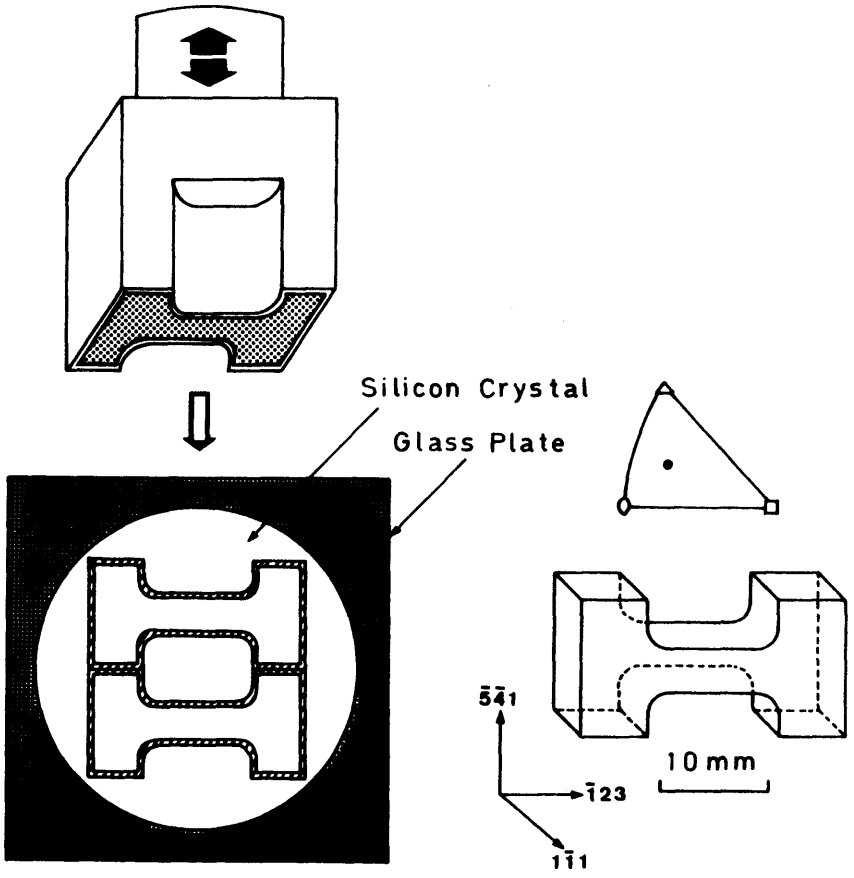


Fig. 7-1. Schematic illustration of the procedure for preparing fatigue specimen having shoulders at the both ends by means of ultrasonic cutting. Geometry and shape of specimen are also shown; tensile axis parallel to $[\bar{1}23]$ and side surface parallel to $(1\bar{1}1)$.

High-temperature fatigue tests were carried out by using the newly developed high-temperature fatigue apparatus, as shown schematically in Fig. 7-2, which was attached to an Instron-type testing machine (Shimadzu, DSS-2000 Autograph).

The pull rods inside the vacuum chamber are separated to two parts; the outer rod is cylindrical and the inner rod is of piston-type, both made of heat-resistant alloys (M-200). After setting a specimen to the grips, the positions of the grips are adjusted by moving the crosshead. Then the shoulder parts of the specimen are gripped tightly at a desired elevated temperature by squeezing compressed gas so as to push the inner rods. After that, the inner rods are tightened through the clamps. The above procedures are performed so as not to put any load to the specimen. During tensile cycles, the specimen is held against pulling by the grips which are the ends of the outer pull rods. The specimen is loaded through the inner pull rod during compressive cycles. The extensions can be measured and controlled by a linear-variable-differential (LVD) transformer extensometer which is connected to the flexible bellows of the apparatus.

The water-cooled specimen chamber is either evacuated to about $5 \times 10^{-3}$ Pa or filled with a desired inert-gas atmosphere. The heaters are made of molybdenum plates which are cut in a meander shape. Temperature of the specimen is measured with an alumel-chromel thermocouple positioned near the specimen and kept constant with accuracy of $\pm$ 1 K by a P.I.D. temperature regurator. The maximum specimen temperature attained is about

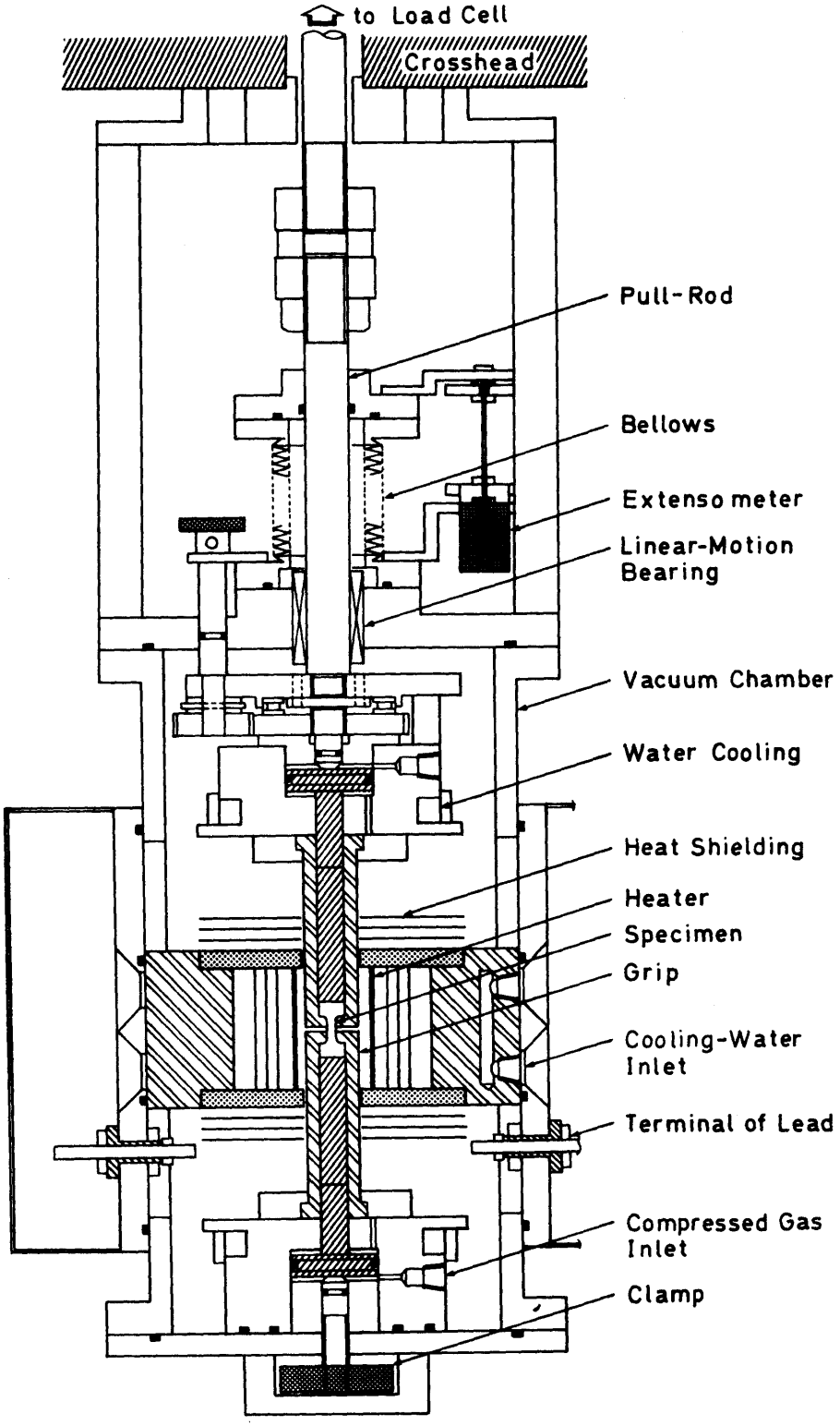


Fig. 7-2. Schematic illustration of high-temperature fatigue apparatus for Instron-type testing machine.

1273 K.

Fatigue Tests

By using the aforementioned apparatus, fatigue tests can be performed in push-pull in a rigid grip system. All tests were conducted in vacuum at 1073 K and at a shear-strain rate between $8.9 \times 10^{-5}$ $s^{-1}$ and $8.9 \times 10^{-4}$ $s^{-1}$. Upon termination of the test, specimens were cooled rapidly without removing load so as to freeze in the dislocation configurations. Surfaces of the deformed crystals were examined by Nomarsky contrast technique using an optical microscope, and slip-band distributions were observed on the $(\bar{5}\bar{4}1)$ free surfaces of the specimens.

7.2.2. Electron Microscope Observations

Electron microscope observations were made on the specimens cyclically loaded at a constant stress amplitude of $\pm$ 16 $MN/m^2$ (: resolved shear stress) for 330 and 1000 cycles at 1073 K. Slices for electron microscope observations of about 0.4 mm thick were obtained from the central parts of the gauge length of the deformed specimens using a multi-wire saw. The procedures for thinning these slices were the same as those described in Section 2.2.2. Dislocation configurations in each specimen were observed by an HVEM being operated at an accelating voltage of 1000 kV. The dislocation densities were measured on the photograph by counting dislocation intersections with a series of random circles [10].

## 7.3. EXPERIMENTAL RESULTS

### 7.3.1. Cyclic Deformation Characteristics

The specimens were stressed cyclically in tension and in compression at 1073 K at the shear-strain rate of $8.9 \times 10^{-5}\ s^{-1}$. Figure 7-3 shows the stress-strain curves, in which the loading direction was changed five times; in all cases, the initial loading was in the tensile direction. The plastic shear strain imposed in each cycle was estimated to be about 5 %. It is found that the magnitudes of stress drop after the upper yield point decreased drastically as the loading direction was reversed in the course of deformation and that the yield drop desappeared completely after the second tension-compression cycling. The slope of the curve after yielding, i.e., the work-hardening rate $\theta$, is always constant in the respective loading direction during the course of deformation. The values of $\theta/\mu$ ($\mu$: shear modulus) is $5.6 \times 10^{-4}$ for tensile cycle and $6.6 \times 10^{-4}$ for compressive cycle.

Both the yield stress and the final muximum stress in each cycle are plotted in Fig. 7-4 as a function of the cumulative shear strain; they tentatively correspond to cyclic hardening curve. After hardening rapidly in the small strain region, both the yield stress and the maximum stress in tensile cycle increase linearly with the increase in cumulative strain. Although the yield stress and the muximum stress also increase linearly in compressive cycle, there is a gap in stress between them

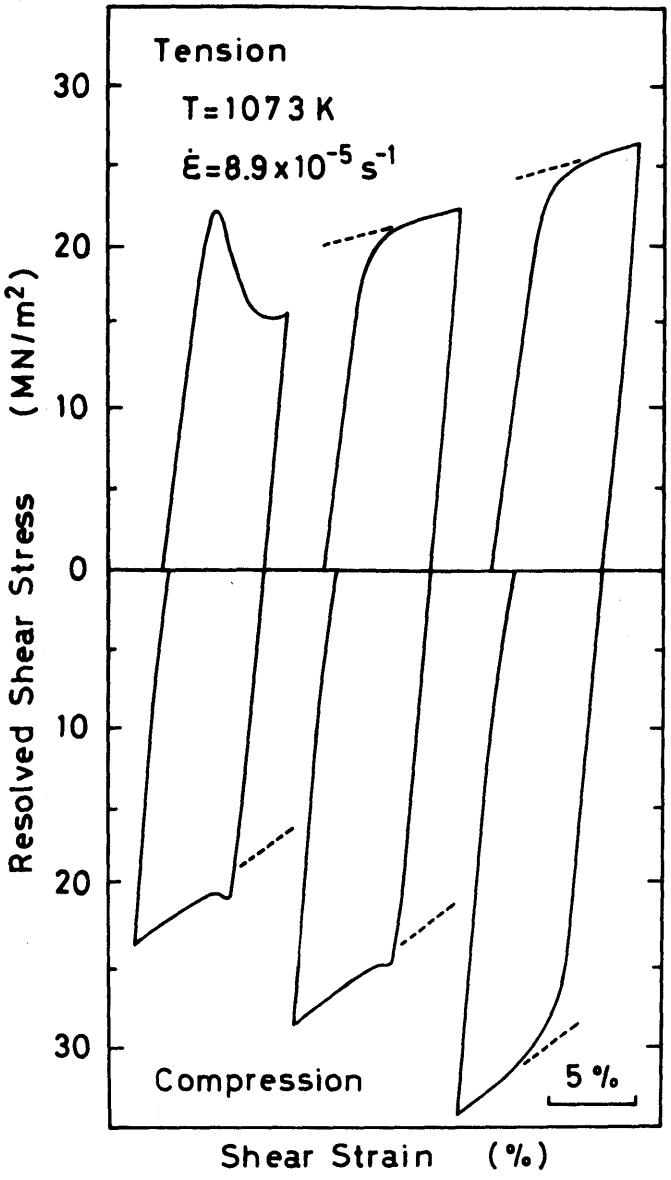


Fig. 7-3. Stress-strain curves at 1073 K at the strain-rate of 8.9 x $10^{-5}$ $s^{-1}$ in which the loading direction was changed five times; the initial loading was in the tensile direction. The plastic shear strain imposed in each cycle is about 5 %.

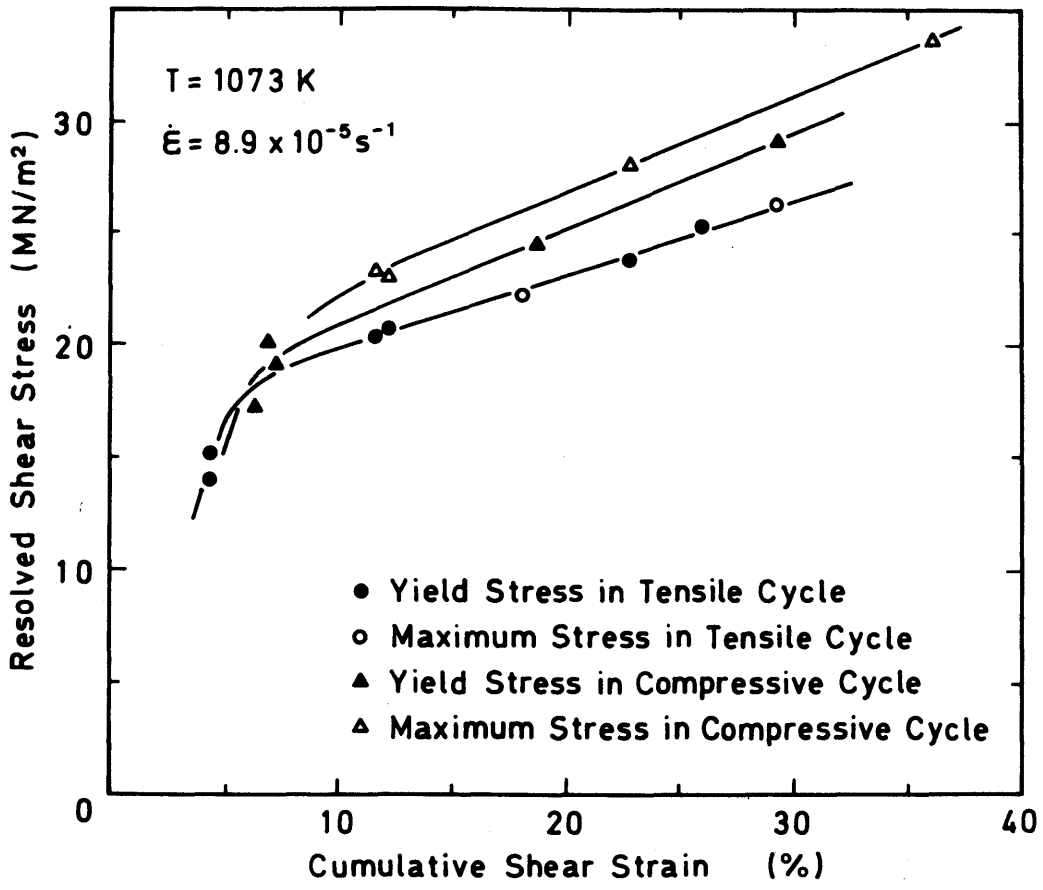


Fig. 7-4. Yield stress and final maximum stress in each cyclic deformation at 1073 K at the strain rate of $8.9 \times 10^{-5}$ $s^{-1}$ expressed as a function of cumulative shear strain; they correspond to cyclic hardening curve.

when compared at the same cumulative strain; this stress gap is about 1.6 $MN/m^2$. Nevertheless, the slope of the both curves in compressive cycle is approximately the same.

Cyclic deformation was also performed in the stress range much lower than the macroscopic yield stress. All specimens were cyclically stressed at the shear-strain rate of $8.9 \times 10^{-4}$ $s^{-1}$ by first imposing a tensile stress 16 $MN/m^2$ (: resolved shear stress) and then an equal compressive stress, which corresponds to a stress level of about one-seventh of the upper yield stress in compressive deformation at 1073 K. Figure 7-5 represents a typical example of cyclic stress - time curve under the condition of constant stress amplitude. In such a way, the spec-

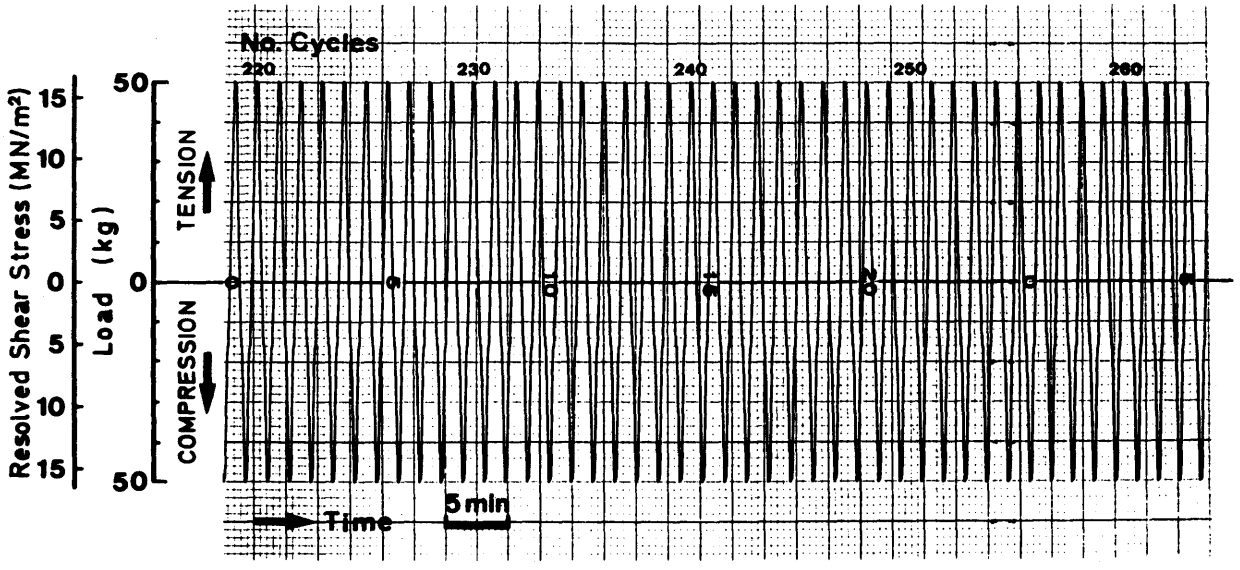


Fig. 7-5. Typical example of cyclic stress-time curve at 1073 K at the strain rate $8.9 \times 10^{-4}$ $s^{-1}$ under constant stress amplitude of $\pm$ 16 $MN/m^2$ (wave shape due to continuous stress cycling). The number of cycles is indicated in the figure.

imens were cyclically deformed for 50, 330 and 1000 cycles. The development of slip-band distribution with the number of cycles is shown in Fig. 7-6. After 50 cycles (a), the most area of the gauge length is covered with a number of fine slip bands which belong to either the primary or the secondary slip system. With increasing number of cycles (b), however, the slip bands of the primary system become to develop still more although faint slip bands of the secondary systems are sometimes seen. It is observed in the long run (c) that long straight slip bands of the primary system develop over the entire area on the surface and that macroscopic inhomogeneities in the slip-band distribution are scarcely observed.

### 7.3.2. Dislocation Configurations Induced by Cyclic Deformation

Figure 7-7 shows the dislocation configuration after 330 cycles on the primary slip plane (111). At this stage, both the dislocation configuration and the density of dislocations seem to be apparently similar to those found, especially at the lower yield point, in the tensile deformation. The average density of dislocations is, in this case, $1.0 \times 10^{8}$ $cm^{-2}$. The dominant features are long dislocation dipoles (about 10 microns in length) which have been formed by the mutual trapping over a portion of their length during cyclic deformation. These dipoles tend to be oriented along the $[1\bar{2}1]$ direction, which is perpendicular to the direction of the primary Burgers vector $[\bar{1}01]$. Although the dipole configuration is also revealed in the early

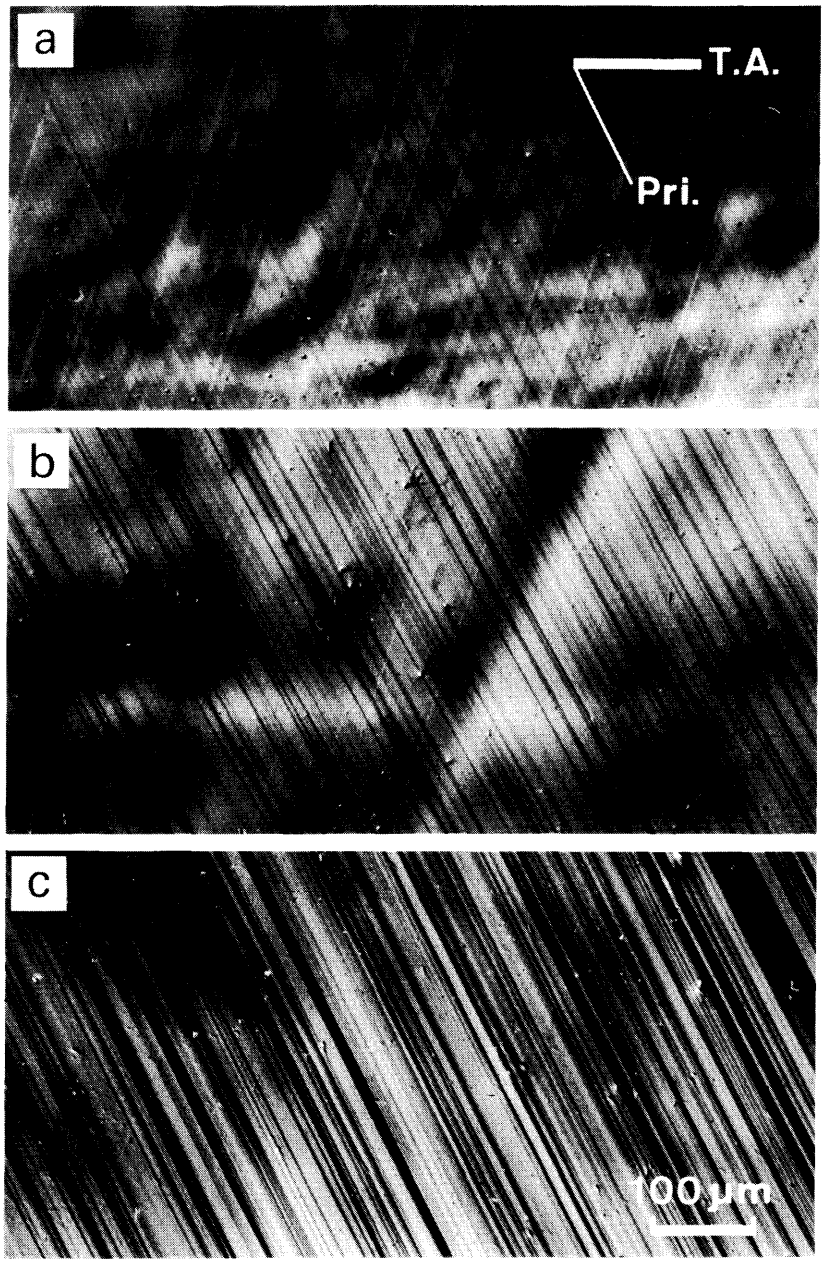


Fig. 7-6. Development of slip-band distribution with the number of cycles on the top surfaces of specimens cyclically deformed at 1073 K at the strain rate of $8.9 \times 10^{-4}$ $s^{-1}$. Each specimen was cycled under constant stress amplitude of $\pm$ 16 $MN/m^2$ for 50 cycles (a), 330 cycles (b) and 1000 cycles (c).

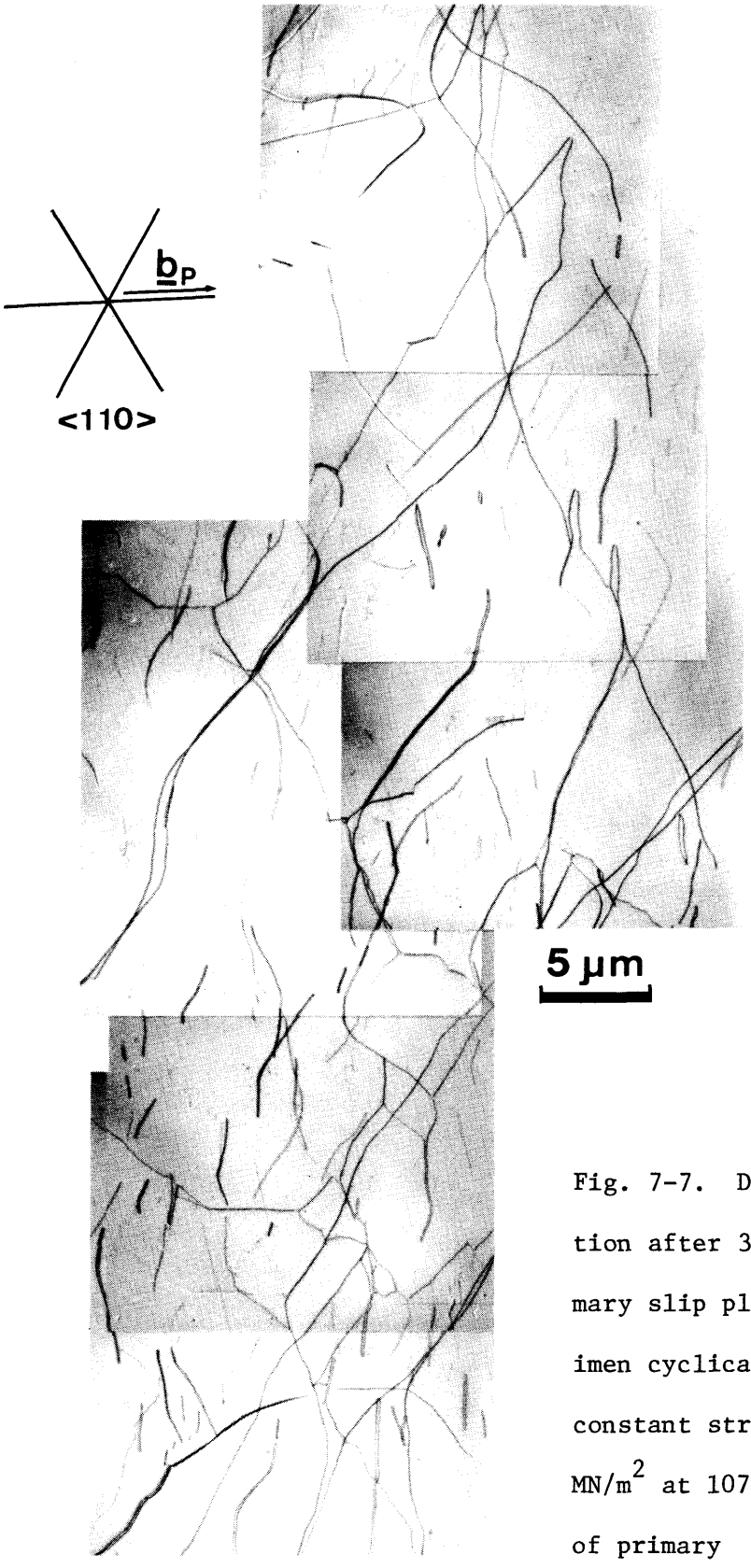


Fig. 7-7. Dislocation configuration after 330 cycles on the primary slip plane (111) in the specimen cyclically deformed under constant stress amplitude of $\pm$ 16 $MN/m^2$ at 1073 K. The direction of primary Burgers vector is shown in the figure.

stages of tensile deformation [3], the density of dipoles in the cyclically deformed crystal is much higher than that in the crystal deformed in tension. Furthermore, elongated, closed-loop dipoles are found to lie along the $[1\bar{2}1]$ direction. It is noted that they are sometimes bent. Numerous dipoles, oriented along $[1\bar{1}0]$ and $[0\bar{1}1]$, are observed in faint contrast. Similar faulted <110> dipoles are also found in copper crystals deformed in tension [11] and in push-pull [12]. It is known that faulted dipoles are formed by the dissociation of a primary <110> dipoles into two Shockley partials and two stair-rod dislocations linked by a stacking fault on an inclined {111} plane [13,14].

Very few primary screw dislocations are observed at this stage or at any subsequent stage of hardening. It is supposed that screw dislocations are mutually annihilated by cross slip during cyclic deformation.

Figure 7-8 shows the dislocation configuration after 1000 cycles on the primary slip plane (111). Continued cycling leads to a development of the dislocation bundles and also to the rapid increase in dislocation density; the average dislocation density is, in this case, $7.7 \times 10^8$ cm$^{-2}$. Contrast experiments have shown that most dislocations have the primary Burgers vector $\underline{b}_p = a/2[\bar{1}01]$ and that the secondary dislocation density is much lower than the primary dislocation density. The bundles of dislocations (multipoles) are predominant at this stage and they are oriented along the $[1\bar{2}1]$ direction. The majority of dislocations within these bundles are primary edge dislocations on parallel slip planes, which have interacted to form dipoles

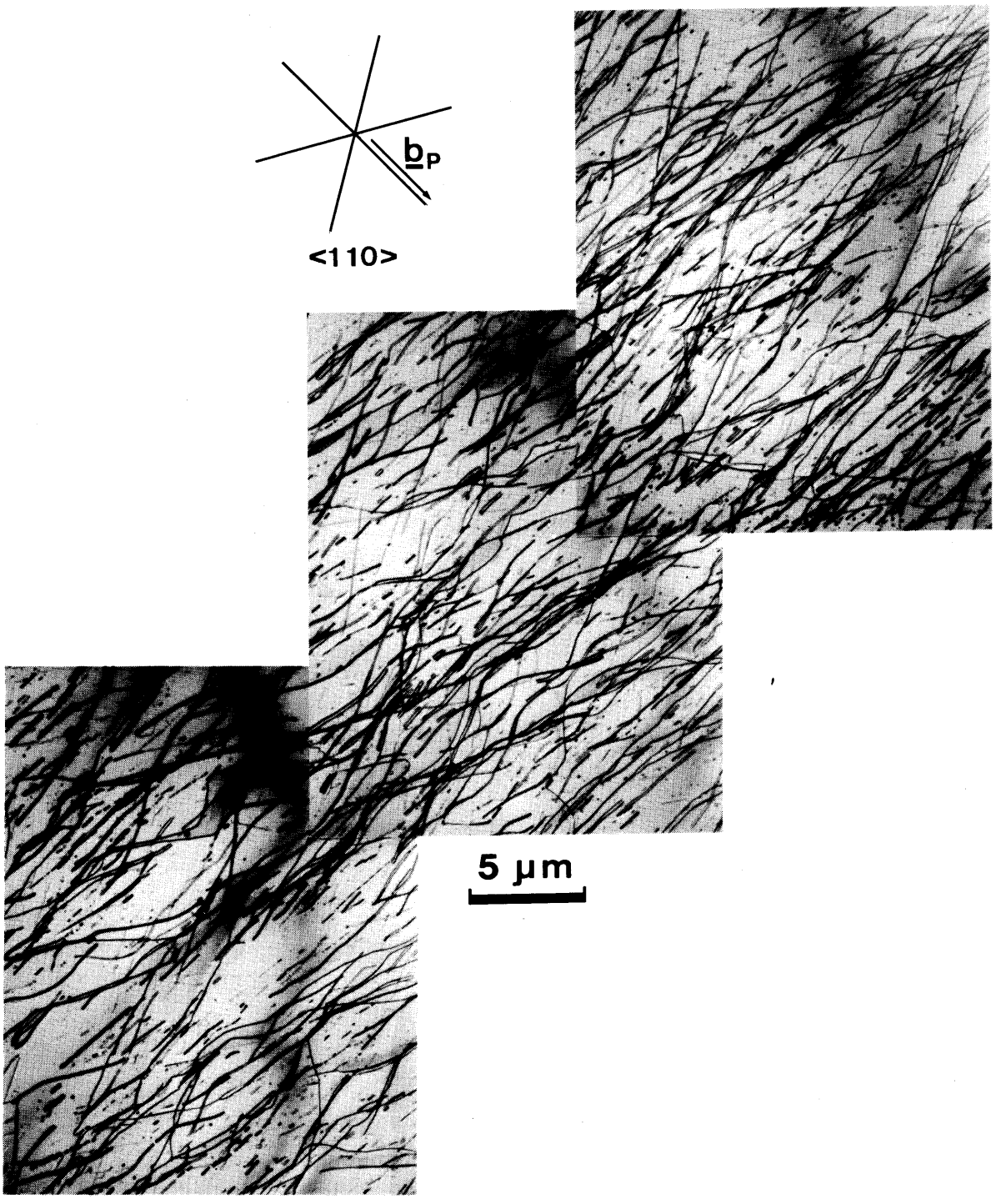


Fig. 7-8. Dislocation configuration after 1000 cycles on the primary slip plane (111) in the specimen cyclically deformed under constant stress amplitude of $\pm$ 16 MN/m$^2$ at 1073 K. The direction of primary Burgers vector is shown in the figure.

and multipoles. Faulted <110> dipoles are also seen, but their density appears to be less than at 330 cycles. These primary dipoles and faulted dipoles within bundles have been fragmented into much shorter length for larger number of cycles. This chopping-up of the long dipoles into short segments is considered to be due to the interaction with dislocations moving on the secondary slip planes. As a result, there is the great quantity of debris in the form of many small or elongated loops. One point to be noted here is that local variation in debris density has been developed to some extent at this stage and dislocations tend to be held up at the high-density region.

In addition, one can discern an elementary cell structure emerging as the dislocation bundles link up into continuous structure. This cell-like structure is still rather irregular and a complete cell structure, as observed in germanium crystals [4], has not been revealed at this stage.

Figure 7-9 shows the dislocation configuration on the cross slip plane $(1\bar{1}1)$ in the same crystal as in Fig. 7-8. The density of dislocations is much lower than that on the primary slip plane, and the bundles of dislocations are separated by regions relatively free of dislocations. This bundle consists of dipoles, faulted dipoles, miltipoles and tangled edge dislocations. The area of bundled region is very small and most dislocations which are not forming the bundles tend to line in a rectilinear figure. A unique dipole configuration is seen at the top of the figure. The less activation of secondary systems at this stage corresponds well with the surface observations shown in Fig. 7-6.

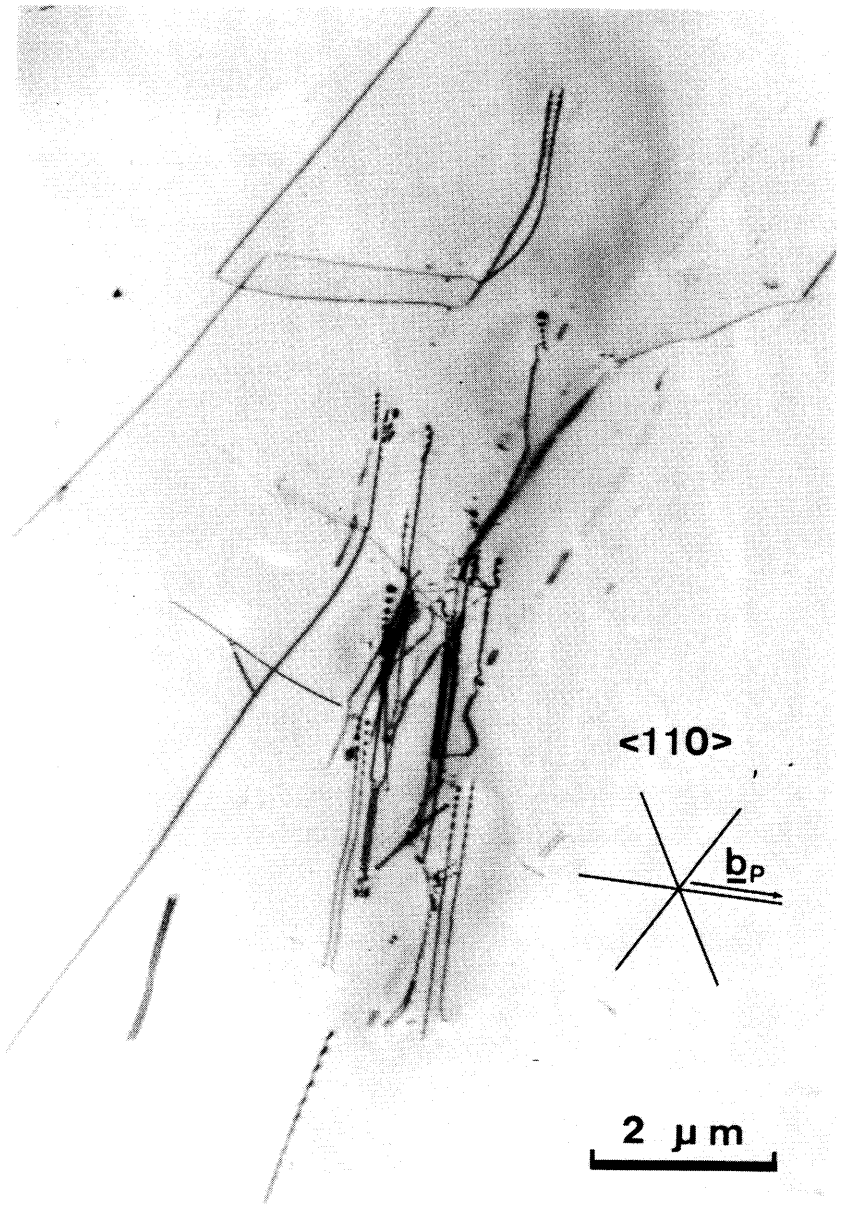


Fig. 7-9. Dislocation configuration after 1000 cycles on the cross slip plane $(1\bar{1}1)$ in the same specimen as in Fig. 7-8. The direction of primary Burgers vector is shown in the figure.

## 7.4. DISCUSSION

On the basis of the present observations mentioned in Section 7.3., it is concluded that the fatigue hardening of silicon crystals takes place during cyclic deformation even in the elastic region, where the stress level of the amplitude is about one-seventh of the yield stress. As a result, the dislocation configurations characteristic of fatigue cycling have been observed, which are a little different from those found in unidirectional deformation.

Now, the relationship between fatigue and unidirectional hardening is discussed, compared with the dislocation configurations found in unidirectional deformation of silicon crystals [3,13,14,15] and also those of f.c.c. metals [11,12,16,17]. It is known that strong parallels exist between low-amplitude fatigue and stage I hardening, and between high-amplitude fatigue and stage II hardening [18]. The observations of microscopic configurations and dislocation density indicate that the dislocation morphology at 330 cycles and at 1000 cycles are relatively similar to those observed at the lower yield point and in the stage I, respectively, in tensile deformation of silicon crystals. Edge dislocation bundles and dipoles are common to both the cyclic and unidirectional mode of deformation in the early stages. In cyclic deformation, however, it is very impressive that the majority of dislocations assume the dipole configuration even in the initiation of cycling and that screw dislocations are notably absent probably due to the mutual annihilation

by cross slip.

As the dislocation configurations in silicon crystals deformed in tension are strikingly similar to those in f.c.c. metals [3], there is also a close resemblance in fatigue hardening process between silicon crystals and f.c.c. metals, especially in the early stages of rapid hardening. Common observations, which are obtained with the development of rapid hardening, are as follows;

(i) The number of dislocation bundles per unit volume increases,

(ii) The density of dislocations within the bundles increases,

(iii) The length of $[1\bar{2}1]$ dipoles in the bundles decreases sharply,

(iv) The number of <110> faulted dipoles decreases.

On the other hand, several attempts have been made to activate dislocation motion in silicon crystals at temperatures below Tm/2 (Tm: melting temperature in Kelvin) [19-21]. One technique for the suppression of brittle behaviour is compression by superimposing a confining pressure [20]. In this case, however, it is necessary to deform the crystals under a hydrostatic pressure of 1500 $MN/m^2$. By applying the technique employed in the present study, the dislocation motion is expected to be activated even at temperatures below 900 K during the stress-controlled cyclic deformation. Actually, a slip band has been formed at 873 K when the specimen was subjected to a stress of 36 $MN/m^2$ in the load-unload stress cycles in compression. This leads to an anticipation that cyclic deformation in the elastic region will permit the dislocation activity at low temperatures,

where silicon crystals are extremely brittle.

## REFERENCES


[1] H. Alexander and P. Haasen: Solid State Phys. 22 (1968) 27.

[2] I. Yonenaga and K. Sumino: Phys. Status Solidi (a) 50 (1978) 685.

[3] Y. Nishino, H. Saka and T. Imura: Phys. Status Solidi (a) 70 (1982) 729.

[4] W.R. Scoble,Jr. and S. Weissmann: Cryst. Lattice Defects 4 (1973) 123.

[5] J. Chikawa, I. Fujimoto and T. Abe: Appl. Phys. Lett. 21 (1972) 295.

[6] K. Sumino and H. Harada: Philos. Mag. A44 (1981) 1319.

[7] Y. Nishino, M. Suzuki, T. Tono, H. Saka and T. Imura: Jpn. J. Appl. Phys. 20 (1981) 1533.

[8] Y. Nishino and T. Imura: Jpn. J. Appl. Phys. 21 (1982) 1283.

[9] Y. Nishino and T. Imura: Phys. Status Solidi (a) 73 (1982) 173.

[10] J.W. Steeds: Proc. R. Soc. London A 292 (1966) 543.

[11] J.R. Hancock and J.C. Grosskreutz: Acta Metall. 17 (1969) 77.

[12] A. Seeger and G. Wobser: Phys. Status Solidi 18 (1966) 189.

[13] J.W. Steeds: Plilos. Mag. 16 (1967) 711.

[14] V.G. Govorkov, Yu.V. Malov, V.I. Nikitenko and I.S. Smirnova: Sov. Phys. -Crystallogr. 11 (1966) 235.

[15] A.L. Aseev, Yu.N. Golobokov and S.I. Stenin: Phys. Status Solidi (a) 28 (1975) 355.

[16] H. Mughrabi: Constitutive Equations in Plasticity, ed. A.S. Argon (M.I.T. Press, Cambridge, 1975) p.199.

[17] J.C. Grossgreutz and H. Mughrabi: Constitutive Equations in Plasticity, ed. A.S. Argon (M.I.T. Press, Cambridge, 1975) p. 251.

[18] S.J. Basinski and Z.S. Basinski: Dislocations in Solids, ed. F.R.N. Nabarro (North-Holland, Amsterdom, 1980) Vol. 4 p. 261.

[19] C.E. Feltner and C. Laird: Acta Metall. 15 (1967) 1633.

[20] M.J. Hill and D.J. Rowcliffe: J. Mater. Sci. 9 (1974) 1569.

[21] K. Wessel and H. Alexander: Philos. Mag. 35 (1977) 1523.

[22] J. Castaing, P. Veyssière, L.P. Kubin and J. Rabier: Philos. Mag. A44 (1981) 1407.

# CHAPTER 8

# THERMAL STRESS AND VISCOELASTIC BEHAVIOUR OF OXIDE FILMS

## 8.1. INTRODUCTION

It is well known that an oxide film thermally grown at a high temperature on silicon crystals by steam oxidation involves internal stress after cooling because of the difference in thermal expansion between the oxide film and the silicon crystal. This stress also brings lattice distortion in the crystal below the oxide film. Therefore, when the oxide film is removed partly from the crystal surface, a high strain is accomodated in the crystal at the boundary between the oxidized region and the oxide-removed region. In this case, an enhanced X-ray diffraction contrast appears along the oxide boundary [1,2]. The strain introduced at the boundary is proportional to the force acting on the boundary [1]. This force acting on the boundary can be evaluated by the X-ray section topography method [2-4] and it has been recognized that, being independent of the oxidation temperature, the stress accomodated in the film is constant [2].

On the other hand, although the deposition of nitride film

is widely employed in silicon device technology, the stress effect of the nitride film formed on the crystal surface often leads to the generation of dislocations in the crystal during thermal treatment since the stress in the nitride film is scarcely changed at increased temperature [5,6]. The fact that the stress is not changed with temperature is due to the reason that this stress is not the thermal stress caused by the difference in thermal expansion between the nitride film and the silicon crystal but the inherent intrinsic stress produced during the film deposition [6]. These dislocations are detrimental to device properties. Therefore, an oxide film is first formed on a silicon crystal before the deposition of nitride film so as to avoid the dislocation generation. It has been assumed so far that this oxide film suppresses the dislocation generation due to its viscoelastic behaviour at increased temperatures [7]. However, the viscoelastic behaviour of oxide films has not yet been well investigated systematically by experiments.

In order to clarify the viscoelastic behaviour of oxide films on silicon crystals, it is necessary to know the change of stress in the film accompanied with the changes of heat-treatment temperature and heating time by observing the change of strain contrast along the oxide boundary and/or the change of curvature of the oxidized region. In the experimental study described in this chapter, the change of strain contrast along the oxide boundary during thermal cycling is investigated by means of real-time X-ray topographic observations. Being based on the obtained results, the viscoelastic behaviour of oxide films is discuss-

ed in detail.

## 8.2. EXPERIMENTAL PROCEDURES

Specimens were prepared from dislocation-free silicon crystals (p-type, 8 - 12 ohm·cm) grown by the Czochralski technique; the surface orientation was parallel to (001) and the thickness was about 0.4 mm. They were chemically polished and steam-oxidized at 1273 K. Except for the half region of the crystal surface, the oxide film on the other half region was removed by chemical etching; the boundary between the oxidized region and the oxide-removed region was nearly parallel to the <110> direction. Different thicknesses of oxide were obtained by changing the time of oxidation from 10 min to 800 min at 1273 K, and the thickness of the film was measured by ellipsometry.

In order to observe the change of strain contrast along the oxide boundary at elevated temperatures, the specimen heating apparatus [8] described in Section 3.2. was set on a goniometer stage and in-situ thermal cycling experiments were performed in nitrogen ambient in the temperature range from 300 K to 1273 K. During the heat treatment, specimens were held by the specimen holder made of a silicon crystal, as illustrated in Fig. 8-1, so as not to introduce inhomogeneous strain at the specimen-holding part.

For the application of the Lang technique, Ag $K\alpha_1$ radiation was used under the operating condition of 50 kV and 1200 mA and

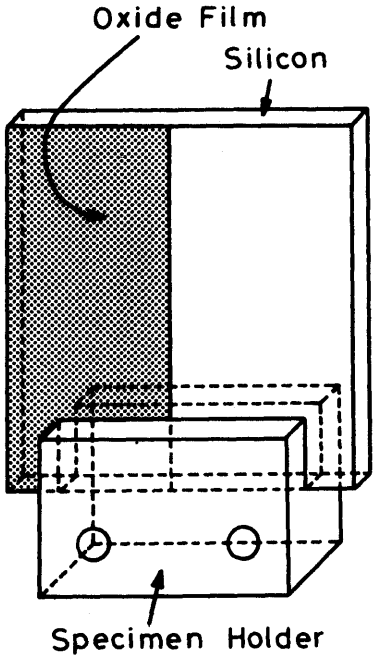


Fig. 8-1. Schematic illustration of specimen holder made of silicon crystal. Holding of specimen was performed by inserting it in the slit of the holder without introducing strain during heating.

symmetric 220 reflection of X-ray was employed throughout the present experiment. The change of strain contrast along the oxide boundary was continuously observed on a monitor TV and the synthesized TV images were simultaneously recorded by a VTR. The strain contrast along the boundary was also examined using Ilford-L4 nuclear research plates to determine the intensity distribution across the boundary in the traverse topograph by using an auto-densitometer (SYNTEX, AD-1).

## 8.3. EXPERIMENTAL RESULTS

In the case of the observation using the reflection vector, the direction of which is perpendicular to that of the oxide boundary, the enhanced black contrast accompanied with white

contrast appeared along the oxide boundary. This is due to the strain gradient in the crystal at the oxide boundary. By traversing the specimen across the oxidized region, the diffraction image was observed to shift gradually to one direction. This suggests that the specimen was elastically warped across the oxidized region and that it becomes convex to the oxide side. In this case, the entire area of warped crystals can be observed by employing the chromatic-aberration correction (CAC) scanning and an orientation-tuning device [9]. The curvature of the oxidized region can be also estimated by using the CAC technique and was determined by measuring the magnitude of shift of the diffraction line on a TV screen, as shown in Fig. 8-2. Each circle represents the experimental value averaged over five measurements and the vertical line attached to each circle represents the scatter range of the observed values. It is noted that the curvature of the oxidized region increases linearly with increase in the oxide thickness. Moreover, the enhanced diffracted intensity due to the strain along the oxide boundary was determined by densitometry and the relationship is also shown in Fig. 8-2 as a function of the oxide thickness. In this case, the darkness measured in the traverse topograph was regarded as the diffracted intensity and the normalized darkness indicates the maximum darkness near the oxide boundary normalized by the darkness far from the oxide boundary. The enhanced diffracted intensity from the oxide boundary was also found to be proportional to the oxide thickness except for the very small thickness of oxide.

The change of strain contrast along the oxide boundary was

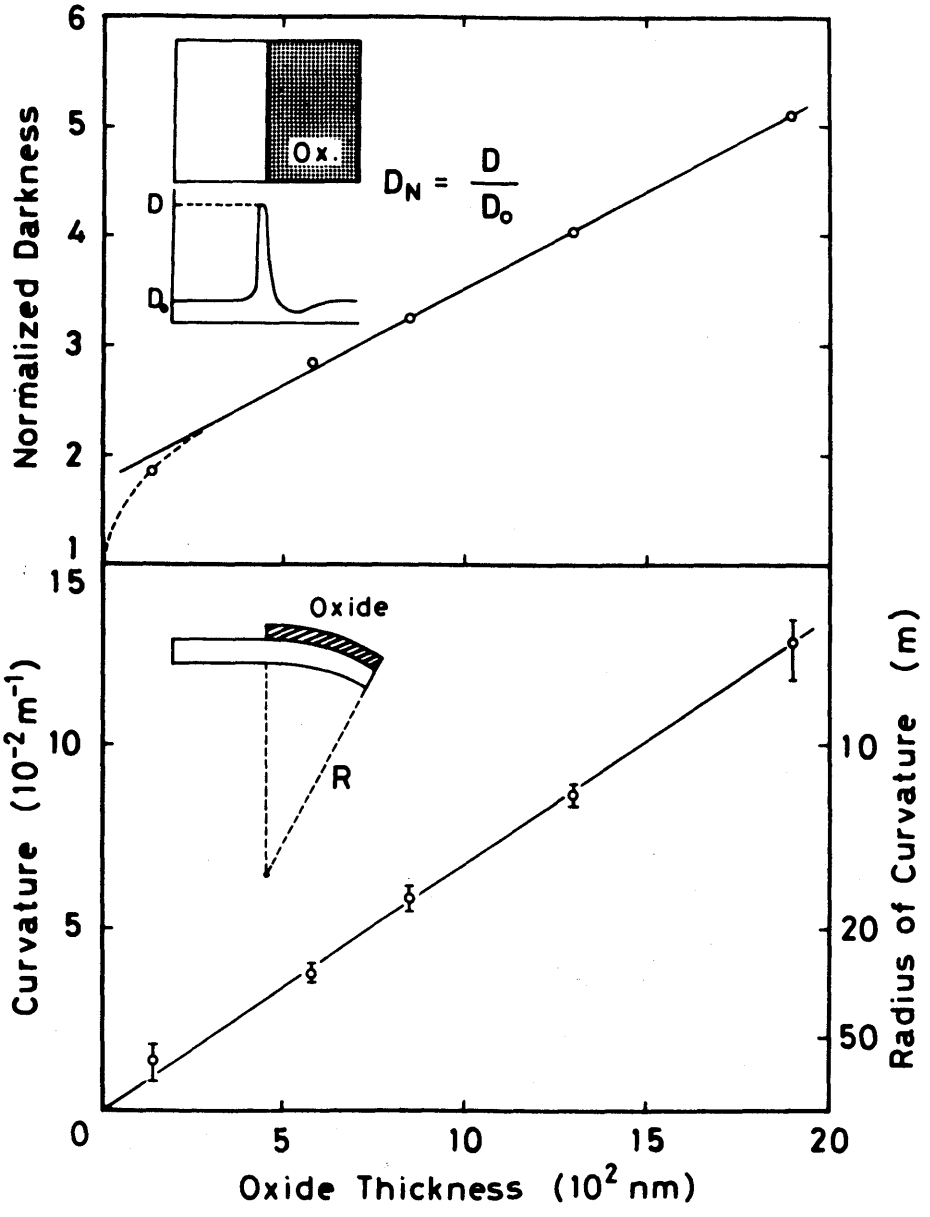


Fig. 8-2. Curvature of the oxidized region (bottom) and normalized darkness ($D_N$ = D/Do) at the oxide boundary (top) as a function of oxide thickness. The curvature was determined by measuring the magnitude of shift of the diffraction line on a TV screen, and the darkness was determined by densitometry.

observed continuously during thermal cycling in the temperature range from 300 K to 1273 K. The pictures shown in Fig. 8-3 are synthesized TV images at 300 K (a), 1123 K (b), 1173 K (c), 1273 K (d), 1173 K (e), 1123 K (f) and 300 K (g), respectively. The straight line with black contrast is the oxide boundary and in this case the oxide film of 1900 nm thick remained on the right-hand region of the boundary. Before heating, the strong black contrast appeared along the oxide boundary (a). The strain contrast, however, decreased with increasing temperature (b) (c), and the contrast almost disappeared at 1273 K which is the oxidation temperature (d), as indicated by the arrows. By cooling the specimen subsequently, the strain contrast reappeared along the oxide boundary and increased with decreasing temperature (e) (f). After cooling, the strong black contrast was again observed to appear along the boundary (g), of which intensity was about the same as that before heating. In this manner, the strain contrast due to the strain accomodated in the crystal at the oxide boundary changes reversively in company with the change of temperature. It can be seen, for instance, from the strain contrasts observed at 1173 K that the contrast at 1173 K after heating to 1273 K (e) was not so strong as that at 1173 K before heating to 1273 K (e). This change of strain contrast before and after heating is considered to be due to the viscoelastic behaviour of the oxide film.

The viscoelastic behaviour of oxide film could be observed during the isothermal heat treatment at a temperature below the oxidation temperature (1273 K). Figure 8-4 shows the change of

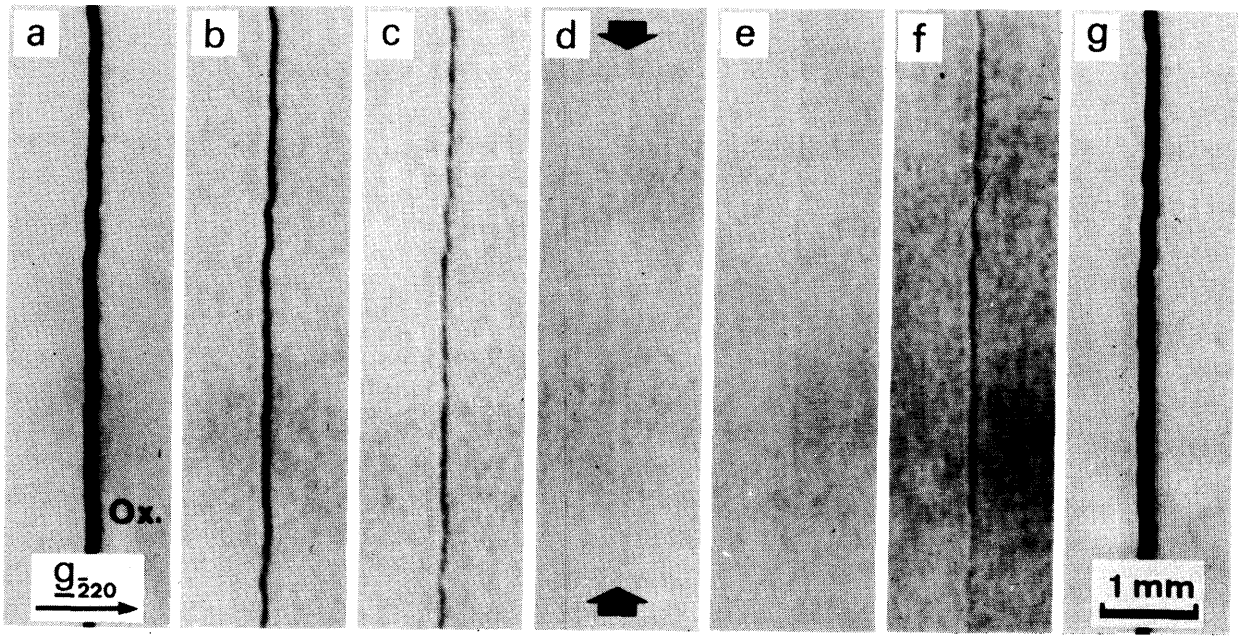


Fig. 8-3. Change of strain contrast along the oxide boundary during thermal cycling. The oxide film (Ox.) of 1900 nm thick remains on the right-hand region of the boundary in this case. Synthesized TV images at 300 K (a), 1123 K (b), 1173 K (c), 1273 K (d), 1173 K (e), 1123 K (f) and 300 K (g): $\bar{2}20$ reflection.

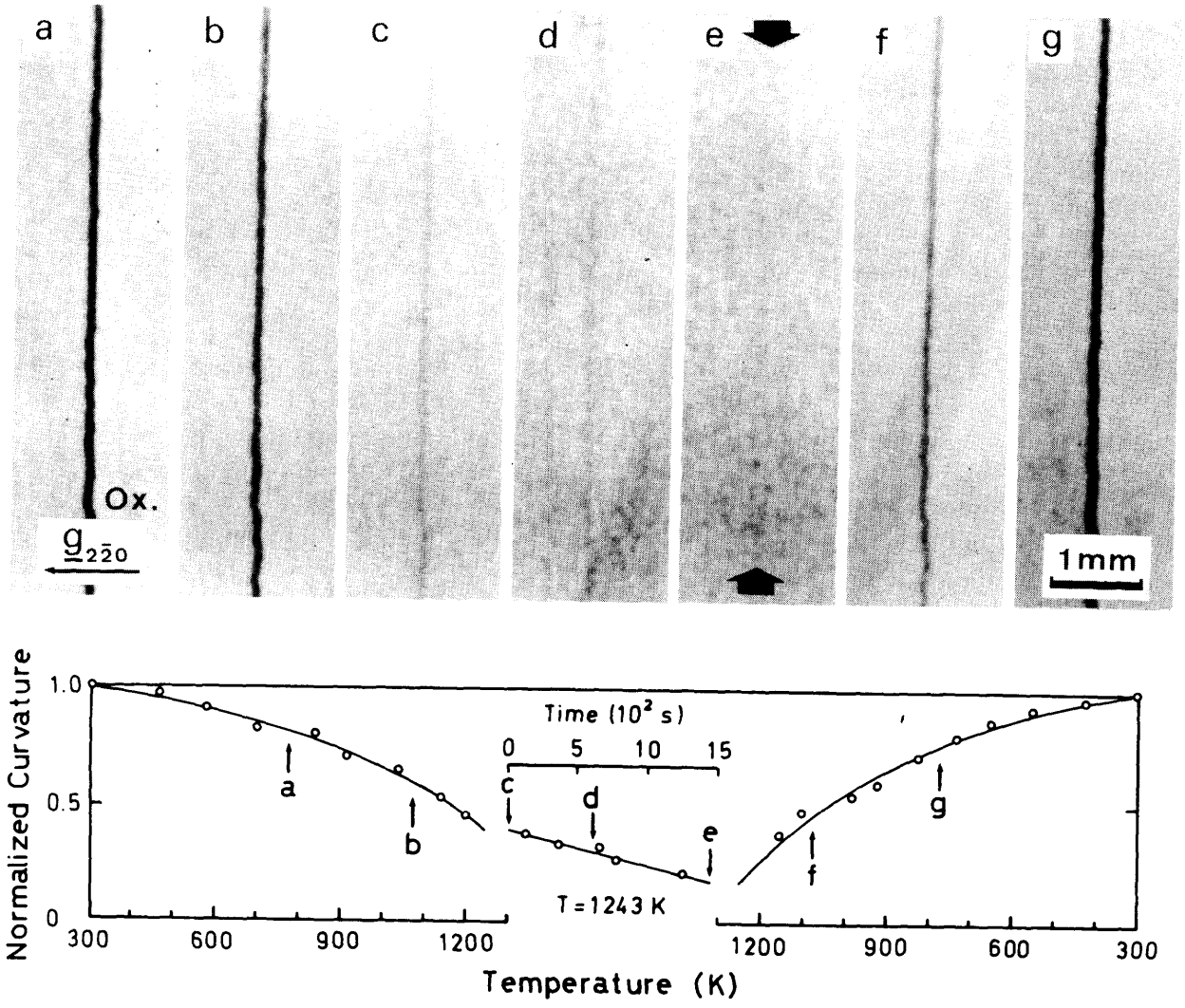


Fig. 8-4. Change of strain contrast along the oxide boundary and change of curvature of the oxidized region during heat treatment. The oxide film (Ox.) of 850 nm thick remains on the right-hand region of the boundary. Synthesized TV images at 773 K (a), 1073 K (b), 1243 K (c), 1243 K for 10 min (d), 1243 K for 24 min (e), 1073 K (f) and 773 K (g): 2$\bar{2}$0 reflection. The curvature was measured simultaneously with the heat treatment.

strain contrast along the boundary of the oxide of 850 nm thick during the heat treatment, and the change of curvature of the oxidized region is also shown in the bottom of the figure. They are synthesized TV images at 773 K (a), 1073 K (b), 1243 K (c), 1243 K for 10 min (d), 1243 K for 24 min (e), 1073 K (f) and 773 K (g), respectively. The strain contrast along the oxide boundary decreased with increasing temperature (a) (b) (c). By maintaining the specimen at 1243 K which is lower than the oxidation temperature (1273 K), the contrast decreased still more (d) and disappeared after maintaining for 24 min (e), as indicated by the arrows. The disappeared contrast, however, reappeared along the boundary by cooling and increased with decreasing temperature (f) (g). On the other hand, it can be seen that the change of curvature corresponds completely to that of strain contrast; the curvature decreased with decreasing contrast and increased with increasing contrast.

The viscoelastic behaviour of oxide films is supposed to be due to the thermally activated process since the contrast along the oxide boundary decreased with time by the isothermal heat treatment. The specimens were, then, adjusted to a particular temperature between 1073 K and 1273 K and maintained at this temperature until the strain contrast has disappeared. Times necessary to get the disappearance of strain contrast were measured at different temperatures. Figure 8-5 shows the relation between the time and the annealing temperature for the four kinds of oxide thicknesses indicated in the figure (a, b, c, d). In this case, the time required to heat the specimen from 873 K to

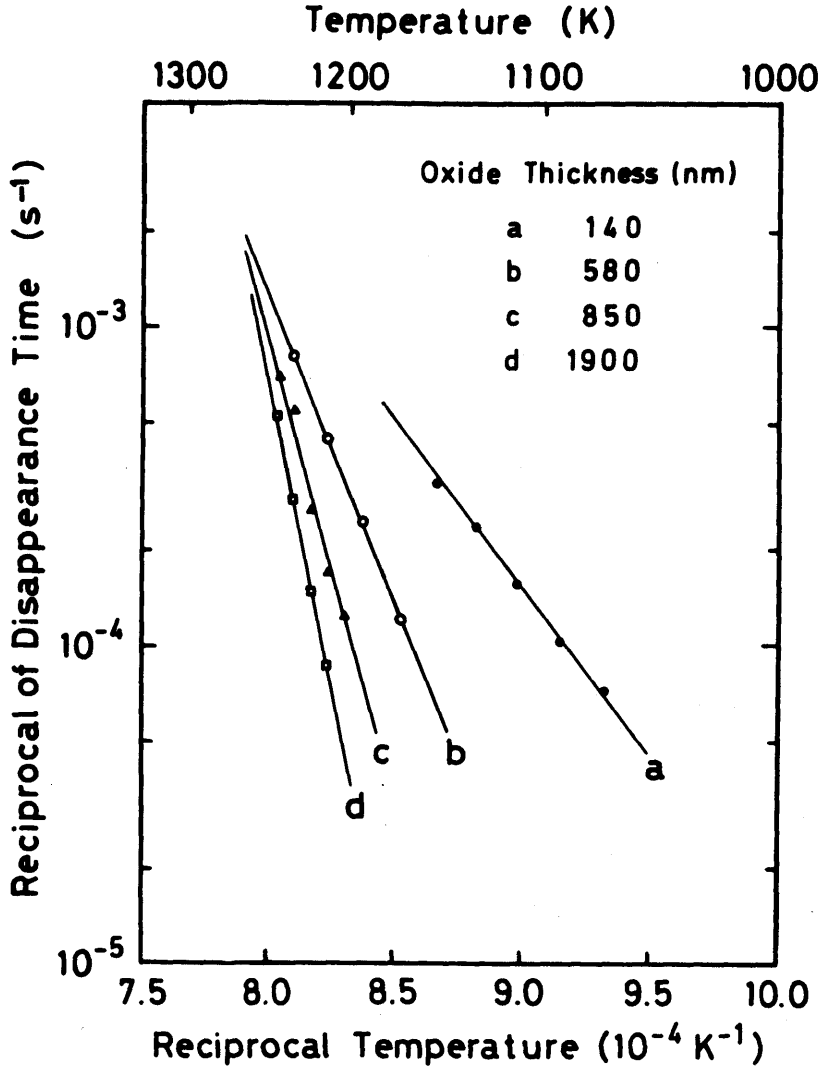


Fig. 8-5. Times necessary to get the disappearance of strain contrast along the oxide boundary as a function of annealing temperature. Oxide thickness: (a) 140 nm, (b) 580 nm, (c) 850 nm, (d) 1900 nm.

a particular annealing temperature was within a few minutes and the temperature of the specimen was kept constant with the accuracy of ± 2 K. As a general tendency, it can be seen that the viscous flow of oxide occurred in shorter time for higher temperature in the case of the same thickness of oxide. In company with the increment of oxide thickness, however, the temperature for the viscous flow became higher and the time necessary to get the disappearance of contrast became longer.

On the other hand, the thermal cycling experiment was performed by using the specimen which was cooled slowly after maintaining it at 1223 K until the strain contrast along the oxide boundary (oxide thickness: 850 nm) disappeared. The pictures shown in Fig. 8-6 are synthesized TV images at 300 K (a), 1073 K (b), 1173 K (c), 1233 K (d), 1173 K (e), 1073 K (f) and 300 K (g), respectively. The strong black contrast appeared along the oxide boundary before heating (a) and decreased with increasing temperature (b) (c). The contrast, however, almost disappeared at 1223 K where the viscous flow of oxide previously occurred, and disappeared entirely at 1233 K (d). By cooling the specimen, the strain contrast gradually reappeared along the oxide boundary (e) (f) (g).

## 8.4. DISCUSSION

On the basis of the observations mentioned in Section 8.3., the changes of strain contrast along the oxide boundary are con-

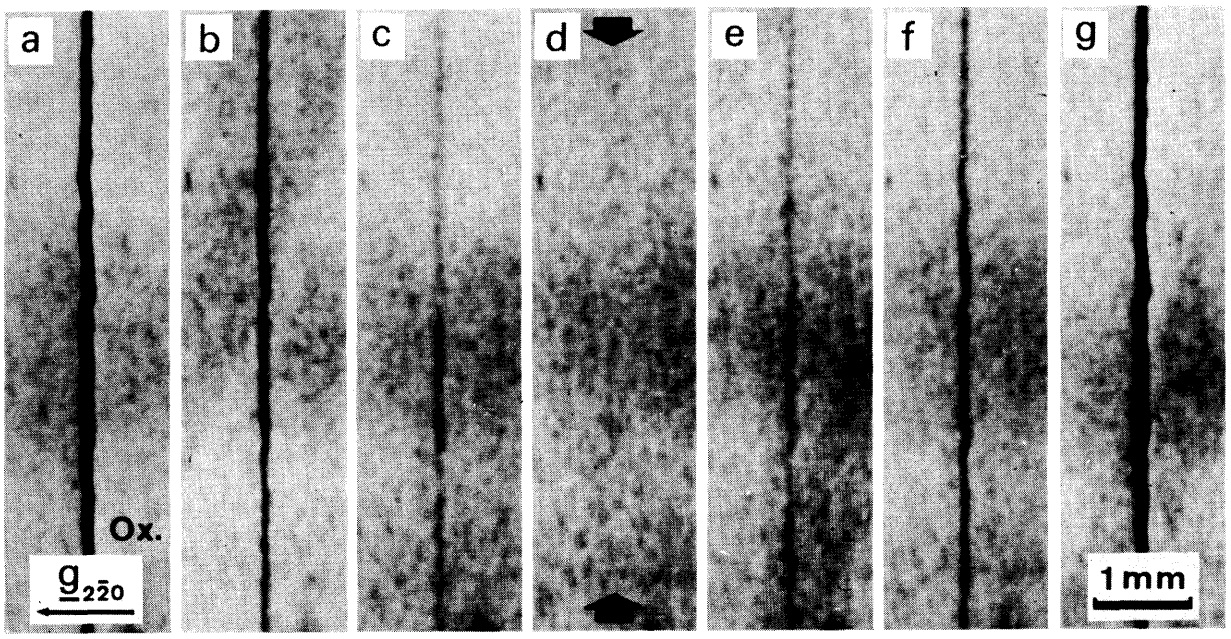


Fig. 8-6. Change of strain contrast along the oxide boundary during thermal cycling. The specimen was preliminary maintained at 1223 K until the strain contrast disappeared before cycling. The oxide film (Ox.) of 850 nm thick remains on the right-hand region of the boundary. Synthesized TV images at 300 K (a), 1073 K (b), 1173 K (c), 1233 K (d), 1173 K (e), 1073 K (f) and 300 K (g): $2\bar{2}0$ reflection.

sidered to be caused by the viscous flow of oxide films. Accordingly, as a result of the viscoelastic behaviour of oxide films, the thermal warping caused by oxidation is relaxed and the stress in the film also decreases at the same time.

This viscoelastic behaviour of oxide films has been considered so far to take place in the temperature range above 1173 K [2,10,11]. From the result shown in Fig. 8-5, however, it is obvious that the viscous flow can occur even at 1073 K in the case of small thickness of oxide. Moreover, since the strain contrast along the oxide boundary has decreased with increasing temperature, it seems that the viscous flow starts upon heating even at a temperature relatively lower than the oxidation temperature. It is expected, therefore, that the viscoelastic behaviour can be observed by maintaining the oxide film at lower temperature than 1073 K although the longer annealing time is necessary.

It has been recognized that the internal stress accomodated in the oxide film is constant and independent of oxidation temperature [2]. If the origin of the stress is only due to the difference in thermal expansion between the oxide and the silicon crystal, it is reasonably expected that the oxide film prepared at a high temperature will show a higher stress at room temperature. As mentioned in Section 8.3., however, the strain contrast along the oxide boundary has disappeared by maintaining the specimen at temperatures below the oxidation temperature. This means directly that the oxide film flows even below the oxidation temperature although the viscosity also becomes higher

with decreasing temperature. Furthermore, as seen in Fig. 8-3, the strain contrast observed at 1173 K after the viscous flow at the oxidation temperature (1273 K) is weaker than that obtained at 1173 K before heating to the oxidation temperature. The above result indicates that once the viscous flow of oxide occurs, the oxide continues to flow until the crystal is cooled down from the oxidation temperature to a temperature where the viscosity of oxide becomes very high. It is reasonable, therefore, to expect that the stresses in the films grown at different temperatures are constant.

On the other hand, when heating the specimen which had been cooled down after maintaining it at a temperature below the oxidation temperature until the strain contrast along the oxide boundary had disappeared, the contrast disappeared immedately at a temperature a little higher than that of the aforementioned pre-treatment, as shown in Fig. 8-6. It seems to be as if the oxide film remembered the temperature where the viscous flow has occurred previously. Here, it is supposed that the atomic arrangement of oxide changes to a certain degree due to the viscous flow at high temperatures. This changed atomic-arrangement would be frozen in during cooling to room temperature. In the next heating process, the atomic arrangement in oxide, at the temperature of the previous heat treatment, is already in the condition obtained after the viscous flow. It is considered, therefore, that the viscous flow occurs immediately in this case and accordingly the strain contrast also disappears immediately.

## REFERENCES


[1] I.A. Blech and E.S. Meieran: J. Appl. Phys. 38 (1967) 2913.

[2] J.R. Patel and N. Kato: J. Appl. Phys. 44 (1973) 971.

[3] N. Kato and J.R. Patel: J. Appl. Phys. 44 (1973) 965.

[4] Y. Ando, J.R. Patel and N. Kato: J. Appl. Phys. 44 (1973) 4405.

[5] S. Isomae, M. Nanba, Y. Tamaki and M. Maki: Appl. Phys. Lett. 30 (1977) 564.

[6] M. Tamura and H. Sunami: Jpn. J. Appl. Phys. 11 (1972) 1097.

[7] S. Isomae, Y. Tamaki, A. Yajima, M. Nanba and M. Maki: J. Electrochem. Soc. 126 (1979) 1014.

[8] Y. Nishino, M. Suzuki, T. Tono, H. Saka and T. Imura: Jpn. J. Appl. Phys. 20 (1981) 1533.

[9] J. Chikawa, I. Fujimoto and Y. Asaeda: J. Appl. Phys. 42 (1971) 4731.

[10] E.P. EerNisse: Appl. Phys. Lett. 30 (1977) 290.

[11] W. Hartmann and G. Franz: Appl. Phys. Lett. 37 (1980) 1004.

# CHAPTER 9

# SUMMARY AND CONCLUSIONS

With the recent progress of silicon device, great attentions have been directed to how dislocations are generated, moved and multiplied in silicon crystals during thermal processing, since these dislocations bring about detrimental effects on the device performances. In order to develop effective means for controlling the dislocation generation in device elements, first of all it is necessary to understand basic processes of generation and multiplication of dislocations in a simple stress condition such as in tension.

Plastic deformation of crystals is essentially a dynamical phenomenon and hence dislocation processes during deformation should be investigated dynamically. Recent development of the ultra high intensity X-ray generator has made it possible to observe dynamical phenomena occurring in bulk crystals by means of X-ray topography. The new technique based on real-time X-ray topography has been employed to investigate dynamically the generation and multiplication of dislocations in silicon crystals at elevated temperatures.

* * *

In Chapter 1, the historical view of the studies on the deformation and the behaviour of dislocations in silicon crystals are summarized at first and the aims of the present studies are also described. In the present studies, the mechanical behaviour of silicon crystals has been investigated by high-temperature tensile deformation and cyclic deformation, adopting the electron microscope observations of deformed crystals at the same time. In order to observe dynamically the dislocation processes in stressed crystals, the high-temperature deformation apparatus has been newly constructed and combined successfully with a real-time X-ray topographic system consisting of a Lang-type goniometer and a video recording system. By means of real-time X-ray topographic observations, the generation process and the movement of dislocations in highly perfect silicon crystals have been investigated under various deformation conditions. Some of the process-induced defects which are observed practically in device technology have been also studied directly by in-situ thermal cycling experiments.

In Chapter 2, the characteristics of mechanical properties of Czochralski silicon crystals as well as the features of dislocation distributions in deformed crystals are described. Especially, the dislocation configurations developed during high-temperature tensile deformation have been investigated in detail by means of transmission electron microscopy. The stress-strain behaviour is characterized by (i) an extremely high upper yield stress, (ii) a sharp stress drop after the yielding and (iii) a heterogeneous deformation from the upper to the lower yield

point by means of the propagation of Lüders bands. It is found that both the upper and the lower yield stresses of Czochralski silicon crystals are well expressed by an equation of the following type:

$$\tau = A_o \dot{\varepsilon}^{1/n} \exp (U / kT) \qquad (9.1)$$

in accord with the results on float-zone silicon crystal and germanium crystal. It is also found that remarkable similarity exists in the dislocation configurations and also in the work-hardening process between silicon crystals and f.c.c. metals. At the lower yield point, long curved primary dislocations of several tens microns in length are most predominant and the dipole configuration is also revealed. The hardening mechanism of the stage I is characterized by the increase of the elastic interaction of primary dislocations which often assume dislocation dipoles of about 1 - 2 microns in length. In the stage II, more complicated configurations are realized since dislocations on the secondary slip system are activated and they interact with dislocations of the primary system, resulting in the formation of complicated networks. It is found that the dislocation density on the primary slip plane increases linearly with the strain during tensile deformation. Furthermore, since no oxide precipitates are observed by weak-beam electron microscopy, it is probable that high mechanical strength of Czochralski crystals is related to the formation of a Cottrell atmosphere around dislocations.

A high-temperature deformation apparatus has been newly

developed in order to carry out real-time X-ray topographic observations of dynamic phenomena occurring in deforming bulk crystals. Outline of the construction and the functional features of this apparatus are described in Chapter 3. Continuous video recording of dislocation processes occurring in a specimen of about 1mm thick under a known applied stress at elevated temperatures has become possible by combining this apparatus with an X-ray diffraction topographic system which consists of a 90 kW-class ultra high intensity X-ray generator, a Lang-type topographic goniometer and a TV-VTR recording system. The deformation apparatus constructed in the present study has the following functional features; (i) the apparatus can be set on a topographic goniometer stage and large area of a specimen, e.g. 45 mm in diameter (in the present apparatus), can be studied, (ii) a load-displacement curve can be recorded in parallel with recording of images of moving dislocations, (iii) a specimen can be stretched smoothly along a single axis with a given constant strain rate: the maximum applied load 80 N, the range of deformation speed $1.7 \times 10^{-2}$ to $1.0 \times 10^{-1}$ mm/min, (iv) studies can be made in any environmental gas atmosphere or in vacuum of about $2 \times 10^{-3}$ Pa at any temperature up to 1373 K, (v) Bragg condition can be kept or, if necessary, adjusted during deformation.

In the experimental study described in Chapter 4, the characteristics of the dislocation motion in silicon crystals during annealing have been investigated by means of in-situ X-ray topographic observations in the temperature range from 1173 K to 1273 K. The small displacements in position of the dislocation

segments take place to balance the friction force with the elastic interaction force between dislocations, so that the dislocation loop after annealing is characterized by a half-elliptic shape. From the analysises of (i) repulsive interaction between parallel dislocations with the same sign and of (ii) configurational changes of a dislocation half-loop, the friction force acting on dislocations can be determined at each annealing temperature by estimating the interaction force between dislocations. On the basis of the analysis of the temperature dependence of friction force, the activation energy for dislocation motion is evaluated to be 2.4eV for screw dislocation and 2.2eV for 60° dislocation.

In the experimental study described in Chapter 5, the deformation behaviour of Czochralski silicon crystals containing oxide precipitates has been investigated by means of real-time X-ray topographic observations. Oxide precipitates are introduced in crystals by the isothermal annealing and larger size of precipitates is obtained at higher annealing temperature. The increased generation and propagation of dislocations usually takes place preferencially at oxide precipitates before the macroscopic yielding. Fresh dislocations thus generated moved smoothly on the slip planes under applied stress at 1073 K, assuming a half-hexagonal shape with straight arms which are parallel to the <110> direction. The velocities of screw and 60° dislocations measured at 1073 K under the resolved shear stress of 4.4 $MN/m^2$ are $9.5 \times 10^{-5}$ cm/s and $1.2 \times 10^{-4}$ cm/s, respectively. The generation and propagation of dislocations hardly takes place

at relatively small precipitates because a higher stress is required to generate dislocations at small one. In the much higher stress level during ordinary macroscopic deformation, however, plastic flow is expected to occur around most oxide precipitates and the probability of pinning of dislocations is not high enough to cause precipitation hardening. These results are closely connected with the lowering of the yield stress observed in heat-treated crystals.

In the experimental study described in Chapter 6, notched silicon crystals have been deformed in tension at elevated temperatures and the incipient microplasticity associated with the notch has been investigated by means of real-time X-ray topographic observations. Above a stress level of about 20 $MN/m^2$ at 973 K, a plastic zone is formed around the notch tip, being accompanied by long-range elastic strain. The generation of dislocations on the slip planes parallel to the tensile axis is caused by the operation of a bending moment induced around the notch tip mainly by the activity of two slip systems with the maximum Schmid factor. In this case, unless other preferred sites for dislocation generation become activated during deformation, the operation of the bending moment at the notch tip plays an important role as the driving force of crack propagation.

In the experimental study described in Chapter 7, cyclic deformation behaviour of silicon crystals has been investigated for the first time by using a high-temperature fatigue apparatus which has been newly constructed for the present fatigue tests.

Especially, in order to verify whether or not the fatigue hardening takes place during cyclic deformation in the elastic region, the crystals have been stressed cyclically in tension and in compression at the stress level of about one-seventh of the upper yield stress at 1073 K. Electron microscope observations indicate that edge dislocation bundles and dipoles are common to both cyclic and tensile deformation in the early stages; dipoles are formed by a mutual-trapping mechanism. In cyclic deformation, however, the majority of dislocations assume the dipole configuration even in the initiation of cyclic deformation, and very few primary screw dislocations are observed probably due to a mutual annihilation by cross slip. In addition, there is a close resemblance in fatigue hardening process between silicon crystals and f.c.c. metals. That is, the bundles contribute to rapid hardening by providing effective barriers to continued dislocation motion on the primary and secondary slip systems.

In the experimental study described in Chapter 8, the viscoelastic behaviour of oxide films on steam-oxidized silicon crystals has been investigated by means of real-time X-ray topographic observations in the temperature range from 300 K to 1273 K. The observations have been performed on oxide films of various thicknesses grown at 1273 K. The strain contrast along the boundary between the oxidized region and the oxide-removed region decreases with increasing temperature and disappears not only at the oxidation temperature but also at temperatures fairly below the oxidation temperature by a prolonged annealing.

The curvature of the oxidized region is changed during heating-cooling thermal cycles in parallel with the change of strain contrast. This change of contrast due to the thermal cycling is reversible and found to be definitely due to the viscoelastic behaviour of oxide films at high temperatures. Therefore, once the viscous flow of oxide occurs, the oxide continues to flow until the crystal is cooled down to a temperature where the viscosity of oxide becomes very high. That is why the stresses in the films grown at different temperatures are constant.

* * *

On the basis of the obtained results in the present studies mainly by means of real-time X-ray topographic observations, some important informations are obtained in respect to the control of dislocation generation in device manufacturing processes.

Figure 9-1 shows a schematical cross-section of integrated circuit. When many microdefects are introduced inside the crys-

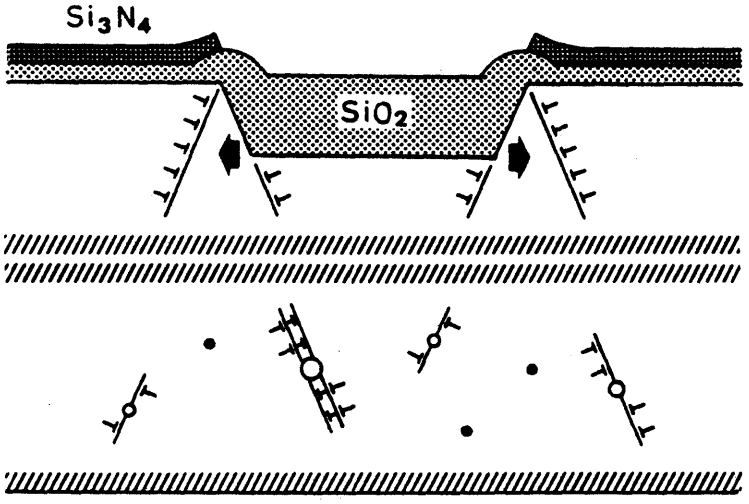


Fig. 9-1. Schematical cross-section of integrated circuit.

tal artificially by the intrinsic gettering method, the generation and propagation of dislocations is possible to take place preferentially at large oxide precipitates (open circles) under small thermal stress, leading to thermal slips. Whereas, it is very difficult to cause plastic flow at small precipitates (full circles) because a higher stress is required with decreasing precipitate size.

In the case of a recessed oxide structure as shown in Fig. 9-1, the edges in the groove are usually concentrated in stress (shown by the heavy arrows) due to the difference in thermal expansion between silicon crystal and oxide, so that dislocations are often introduced at the edges during thermal processing. When this groove, namely a notch in this case, is originally strain free, the crystal lattice merely deforms elastically due to the stress concentration. Dislocations are not generated until the edges in the groove are concentrated in the stress which exceeds the elastic-plastic transition stress.

These dislocations, when generated in float-zone crystals, can move easily at elevated temperatures under the influences of the elastic interaction forces between dislocations and also the image force near the surface. Moreover, the generation and multiplication of dislocations takes place during cyclic deformation in the elastic region. When subjected to thermal cycling and mechanical stress cycling, it is plausible that the dislocation motion is activated under stress cycles even if the stress level of amplitude is much lower than the macroscopic elastic limit.

When dislocations are nucleated in Czochralski crystals, however, they are thought to be locked rapidly by oxygen atoms during thermal processing, thus ceasing to act as multiplication centers.

On the other hand, although the stress effect of nitride film formed on a crystal surface often leads to the dislocation generation during thermal treatment, a thin oxide film formed intentionally between the nitride film and silicon crystal plays an important role in suppressing dislocation generation because of the viscoelastic behaviour of thin oxide film at high temperatures.

# ACKNOWLEDGEMENTS

The author would like to express his sincere appreciation to the continuous guidance and encouragement of Professor Toru IMURA of Nagoya University during the course of the present studies. He also wishes to express his gratitude to Professor Norio KATO of Nagoya University for the helpful discussions and suggestions in preparing this thesis.

The author would like to express his hearty thanks to Dr. Hiroyasu SAKA of Nagoya University for the stimulating discussions and suggestions throughout the present investigation. Thanks are also due to Dr. Natsuo YUKAWA (now Professor of Toyohashi University of Technology), Dr. Minoru DOI (now Nagoya Institute of Technology), Mr. Akira NOHARA, Mr. Nobuo OKAMOTO and Mr. Tamotsu TONO for their kind assistances and encouragements in carrying out the experiments. He is deeply indebted to Dr. Atsushi YAMAMOTO and other members of Metal Physics Laboratory of Nagoya University for their assistances.

The author wishes to express his gratitude to Dr. Takashi

SAKA, Mr. Kenji YASUDA, Mr. Hidenobu YAMAMOTO (now Rigaku Denki) and other members of Ultra High Intensity X-Ray Laboratory of Nagoya University for their co-operations in carrying out the X-ray topographic observations. He is also grateful to Mr. Michiyoshi MAKI, Dr. Yukio TAKANO, Dr. Masao TAMURA and Mr. Seiichi ISOMAE of Central Research Laboratory, Hitachi Ltd. for some specimen preparations and fruitful discussions. It is a pleasure to acknowledge the kindness of Mr. Chiaki MORITA, Mr. Shigeo ARAI and other members of Electron Optics Laboratory of Nagoya University in carrying out the electron microscope observations.

# LIST OF PUBLICATIONS

1. S. Asano, Y. Nishino and R. Otsuka
   : J. Jpn. Inst. Metals 43 (1979) 241 [in Japanese].
   "Lattice Hardening and Anomalous Softening of Iron and Steel Caused by Electrolytic Hydrogen Charging"

2. W.A. Jesser, T. Imura, A. Nohara and Y. Nishino
   : Kristall und Technik 14 (1979) 1219.
   "Effects of Environmental Gas on HVEM Radiation Damage in Aluminum"

3.* Y. Nishino, M. Suzuki, T. Tono, H. Saka and T. Imura
   : Jpn. J. Appl. Phys. 20 (1981) 1533.
   "Straining Apparatus for Dynamic Observation by X-Ray Topography"

4.* Y. Nishino, H. Saka and T. Imura
   : Phys. Status Solidi (a) 70 (1982) 729.
   "Dislocation Configuration Characteristic of Deformed Czochralski-Grown Silicon Crystals"

---

* Papers related to the present investigations.

5.* Y. Nishino and T. Imura
: Jpn. J. Appl. Phys. 21 (1982) 1283.
"Dislocation Generation in the Initiation of Fractures in Silicon Crystals"

6.* Y. Nishino and T. Imura
: Phys. Status Solidi (a) 73 (1982) 173.
"Generation Process of Dislocations in Precipitate-Containing Silicon Crystals"

7.* Y. Nishino and T. Imura
: Phys. Status Solidi (a) 74 (1982) 793.
"Viscoelastic Behaviour of Oxide Films on Silicon Crystals"

8.* T. Imura and Y. Nishino
: J. Crystallogr. Soc. Jpn. 24 (1982) [in Japanese] in press.
"Development of Deformation Apparatus for In-Situ Observations by X-Ray Topography"

9.* T. Imura and Y. Nishino
: X-Ray Instrumentation for the Photon Factory (D. REIDEL, Tokyo, 1983) in press.
"High-Temperature Deformation Apparatus for Real-Time X-Ray Topographic Observations"

10. Y. Nishino, U. Messerschmidt and T. Imura
: submitted to Mater. Sci. Eng.
"Hardening of MgO Single Crystals by X-Ray Irradiation at Room Temperature"

11. U. Messerschmidt, Y. Nishino, T. Imura and H. Saka
: submitted to Phys. Status Solidi.
"X-Ray Topographic In-Situ Observation of Slip Band Propagation in MgO Single Crystals"

12.* Y. Nishino, H. Saka and T. Imura
: in preparation.
"Temperature Dependence of Friction Force Acting on Dislocations in Silicon Crystals"

13.* Y. Nishino and T. Imura
: in preparation.
"Dislocation Configurations Induced by Cyclic Deformation in Silicon Crystals"